Theoretical studies of atom-atom, atom-photon and photon-photon entanglement

A Thesis
Presented to
The Academic Faculty

by

Bo Sun

In Partial Fulfillment
of the Requirements for the Degree
Doctor of Philosophy

School of Physics
Georgia Institute of Technology
December 2006

Theoretical studies of atom-atom, atom-photon and photon-photon entanglement

Approved by:

Professor Li You
School of Physics, Chair

Professor Alex Kuzmich
School of Physics

Professor Ronald F. Fox
School of Physics

Professor David S. Citrin
School of Electrical and Computer Engineering

Professor Michael S. Chapman
School of Physics

Date Approved: December 26, 2006

To my parents,

Mr. He-Quan Sun and Mrs. Yi-Yun Su

ACKNOWLEDGEMENTS

I want to share this great moment in my life with all my friends at Georgia Tech, in the USA, and in China. Without their help and support, this work would not have been possible.

First of all, I want to express my sincere gratitude to my thesis advisor, Professor Li You, for his support and encouragement and for the inspiration that his thinking has provided for my work. I began working with Li four years ago and since then I have learned a lot from him. His experience and insight into atomic, molecular and optical physics are the most precious for improving my researching abilities.

In the past two years, I have had the great pleasure of working with Dr. Duan-Lu Zhou, who was Li's post-doc at that time. We have collaborated on two papers which are of great importance to my thesis work. His rich physics knowledge and smart thinking always make our discussions enjoyable.

I am grateful to Alexander Wiener (Alex), for his proofreading and nice feedbacks. I also want to express many thanks to my friends Drs. Wen-Xian Zhang, Peng Zhang and Su Yi, for their discussions on some issues of my thesis work. Wen-Xian has taught me many numerical skills in C, Mathematica and Matlab. Peng has given me detailed explanations on the representation theory of group. Many thanks to Hsiang-Hua Jen and Hai-An Wang for various help they gave me. It has always been a great pleasure for me to discuss interesting physics questions with them.

On a personal note, I am indebted to my parents and my sister for their support and encouragement over all these years. I am thankful to my wife Li-Xia Wei, who was always by my side throughout my graduate studies. She is the best and the most wonderful friend and has been always incredibly supportive to me in our life together.

TABLE OF CONTENTS

LIST OF TABLES

LIST OF FIGURES

SUMMARY

In this thesis the entanglement properties of atom-atom, atom-photon, and photon-photon are investigated. The recent developments of quantum computation as well as quantum information and communication have attracted much interest in the generation of these entanglements in the laboratory. Entanglement is now believed to be an essential resource for realizing some non-classical tasks, such as teleportation.

We first study a model system in the cavity QED setup. Cavity QED has proved to be excellent in the coherent manipulation of atoms and cavity photons. By using a four-level atom and two resonant cavity modes, we can generate atom-photon entanglement almost deterministically. The generated photon can be distributed which is ideal for quantum communication.

An extension of the above model to a six-level atom and again two resonant cavity modes can generate entangled photon pairs by appropriately adjusting system parameters. The overall process can be divided into two steps. In each step, a cavity photon will be generated and leak out of the cavity. The final state of the atom becomes disentangled with both photons. Thus, the whole process generates an almost maximally entangled photon pair with very high probability.

We then investigate the atom-atom entanglement in a 1D harmonic trap. At low temperature, the atom-atom interaction is dominated by the s-wave/p-wave scattering, further simplified as a contact interaction. We show the dependence of the pair entanglement on the scattering length and temperature, as well as the particle symmetry requirement (bosons or fermions). Among many peculiar properties in 1D systems, we briefly discuss the "Fermi-Bose duality" in this simple 1D system.

While the entanglement properties of a single-channel model has recently been obtained for 1D and 3D systems, we study the entanglement of a multi-channel process in a cylindrical harmonic trap. We adopt a model system consisting of two fermionic atoms with opposite

spins. The open-channel atomic pair can be converted to a closed-channel bosonic molecule, or vice versa, leading to orbital deformation and entanglement. We carry out calculations in the so-called "broad resonance" regime and discuss the dependence of entanglement on the trap geometry.

Finally we present detailed studies of the spin mixing between two ^{87}Rb atoms in a single lattice site. Staring from the spin-1 manifold, we discuss various motional state approximations which turn out to cause observable errors. Then, we include the dipolar interaction for a complete study. We find that while the dipolar effect can be negligible in a spherical harmonic trap, the dipolar interaction can lead to an experimentally observable frequency shift in a cylindrical harmonic trap with very large aspect ratio. We also consider the spin-2 manifold and discuss the corresponding spin mixing.

CHAPTER I

INTRODUCTION

Quantum mechanics has been a very successful theory in dealing with microscopic phenomena. It is more fundamental and accurate than classical mechanics and has shown many amazing properties that cannot be described by classical mechanics. One of its counter-intuitive properties is quantum entanglement. Quantum entanglement is a basic concept in quantum mechanics. It describes the quantum correlations of two or more objects whose quantum states have to be described with reference to each other, even though the individual objects may be spatially separated. It is responsible for the test of the validity and interpretation of standard quantum mechanics [1, 2]. Quantum entanglement has been a topic of extensive study in recent years, motivated in large part by the development in quantum information and computing science. It has been viewed as an essential resource for performing non-classical tasks [3, 4], such as quantum cryptography [5, 6, 7], teleportation [8, 9, 10, 11, 12], as well as the exponential speed-up promised by Shor's factoring algorithm [13].

For any physical system, a natural question arises: Is quantum entanglement a physical property? If so, what does it describe? Quantum entanglement is not a traditional physical quantity, as there does not seem to exist a corresponding Hermitian operator. It describes the quantum correlations among different degrees of freedom, in contrast to the more standard correlation functions. It is now understood that only quantum correlations, not classical correlations, contribute to quantum entanglement [14]. Different from applications of entanglement in quantum information science, non-locality of a composite system is generally not believed to be a necessary element for the description of quantum correlations in the system.

In order to quantify quantum entanglement, many definitions have been proposed for

1

both pure states and mixed states. Until recently, very little has been known about genuine multi-body entanglement. On the contrary, two-body entanglement has been studied extensively with fruitful results obtained. This paves the way for our study on two-body entanglement. A qualified two-body entanglement measure must satisfy the following three basic requirements [15, 16]:

(1) It gives zero for separable states. Separable states are those states that can be written in the following form [17]

$$\rho^{(12)} = \sum_i p_i \rho_i^{(1)} \otimes \rho_i^{(2)}. \tag{1.1}$$

Here $p_i \geq 0$ and $\sum_i p_i = 1$. $\rho_i^{(1)}$ and $\rho_i^{(2)}$ are the density matrices of the respective subsystem. States that cannot be written in this form are called inseparable, or entangled.

(2) It should be invariant under local unitary transformations, which is an intuitive requirement that entanglement should be basis independent.

(3) It should not increase under local operation and classical communication (LOCC). Such a requirement guarantees that all classical operations will not contribute to quantum entanglement, *i.e.*, quantum entanglement cannot be prepared by purely classical operations.

We point out that there are also some other restrictions, *e.g.*, additivity and convexity [16]. Here we do not impose those restrictions, as the above three criteria have already defined an entanglement monotone.

For any two-body pure states, von Neumann entropy is a widely used entanglement measure [18, 19]. It originates from analogy with thermodynamics and relies on the Schmidt decomposition. Any state $|\Psi_{12}\rangle = \sum_{n\nu} C_{n\nu}|n\rangle_1|\nu\rangle_2$ can be written in the following Schmidt form

$$|\Psi_{12}\rangle = \sum_s \sqrt{\lambda_s}|F_s\rangle_1|G_s\rangle_2, \tag{1.2}$$

where λ_s are the eigenvalues of the reduced density matrix $CC^\dagger$ (or $C^\dagger C$), with C being the coefficient matrix of the wave function. The reduced density matrix can be obtained by tracing out either subsystem. Then von Neumann entropy is defined as

$$\mathbb{E} = -\sum_s \lambda_s \ln(\lambda_s), \tag{1.3}$$

2

with $\lambda_s \geq 0$ and $\sum_s \lambda_s = 1$.

For mixed states, von Neumann entropy is generally not a valid entanglement measure. In fact, determining whether or not a mixed state is entangled is considered difficult. Formally, it has been shown to be NP-hard (Non-deterministic Polynomial-time hard) [20]. Entanglement measures based on operational considerations, such as entanglement of formation [21], entanglement cost, relative entropy of entanglement and distillable entanglement [16] have been proposed. The calculations of these quantities rely on maximization or minimization of certain functions, and in general require demanding computational capabilities. Thus, we refer to negativity, a quantity without a corresponding physical operation but much easier to calculate, as our mixed state entanglement measure.

Negativity was first suggested by R. F. Werner [22], and was based on the Peres-Horodecki criterion [23, 24] of the positivity for the partially transposed density matrix. The eigenvalues of a density matrix are always non-negative. However, this is not the case for the partially transposed density matrix, as partial transposition is not a completely positive map. Negativity is defined as the absolute sum of all of the negative eigenvalues, or equivalently

$$\mathbb{N} = \frac{\sum_i |\lambda_i| - 1}{2}, \tag{1.4}$$

where λ_i are the eigenvalues of the partially transposed density matrix satisfying $\sum_i \lambda_i = 1$. Here the partial transposition can be done with respect to either subsystem. If negativity gives a non-zero value, the corresponding state must be entangled.

Many studies have been devoted to entanglement measures, yet a realistic question of both theoretical and experimental importance is how to generate a desired entangled state. Many theoretical models have been proposed and some of them have been implemented experimentally in atomic-molecular-optical (AMO) systems. All of the entangling schemes rely on direct or indirect interactions between subsystems. Such interactions are almost ubiquitous in real atomic systems. Atoms not only interact with the near resonant electromagnetic field, but also with other surrounding atoms. These types of interactions will be

3

utilized to generate the desired entanglement. For our purpose, we want to realize atom-photon, photon-photon, and atom-atom entanglement, which are believed to be the building blocks of quantum information and communication physics.

Perhaps the simplest realization of an atom-photon entangled state is by cavity QED. In a typical cavity QED system, an atom with internal structure is localized inside a cavity and coherently interacts with the quantized cavity mode. We denote $|e\rangle$ and $|g\rangle$ as two energy levels of the atom and $|n\rangle$ as the number state of the cavity field mode that is nearly resonant to the atomic transition frequency. Starting from $|\Psi_{ap}\rangle(t = 0) = |e\rangle|0\rangle$, there will be coherent Rabi oscillations between $|e\rangle|0\rangle$ and $|g\rangle|1\rangle$. At certain times, the combined system will evolve to $|\Psi_{ap}\rangle = (|e\rangle|0\rangle \pm i|g\rangle|1\rangle)/\sqrt{2}$ (up to a global phase factor), an atom-photon entangled state. However, it does not have a well-defined photon number, thus limiting its potential usage in a quantum network, where we want photons to carry information to remote nodes with unit probability (in an ideal case). A feasible model is to use two orthogonal polarizations as the natural basis of the photonic qubit. The desired state should take the similar form $|\Psi'_{ap}\rangle = (|e\rangle|L\rangle + |g\rangle|R\rangle)/\sqrt{2}$, where $L(R)$ denotes the photon polarization. This remedies the above problem and may be realized with state-of-the-art cavity QED technology.

Another demanding task is to realize a photon-photon entangled state. Until very recently, most experimental realizations of photonic entangled states came exclusively from parametric down conversion (PDC) using nonlinear crystals where a single pump photon spontaneously converts itself into two correlated photons satisfying energy and momentum conservation [25, 26, 27, 28, 29, 30, 31]. The shortcoming is that this is a stochastic process, and the probability of conversion is very low due to the small nonlinearity in normal crystals. Cavity QED system provides an alternative method for generating photon-photon entangled states. The atom in the cavity can be viewed as a strong nonlinear medium, thus inducing an effective interaction between two cavity photons. Our proposed scheme has the advantage that the photon-photon entangled state can be controlled and generated on demand. Again, such entangled state can be generated in a cavity QED by appropriately adjusting system parameters.

In contrast to photons, where the mutual interaction is very weak, atoms can interact with surrounding atoms with relatively strong strength. However, the creation of long-lived entangled pairs with material particles (atoms and ions) is a relatively recent pursuit [32, 33, 34, 35], spurred on in large part by developments in quantum logic and computing. These experimental efforts have been very successful [36, 37, 38] and are highlighted by the demonstration of a 6-ion GHZ state [39], using a proposal with trapped ions due to Mølmer *et al.* [40]. On the theoretical side, the study of the entanglement between two trapped atoms (ions) will be helpful to elucidate the entanglement dependence on system parameters, *e.g.*, trap frequency, interaction strength, and temperature, thus controlling the generation of the desired entangled states. For two neutral atoms at very low temperature, the system dynamics are usually described by a single parameter, the s-wave scattering length a_s. The corresponding spectrum has been obtained analytically [41, 42], and the entanglement properties can then be straightforwardly calculated. In addition, we study the dependence of entanglement on particle symmetry, *i.e.*, how the symmetry requirements affect the pair entanglement.

In recent years, optical lattice has been a powerful tool for studying quantum degenerate gases. An optical lattice consists of arrays of microscopic potentials induced by the ac Stark effect of interfering laser beams [43, 44, 45, 46, 47, 48, 49, 50, 51]. Optical lattice provides a more flexible system for studying cold atom gases. Many new phenomena arise in optical lattices, such as Superfluid-Mott Insulator (SF-MI) phase transition [52, 53, 54, 55] and BCS (Bardeen-Cooper-Schrieffer)-BEC (Bose-Einstein Condensation) crossover using Feshbach resonance [56, 57]. In the MI phase where the tunnelling is negligible, each lattice site can be viewed as an independent trap. With only a few atoms confined in the same lattice site, the dynamics in each lattice well may be solved exactly. The experiments at ETH [56, 57] have investigated lattice fermions in the MI phase, where two fermionic atoms with different internal states are in the same lattice site. As the system is swept adiabatically across Feshbach resonance, two open-channel fermions can be converted to a closed-channel molecular boson, or vice versa. At the same time, a band insulator evolves continuously into states occupying many bands, thus acquiring orbital deformation and entanglement

[58]. It is then interesting to study how the pair entanglement changes during this process. In the single-channel model, the entanglement of two bosonic atoms in a spherical harmonic trap has been investigated in Ref. [59]. To extend the earlier results to a multi-channel problem with cylindrical symmetry, we adopt the model proposed by R. B. Diener and Tin-Lun Ho [58]. Different from the single-channel problem as studied in Refs. [41, 42], the system dynamics are now determined by two parameters, the s-wave scattering length a_s and the effective range r_0. The experiments are carried out in the so-called "broad resonance regime", $i.e.$, $|r_0|$ much less than the trap widths, where the molecular component turns out to be always negligible, thus allowing for a clear calculation of pair entanglement without the knowledge of the molecular wave function. Not surprisingly, this model reduces to the original single-channel problem for vanishing r_0.

Another interesting phenomenon is coherent spin mixing, first realized in the limit of a condensate with large number of atoms in a single trap [60, 61]. Recent experiments have been focusing on the opposite limit of many identical trapping sites, each containing two atoms as in an optical lattice [62, 63, 64]. Binary collisions conserve the magnetic quantum number of the total spin, thus limiting the accessible channels in the spin mixing. For example, preparing two $f = 1$ ^{87}Rb atoms in the spin state $|m_f = 0, m'_f = 0\rangle$, the spin mixing will happen between $|m_f = 0, m'_f = 0\rangle$ and $|m_f = 1, m'_f = -1\rangle$. In this case, the scattering potential can be split into two parts with scattering strengths c_0 being spin independent and c_2 spin dependent, where the Rabi oscillation for the spin mixing is crucially determined by the latter. From the oscillation frequency, we can extract the scattering length difference, from which the magnetic ground state can then be identified. In the original papers [62, 63, 64], the theoretical estimates use the ground state of the trap as the motional state, inevitably causing some errors. Detailed studies on the motional state will thus give better results for such precision measurement and unambiguously determine the magnetic ground state.

To fully explore the above problem, we also need to calibrate the spin dipolar effect. The origin of the spin dipolar interaction comes from the intrinsic magnetic dipole moment of the atom, which is related to its total angular momentum. The dipolar effect in condensates has

attracted much interest in recent years, and many methods have been proposed to observe such effect [65, 66, 67, 68, 69, 70, 71, 72, 73, 74, 75, 76]. To date, the dipolar interaction has been observed experimentally only for ^{52}Cr ($f = 3$) which has a dipole moment of $6\mu_B$ [77]. For the few-body counterpart, we find that the dipolar interaction may manifest itself in the spin mixing process. The spin dipolar effect is estimated by the relative strength between the dipolar coefficient c_d and the spin dependent coefficient c_2. A larger value of $|c_d/c_2|$ indicates an enhanced spin dipolar effect. For a typical system, the dipolar effect is negligibly small in a spherical harmonic trap. However, it may become detectable in cylindrical harmonic traps with very large or small aspect ratios. Detailed calculations should decide what kind of shape, pancake shape or cigar shape, can best reveal the dipolar effect, so that it can provide an alternative method for observing such interesting effect in a few-body system. This will further deepen our understanding of the dipolar effect in spin mixing dynamics.

This thesis is organized as follows. Chapter 1 is an introduction, where we give a brief review of entanglement and other relevant topics. In the second chapter, we will study atom-photon entanglement generation and distribution in a cavity QED system. We also review some aspects of the cavity system and discuss in detail the parameter range for generating optimized results.

In chapter 3, we will discuss the generation of photon-photon entangled states, again based on a cavity QED system. We propose an efficient method for generating maximally entangled photon pairs, which are urgently needed by experimentalists. Combined with atom-photon entanglement generation, these proposals may be useful for a distributed quantum network in which matter qubits serve as storing units while photonic qubits serve as information carriers.

In chapter 4, we will investigate the entanglement of two identical atoms in a one-dimensional harmonic trap. We adopt the well-known pseudopotential to model the atom-atom interaction. According to different symmetry requirements, we discuss the entanglement between two bosonic (fermionic) atoms under s-wave (p-wave) scattering, respectively. We give detailed results based on our models and discuss the dependence of entanglement

on the scattering length and temperature.

In chapter 5, we will calculate the entanglement of two fermionic atoms with different internal states during the BCS-BEC crossover in a cylindrical harmonic trap. We discuss the entanglement in a nearly spherical harmonic trap, as well as in traps with very large or small aspect ratios. We find that the entanglement tendency during the BCS-BEC crossover remains essentially the same as in a spherical harmonic trap. In this multi-channel problem, it turns out that the results coincide with that of single-channel problem in the broad Feshbach resonance regime.

In chapter 6, we study the spin mixing of two ^{87}Rb atoms in a single optical lattice site. We approximate each lattice site as a harmonic trap in the limit of negligibly small tunnelling. We give detailed studies on the spin mixing frequency for various approximations of the two-atom motional state. We give numerical results to interpret the difference between the experimentally measured and the theoretically calculated values. We also include the dipolar effect and discuss its dependence on the trap geometry.

CHAPTER II

ATOM-PHOTON ENTANGLEMENT GENERATION IN A CAVITY QED SYSTEM

2.1 Introduction

In this chapter, we are going to discuss how to generate atom-photon entangled states in a cavity QED system. For a large class of quantum communication protocols (including cryptography protocols, teleportation, entanglement purification, *etc.*), one always begins with the following statement: "*Imagine that Alice has an entangled pair of particles, and she sends one particle to Bob...*". So creating entanglement is believed to be a pressing need for quantum information and communication. As our first step towards this direction, we want to realize atom-photon entanglement, wherein the atom provides reliable quantum information storage with local entanglement capabilities and the photon provides quantum communication capabilities over a long distance. In particular, it will be important to be able to reliably convert and transfer quantum information between material and photonic qubits.

Cavity QED proves to be an ideal system for generating atom-photon entanglement. For a simple illustration of an optical cavity QED, we consider a motionless two-level atom, labelled by $|e\rangle$ and $|g\rangle$, with energy difference $\omega_0 \equiv \omega_e - \omega_g > 0$. The atom with the electric dipole matrix element $\vec{d}$ will interact with a cavity field mode (with angular frequency ω_c) which is nearly resonant with the atomic transition, *i.e.*, $|\omega_0 - \omega_c| \ll \omega_0, \omega_c$. The electric field in this mode can be expressed in a second quantized form $E(\vec{r}) = \mathcal{E}_0(a\vec{f}^*(\vec{r}) + a^\dagger \vec{f}(\vec{r}))$, where a ($a^\dagger$) is the operator of annihilating (creating) a cavity mode photon. $\vec{f}(\vec{r})$ is a dimensionless complex vector function, characteristic of the mode, that satisfies the boundary conditions on the cavity walls. The modulus of $\vec{f}(\vec{r})$ is normalized to unity at the field maximum. The quantity $\mathcal{E}_0$, called the field per photon is $\mathcal{E}_0 = \sqrt{\hbar\omega_c/(2\epsilon_0 V)}$. The effective mode volume is,

by definition, $V = \int d\vec{r} |\vec{f}(\vec{r})|^2$. The combined system made of a single atom and a resonant mode of a high Q cavity reveals dynamical behavior very different from that of the free atom or field subsystem, with striking manifestations of the coherent and nonlinear effects of the vacuum field on the atomic system [78].

After the rotating wave approximation, which excludes the counter rotating terms from the equations of motion, the Hamiltonian describing atom-photon interaction is

$$H_{ap} = \hbar(g_0 a^\dagger |g\rangle\langle e| + g_0^* a|e\rangle\langle g|), \tag{2.1}$$

where g_0 is called *vacuum Rabi frequency*, defined as $g_0 = \mathcal{E}_0 \vec{d} \cdot \vec{f}(\vec{r})/\hbar$. This is the famous Jaynes-Cummings model [79], describing the coherent evolution between the atom and the cavity field. The atom in the ground state $|g\rangle$ absorbs a cavity photon and jumps to the excited state $|e\rangle$ or vice versa. Exact diagonalization of the Hamiltonian H_{ap} leads to the so-called dressed states, which are in general a superposition of the unperturbed states $|e, n\rangle$ and $|g, n + 1\rangle$ [80], where n denotes the number of photons in the cavity mode.

We can also use an external laser to control the atom or the cavity field. The external laser can be viewed as a photon reservoir. We treat it classically since losing or gaining several photons is unimportant to the laser. There are two types of interaction for the external laser: "side excitation" and "end excitation". In the former case, the laser couples directly to the atom. The interaction Hamiltonian is

$$H_{af} = \hbar(\Omega_{af}|e\rangle\langle g| + \Omega_{af}^*|g\rangle\langle e|), \tag{2.2}$$

with Ω_{af} the coupling strength between the laser field and the atom [81]. In the latter case, the laser couples to the cavity field through the side mirror(s). The interaction Hamiltonian is

$$H_{pf} = \hbar(\Omega_{pf}a^\dagger + \Omega_{pf}^*a), \tag{2.3}$$

with Ω_{pf} the coupling strength between the laser field and the cavity field [81].

In real cavity systems, we need to take dissipations into consideration. Generally speaking, two types of dissipations are important: cavity decay rate κ and atomic spontaneous rate γ. κ represents the rate of a cavity photon leaking out of the cavity, and γ represents

the rate at which the atom loses its coherence. For typical optical cavities, g, κ and γ are all on the order of MHz, and it is the relative strength that determines the system dynamics. Cavity QED is analogous to a quantum harmonic oscillator in certain aspects, with g being responsible for oscillations and κ, γ being responsible for dissipations. Thus, if $g \gg (\kappa, \gamma)$, the so-called strong coupling regime, the system behaves like a damped oscillator, so many Rabi oscillations are expected. If $g \ll (\kappa, \gamma)$, the so-called weak coupling regime, it behaves like a over-damped oscillator, so no oscillation will happen. In the literature, these dissipations are usually included in the system dynamics via two types of approaches. One is the density matrix approach in the form of a master equation, and the other is the non-Hermitian Hamiltonian approach. Both approaches are quite accurate in describing the system dynamics with only very tiny differences, as we will demonstrate later.

Based on the above considerations, we propose a system composed of a single trapped atom inside a high Q optical cavity for the deterministic generation of atom-photon entanglement and its distribution via a well directed photon from a high Q optical cavity. Our model is a direct extension of the earlier proposal by C. K. Law *et al.* [82, 83] for a deterministic single photon (or "Fock states") source [84, 85, 86], which is an indispensable device for some quantum cryptographic applications [6, 7]. In the original model of Law and coworker, a single atom is placed inside a high Q optical cavity. A pictorial illustration of the required energy level structure is presented in the left panel of Fig. 2.1, where a three-level $\Lambda-$type atom with one excited state ($|e\rangle$) and two long lived ground states ($|g_1\rangle$ and $|g_2\rangle$) couple respectively to a classical pump field (in solid line) and the cavity field (in dashed line). Working in the strong coupling limit, the dominant absorption-emission process will then consist of an atom starting in $|g_1\rangle$, pumped into the excited state $|e\rangle$, which then decays via the cavity into $|g_2\rangle$ [82, 83, 87, 88]. Following emission, an additional external laser field driving the transition $|g_2\rangle \rightarrow |e\rangle$ will reset the atom to state $|g_1\rangle$, preparing it for the next photon emission. Such a single photon "gun" can expect to reach a repetition rate on the order of κ, which is typically several MHz. An alternative approach based on adiabatic passage for a deterministic or "push button" single photon source was considered in Refs. [87, 88].
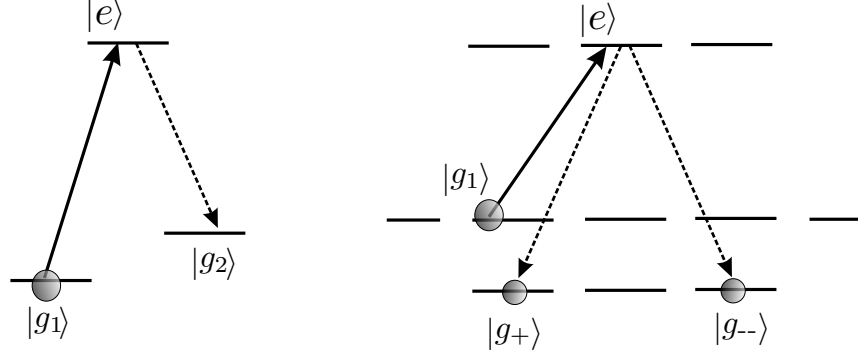
Figure 2.1: Atom-photon entanglement illustrations.

2.2 A model system

The model system proposed for this study consists of a direct extension of the famous Law-Kimble model to a four-level atom as illustrated in the right panel of Fig. 2.1, with $|e\rangle$ now resonantly coupled to both states $|g_+\rangle$ and $|g_-\rangle$ through the right and left circular polarized cavity photon field. Following Law *et al.* [82], the coherent part of our model Hamiltonian can be expressed as

$$H_0 = \hbar g(a_L \sigma_{e,g_-} + a_L^\dagger \sigma_{g_-,e} + a_R \sigma_{e,g_+} + a_R^\dagger \sigma_{g_+,e}) + \hbar r(t)(\sigma_{g_1,e} + \sigma_{e,g_1}), \qquad (2.4)$$

where $\sigma_{\mu,\nu}(t=0) = |\mu\rangle\langle\nu|$ ($\mu,\nu = g_1, e, g_-, g_+$) are atomic projection operators. a_ξ and $a_\xi^\dagger$ ($\xi = L, R$) are annihilation and creation operators for the quantized cavity fields. $r(t)$ denotes the coupling between the atom and the external classical field. The master equation of the system is

$$\begin{aligned}
\frac{d}{dt}\rho &= -\frac{i}{\hbar}[H_0, \rho] + \kappa \sum_{\xi=L,R} (2a_\xi \rho a_\xi^\dagger - a_\xi^\dagger a_\xi \rho - \rho a_\xi^\dagger a_\xi) \\
&\quad + \sum_{\mu=g_1,g_-,g_+} \frac{\gamma\beta_\mu}{2}(2\sigma_{\mu,e}\rho\sigma_{e,\mu} - \sigma_{e,e}\rho - \rho\sigma_{e,e}),
\end{aligned} \qquad (2.5)$$

where β_μ denotes the branch ratio of the atomic decay to levels $|\mu\rangle$ and $\beta_{g_1} + \beta_{g_-} + \beta_{g_+} = 1$. Similar to Law's protocol, the system is prepared in the state $|g_1\rangle$ with no photon in the cavity. After turning on the classical field $r(t)$ for a period T_0, one photon (either left polarization or right polarization) will be generated in the cavity, which immediately transmits

outside the cavity in the bad cavity limit

$$\kappa \gg g^2/\kappa \gg \gamma. \tag{2.6}$$

The probability of detecting a left polarized or right polarized photon is given by

$$P_\xi(t) = 2\kappa \int_0^t \langle a_\xi^\dagger(t') a_\xi(t') \rangle dt'. \tag{2.7}$$

To gain more physical insight, we describe the dynamic evolution of the system using the non-Hermitian effective Hamiltonian [89]

$$H_{\text{eff}} = H_0 - i\hbar\kappa a_L^\dagger a_L - i\hbar\kappa a_R^\dagger a_R - i\hbar\frac{\gamma}{2}\sigma_{e,e}. \tag{2.8}$$

Using a cavity photon number limited basis of $|\mu, n_L, n_R\rangle$ ($\mu = g_1, e, g_-, g_+$) and $n_{L/R} = a_\xi^\dagger a_\xi (= 0, 1)$, the pure state wave function can be written as

$$|\psi(t)\rangle = a_{g_1}|g_1, 0, 0\rangle + a_e|e, 0, 0\rangle + a_{g_-}|g_-, 1, 0\rangle + a_{g_+}|g_+, 0, 1\rangle. \tag{2.9}$$

Its conditional dynamics are then described by $i\hbar|\dot\psi\rangle = H_{\text{eff}}|\psi\rangle$, which yields

$$\begin{aligned}
i\dot a_{g_1}(t) &= r(t)a_e, \\
i\dot a_e(t) &= r(t)a_{g_1} + ga_{g_-} + ga_{g_+} - i\frac{\gamma}{2}a_e, \\
i\dot a_{g_-}(t) &= ga_e - i\kappa a_{g_-}, \\
i\dot a_{g_+}(t) &= ga_e - i\kappa a_{g_+}.
\end{aligned} \tag{2.10}$$

For classical field $r(t) \ll g^2/\kappa$, the approximated solution becomes

$$\begin{aligned}
a_{g_1}(t) &\approx \exp\left[-\frac{2}{4g^2/\kappa + \gamma}\int_0^t r^2(t')dt'\right], \\
a_e(t) &\approx -i\frac{2r(t)}{4g^2/\kappa + \gamma}a_{g_1}(t), \\
a_{g_\mp}(t) &\approx -i\frac{g}{\kappa}a_e(t).
\end{aligned} \tag{2.11}$$

Assuming the given initial condition $a_{g_1}(0) = 1$ and $a_{e/g_-/g_+}(0) = 0$, the left and right polarized modes are equally populated if their couplings to the cavity mode are identical. The conditional state of the system then becomes [90, 91, 92]

$$\frac{1}{\sqrt{2}}\left(|g_-\rangle|n_L = 1, 0\rangle + |g_+\rangle|0, n_R = 1\rangle\right), \tag{2.12}$$

an atom-photon entangled state.

2.3   Numerical results

We have performed numerical calculations for a classical driving field

$$r(t) = r_0 \sin^2\left(\frac{\pi t}{T_0}\right), \qquad 0 \le t \le T_0, \tag{2.13}$$

with $(g, \kappa, \gamma, r_0) = (2\pi)(45, 45, 4.5, 22.5)$ MHz and $T_0 = 6/\gamma$=210 ns. Selected results are presented in Figs. 2.2 and 2.3. The conditional probability for a left or right polarized photon rapidly increases to 49%. For comparison, we have solved both the conditional wave function dynamics as well as the complete master equation dynamics. The non-Hermitian Hamiltonian approach gives a slightly lower value for final photon emission probability because it excludes repeated spontaneous decay. In the event that $|e\rangle$ decays to $|g_1\rangle$, it may be re-excited by the classical field before emitting the photon.
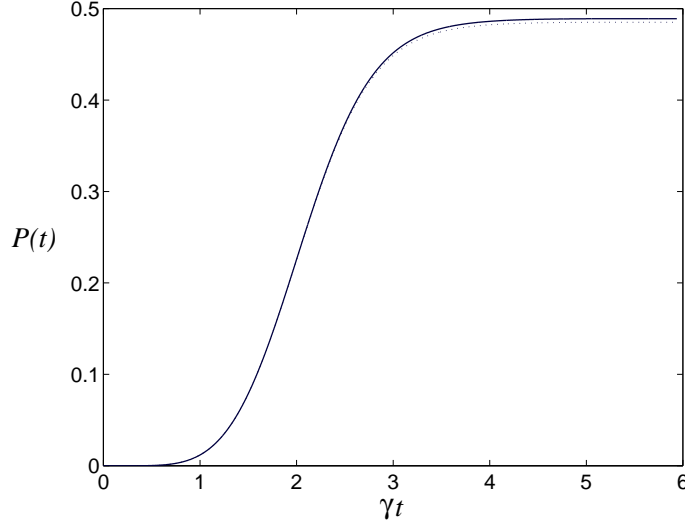
Figure 2.2: The conditional probability for the emission of a cavity photon. The solid line is master equation approach, and the dotted line is non-Hermitian Hamiltonian approach.

We note that the bad cavity limit, or the operating condition as specified by the Eq. (2.6), in fact corresponds to the cavity QED system not in the strong coupling limit. Thus, the cavity photon decays immediately once created, and this allows for an adiabatic description by eliminating the atomic dynamics in the cavity. The condition of $g^2 \gg \kappa\gamma$ is in fact the same requirement of a large cooperativity parameter $(C \propto g^2/(\kappa\gamma))$ or a small critical atom number $(n_c \propto \kappa\gamma/g^2)$ as in the strong coupling limit [78]. It turns out that this
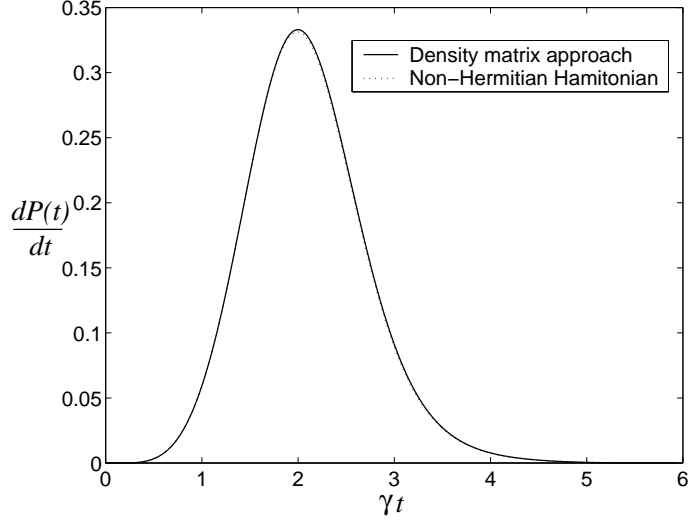
Figure 2.3: Cavity emission rate.

parameter is an important characterization for the fidelity of several important quantum computing protocols of atomic qubits inside high Q cavities [93]. We now further illuminate this in terms of the basic element of quantum information exchange between an atomic qubit and a cavity.

We consider a three-level Λ-type coupling scheme as in the left panel of Fig. 2.1. When the classical field $\Omega(t)$ is Raman resonant with respect to the cavity photon (assuming a perfect compensation for ac Stark shifts [94]), while strongly off-resonant with respect to the atomic transition $|e\rangle \leftrightarrow |g_2\rangle$, the two states $|g_1, 0\rangle$ and $|g_2, 1\rangle$ are effectively coupled directly through a Rabi frequency Ω_{eff} and an effective atomic decay rate γ_{eff} given by

$$
\begin{aligned}
\Omega_{\text{eff}} &= \frac{1}{2}\frac{\Omega g}{\Delta}, \\
\gamma_{\text{eff}} &= \frac{1}{4}\frac{\Omega^2}{\Delta^2}\gamma,
\end{aligned}
\tag{2.14}
$$

where $\Delta = \omega_L - (\omega_e - \omega_1)$ is the pump field detuning.

To expect coherent dynamics for state mapping [95] according to

$$
(\alpha|g_1\rangle + \beta|g_2\rangle) \otimes |0\rangle \rightarrow |g\rangle \otimes (\alpha|0\rangle + \beta|1\rangle),
\tag{2.15}
$$

one requires $\Omega_{\text{eff}} \gg \gamma_{\text{eff}}$ and $\Omega_{\text{eff}} \gg \kappa$, which reduces to

$$
\frac{\kappa}{g} \ll \frac{\Omega}{\Delta} \ll \frac{g}{\gamma}.
\tag{2.16}
$$

15
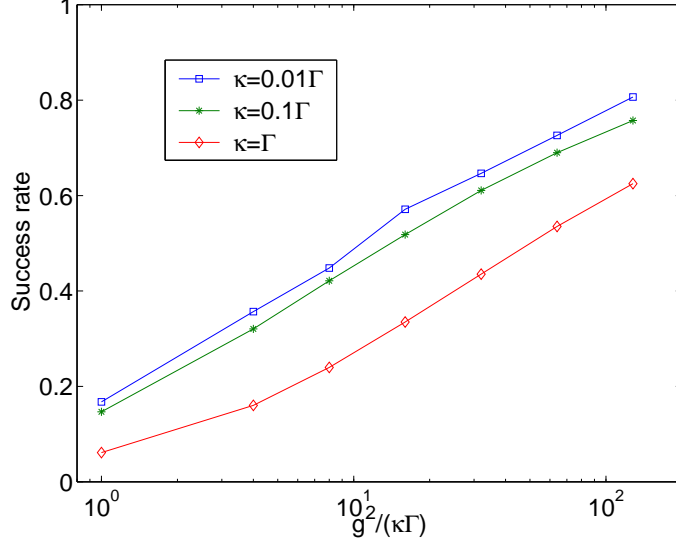
Figure 2.4: The success rate of mapping the atomic state $\alpha|g_1\rangle + \beta|g_2\rangle$ into the cavity state $\alpha|1\rangle_C + \beta|0\rangle_C$. The worst case scenario of $\alpha = 1$ and $\beta = 0$ is considered here. States with non-zero βs generally lead to proportionally larger success rates. We have used $\gamma = (2\pi)20$ (MHz) and $\Delta = 50\gamma$.

Thus $g^2 \gg \kappa\gamma$. This requirement can also be understood with the order of magnitude estimates suggested by C. Monroe (see also [96]). The fidelity of state mapping is approximately given by $F = 1 - p_{\text{atom}} - p_{\text{cavity}}$, where p_{atom} and p_{cavity} are respectively the rate for atomic spontaneous emission or cavity decay given by $\gamma_{\text{eff}}/\Omega_{\text{eff}} \sim \Omega\gamma/(\Delta g)$ and $\kappa/\Omega_{\text{eff}} \sim \Delta\kappa/(\Omega g)$. The maximum for the fidelity therefore is approximately given by $F \leq 1 - 2\sqrt{p_{\text{atom}}p_{\text{cavity}}} = 1 - 2\sqrt{\kappa\gamma/g^2}$, and occurs roughly when $p_{\text{atom}} \sim p_{\text{cavity}}$, or $\gamma_{\text{eff}} \sim \kappa$, not within the bad cavity limit.

We have performed extensive numerical simulations to check this understanding. First for the Raman scheme and a constant Ω, we define *success rate* (Fig. 2.4) [82] as the conditional probability for the atom to end up in state $|g_2\rangle$ staring from state $|g_1\rangle$, *i.e.*, conditional to the system experiencing no spontaneous emission from either the atom or the cavity. The numerical results are given in Fig. 2.4, which shows a weak dependence on the classical field detuning Δ. Typically, we find the optimal condition corresponds to $\Omega/\Delta \sim 0.2 - 0.75$.

The second figure of merit applies to the operation of the atom + cavity system as a photon gun, the aim of our proposed model. In this case, the probability of emission, or
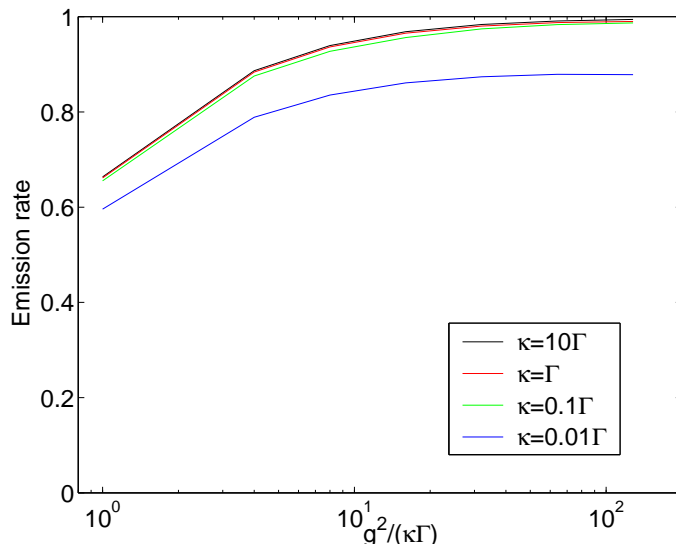
Figure 2.5: The optimal photon-gun-quality for $\gamma = (2\pi)20$ (MHz) and $\Delta = 50\gamma$.

the *emission rate*, into the cavity mode is used. In a sense, the emission rate measures the photon-gun-quality. The results from our numerical survey are illustrated in Fig. 2.5. It is interesting to note that the results do depend on the detuning, essentially reflecting an unbalanced choice of κ with γ_{eff}. We also note that together with the probability of the atomic spontaneous emissions, the two add to unity in the long time limit.

Building on several current experiments, it seems possible to achieve $g^2/(\kappa\gamma) = 30$ [97, 98, 99, 100, 101, 102, 103], a condition for very efficient photon gun according to our calculations. In the strong coupling limit, this also becomes a promising parameter regime for converting an atomic qubit into a flying qubit (of 0 and 1 photon).

We have also compared the state mapping Eq. (2.15) with the counter-intuitive pulse sequence for adiabatic passage [95, 104, 105, 106]. The best numerical results are shown in Figs. 2.6 and 2.7, respectively. We note that in this case, the numerical survey is rather cumbersome as we are looking at a three dimensional (Ω, Δ, and γ) optimization search for each data point. The Raman differential detuning is defined as $\delta = (\omega_L - \omega_c) - (\omega_2 - \omega_1)$.

All of the above discussions assume that the atom is motionless in the cavity. Here we briefly discuss the effect of atomic motion on the protocol for atom-photon entanglement. In all current optical cavity QED systems, the coupling strength $g(\vec{r})$ between the quantum cavity field and the atom is position dependent, with $\vec{r}$ being the atomic center of mass
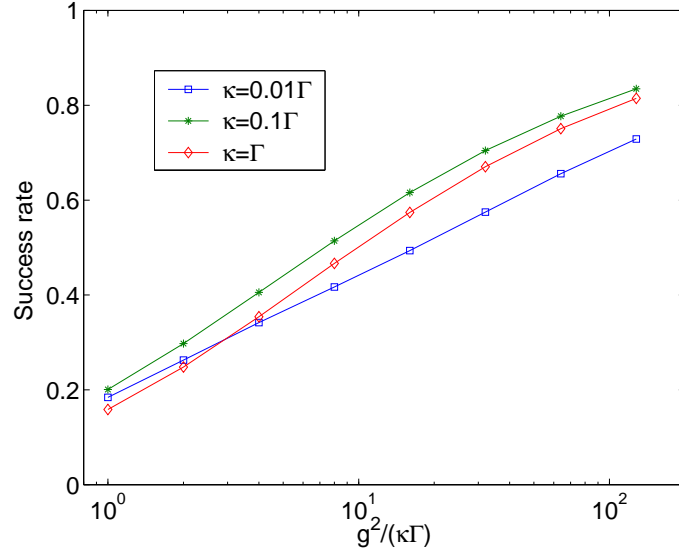
Figure 2.6: The same as in Fig. 2.4 but with the adiabatic passage protocol. The results are optimized and are observed to be less sensitive on the ratio of κ/γ. $\gamma = (2\pi)20$ (MHz).
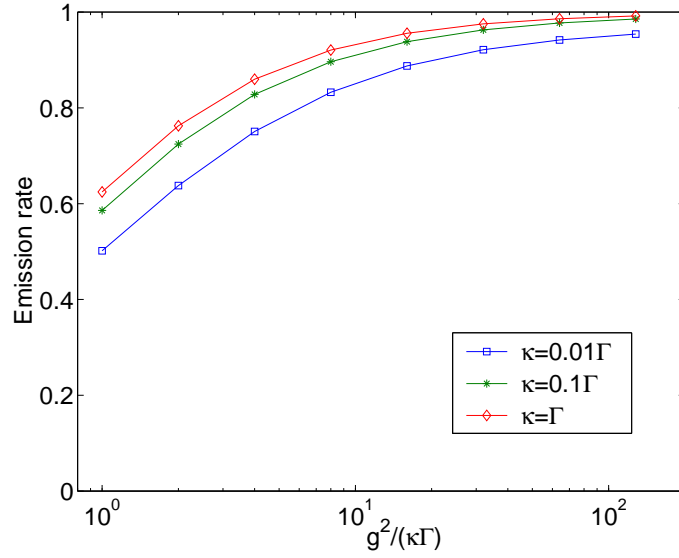
Figure 2.7: The same as in Fig. 2.5 but with the adiabatic passage protocol. The results are optimized and for $\gamma = (2\pi)20$ (MHz).

coordinate. The variation of $g(\vec{r})$ due to the standing wave cavity mode along the cavity axis leads to entanglement between the atomic motion and its internal state, which in the extreme case can cause a complete loss of coherence/entanglement between the atom and the emitted photon, if the atomic center of mass wave packet is delocalized to a size δr comparable to or larger than the cavity mode wavelength λ_c. Typically, one requires the so-called Lamb-Dicke limit [107, 108], or $\delta r \ll \lambda_c$, to enforce an approximately constant $g(\vec{r})$ over the whole atom. A small size wave packet can be prepared by cooling the atomic motion to the ground state of an external harmonic trap as for trapped ions. In this limit, effects of atomic recoil become negligible, as the recoil energy is much less than the trap excitation quanta. The dependence of the fidelity for the state transfer protocol Eq. (2.15) on the Lamb-Dicke parameter $\eta_c = 2\pi\delta r/\lambda_c$ has already been extensively investigated before with numerical simulations [109]. For the application of the recently suggested motional insensitive dark state protocol [110, 111] to state transfer Eq. (2.15), non-adiabatic motional effects have also been studied in great detail [112].

2.4   Conclusion

In conclusion, we have proposed a simple but efficient model for a deterministic generation of atom-photon entanglement. Our scheme is based on an optical cavity QED and can be realized with state-of-the-art technology. The generated atom-photon entangled state can be utilized in quantum information and communication where the photon acts as the information carrier and the atom stores the information. We also discuss the condition for a high fidelity quantum computing protocols in terms of quantum information exchange between an atomic qubit and a cavity. With the controllability of entanglement distributed to a distant party, it is of potential interest to build a quantum network. Successfully generating controlled interactions between a single trapped atom and a cavity photon will represent an important milestone in quantum information physics.

CHAPTER III

PHOTON-PHOTON ENTANGLEMENT GENERATION IN A CAVITY QED SYSTEM

3.1 Introduction

In this chapter, we are going to discuss how to generate photon-photon entanglement. Entangled photon pairs are viewed as essential resources in linear optics quantum computation, as well as in quantum information and communication. Until very recently, most experimental realization of photonic entangled states came exclusively from parametric down conversion (PDC) using nonlinear crystals, where a single pump photon spontaneously converts into two correlated photons satisfying energy and momentum conservation [25, 26, 27, 28, 29, 30, 31]. The stochastic nature and the very low probability of this process due to the very small nonlinearity make it less suitable for quantum information and communication. PDC becomes especially ineffective when adopted for the linear optical approach to quantum computation [113, 114, 115]. Thus, generating deterministic entangled photon pairs has become a pressing need.

The topic of this chapter is devoted to the generation of photon-photon entangled states again in a cavity QED system. The basic ingredient is the atom-photon interaction as shown in the previous chapter. By appropriately adjusting the system parameters, the final state of the atom becomes disentangled with the generated photons, thus creating an almost maximally entangled photon pair.

3.2 A model system

Our model system is sketched in Fig. 3.1. We utilize an atom with level structure of an $F = 1 \rightarrow F' = 1$ structure as shown in Fig. 3.2. Each Zeeman sublevel is denoted as $|Fm_F\rangle(|F'm'_F\rangle)$, further simplified as $|g_{m_F}\rangle = |Fm_F\rangle$ and $|e_{m'_F}\rangle = |F'm'_F\rangle$. The transition frequency between $F = 1$ and $F' = 1$ is labelled as ω_A. As the atom falls through an

optical cavity, it interacts first with the cavity mode field (with frequency ω_C), then with a classical pump field π-polarized with respect to the cavity axis and propagating along a perpendicular direction. We utilize two orthogonal polarizations of the same resonant cavity mode. Similar model systems were invoked previously in Ref. [105], where Lange *et al.* proposed a scheme for generating Greenberger-Horne-Zeilinger (GHZ) photon multiplets by an adiabatic passage protocol and in Refs. [116, 117, 118], where the entanglement of two modes in one or two cavities was investigated.
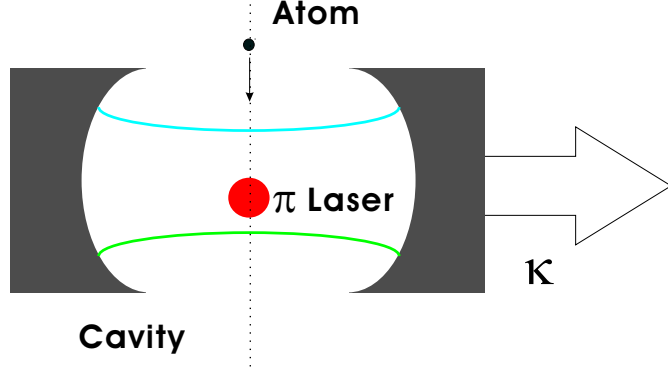
Figure 3.1: The illustration of the proposed cavity QED setup.
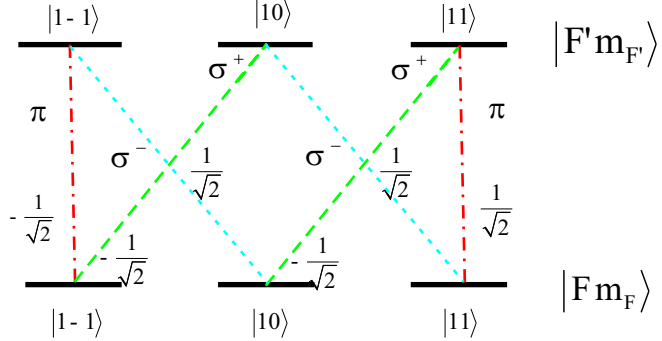
Figure 3.2: The proposed coupling scheme: the vertical dashed-dot lines denote the π-polarized pump field, while the tilted lines denote the left (dotted lines for σ^-) and right (dashed lines for σ^+) polarized cavity fields. The various Clebsch-Gordon coefficients are also indicated.

We assume an initially empty cavity and prepare the atom in the excite state $|e_0\rangle$ before it enters the cavity mode [119]. Based on the interaction sequence, the atom's passage through the cavity can now be divided into two parts. In the first part, the atom only interacts with the cavity mode, and does not enter the area of the π-polarized pump field.

Thus, the excited atom first emits a photon, entangled with the atom in ground states as discussed in the previous chapter [120]. In the second part, the atom is subsequently excited by the pump, emits a second photon, and swaps its entanglement with the first photon (already outside the cavity) to the second photon. The whole process now generates an entangled photon pair. We will analyze this protocol including both atomic and cavity decays. In the interaction picture to the Hamiltonian

$$H_0 = \hbar\omega_C \sum_{m_{F'}} |e_{m_{F'}}\rangle\langle e_{m_{F'}}| + \hbar\omega_C(a_L^\dagger a_L + a_R^\dagger a_R) \tag{3.1}$$

of the atom plus the cavity, our system dynamics are governed by $H = H_1 + H_2$, with

$$H_1 = -\hbar\Delta \sum_{m_{F'}} |e_{m_{F'}}\rangle\langle e_{m_{F'}}| + \frac{1}{2}\hbar[\Omega(t)A_{10}^\dagger + H.c.] \tag{3.2}$$

and

$$H_2 = \frac{1}{2}\hbar g(t)(A_{11}^\dagger a_R + A_{1-1}^\dagger a_L + H.c.). \tag{3.3}$$

Hereafter, $H.c.$ denotes Hermitian conjugate. The second term of H_1 is from the interaction of the atom with the pump field and H_2 denotes the interaction of the atom with the left and right circularly polarized cavity modes. $\Delta = \omega_C - \omega_A$ is the detuning, and for simplicity the pump field is assumed to be resonant with the cavity mode. The atom field coupling coefficients are

$$g(t) = -\mathcal{E}(\vec{R})\langle F'||d_1||F\rangle, \tag{3.4}$$

$$\Omega(t) = -E(\vec{R})\langle F'||d_1||F\rangle, \tag{3.5}$$

where $\langle F'||d_1||F\rangle$ is the reduced dipole matrix element according to Wigner-Eckart theorem, and $\mathcal{E}(\vec{R})$ and $E(\vec{R})$ are respectively the spatial profiles of the cavity mode and the pump field. The atomic raising operators are defined as

$$A_{1q}^\dagger = \sum_{m_F, m_{F'}} \langle F'm_{F'}|Fm_F 1q\rangle|F'm_{F'}\rangle\langle Fm_F|. \tag{3.6}$$

According to the previous prescription, the interaction parameters take the following time dependence

$$g(t) = gh(t)h(T - t), \tag{3.7}$$

$$\Omega(t) = \Omega h(t - t_1)h(t_2 - t), \tag{3.8}$$

22

with the heaviside step function $h(t) = 0$ for $t < 0$ and $h(t) = 1$ for $t \geq 0$. The different times have the following meanings: the atom enters the cavity at time 0, arrives at the pump laser at time t_1, leaves the pump at time t_2, and finally exits the cavity at time T.

Dissipations are essential to our protocol as they allow the excited atom to decay and the cavity photons to be emitted. Their effects on the dynamics can be included straightforwardly using a master equation

$$\dot{\rho} = -i[H, \rho] + D\rho + C\rho, \tag{3.9}$$

where the dissipative terms of the cavity and atom are

$$D\rho = \kappa \sum_{\xi=R,L} (2a_\xi \rho a_\xi^\dagger - a_\xi^\dagger a_\xi \rho - \rho a_\xi^\dagger a_\xi), \tag{3.10}$$

$$C\rho = \frac{\gamma}{2} \sum_q (2A_{1q} \rho A_{1q}^\dagger - A_{1q}^\dagger A_{1q} \rho - \rho A_{1q}^\dagger A_{1q}). \tag{3.11}$$

2κ is the one side decay rate of the cavity, while the other side of the cavity is assumed perfectly reflecting. γ is the decay rate for the atomic excited state $|e_{m_{F'}}\rangle$.

The initial state of our system is now $|\psi(0)\rangle = |e_0, 0_L, 0_R\rangle$, and the rate of cavity photon emission with polarization ξ at time t is $p_\xi(t) = 2\kappa\langle a_\xi^\dagger(t)a_\xi(t)\rangle$. The probability of cavity photon emission is then $P_\xi(t) = 2\kappa \int_0^t dt' \langle a_\xi^\dagger(t')a_\xi(t')\rangle$. We require that the cavity photon be emitted as soon as it is generated, thus the preferred operating condition is close to the bad cavity limit ($\gamma \ll g^2/\kappa \ll \kappa$) as for a single photon source [82, 120, 121]. In fact, as we experienced in the previous chapter, we find that it is desirable to operate with $\kappa \sim g \gg \gamma$, a compromise between the bad cavity and the strong coupling limit, due to the necessity of coherently pumping the atom to the excited state for a second photon.

To gain more insight, we describe the dynamic evolution using the non-Hermitian effective Hamiltonian

$$H_{\text{eff}} = H - i\kappa(a_L^\dagger a_L + a_R^\dagger a_R) - i\frac{\gamma}{2} \sum_q |e_q\rangle\langle e_q|. \tag{3.12}$$

Such an approach is appropriate, as re-excitations of the decayed atom due to emitted photons are negligible, and re-absorptions of the cavity photons can be neglected due to their fast decays to the outside of the cavity. For $t \in [0, t_1]$, the system state is approximately

$$|\psi(t)\rangle = d_0(t)|e_0, 0_L, 0_R\rangle + c_{-1}(t)|g_{-1}, 0_L, 1_R\rangle + c_1(t)|g_1, 1_L, 0_R\rangle. \tag{3.13}$$

The effective Schrödinger equation becomes

$$i\frac{d}{dt}\begin{pmatrix} d_0(t) \\ c_{-1}(t) \\ c_1(t) \end{pmatrix} = \begin{pmatrix} -\Delta - i\frac{\gamma}{2} & -\frac{g}{\sqrt{2}} & \frac{g}{\sqrt{2}} \\ -\frac{g}{\sqrt{2}} & -i\kappa & 0 \\ \frac{g}{\sqrt{2}} & 0 & -i\kappa \end{pmatrix}\begin{pmatrix} d_0(t) \\ c_{-1}(t) \\ c_1(t) \end{pmatrix},$$

which is solved to give

$$c_1(t) = -\frac{ig}{\sqrt{2}}\frac{e^{s_1 t} - e^{s_2 t}}{s_1 - s_2}, \tag{3.14}$$

on making use of the property $c_1(t) = -c_{-1}(t)$. s_1 and s_2 are the roots of equation

$$2s^2 + (2\kappa + \gamma - i2\Delta)s + \gamma\kappa + 2g^2 - i2\kappa\Delta = 0. \tag{3.15}$$

Identical coupling is assumed for both polarization modes, and thus $p_R(t) = p_L(t) = 2\kappa|c_1(t)|^2$. When the time before the pump excitation is so long that the excited atom (in $|e_0\rangle$) completely decays into ground states and the cavity photon completely leaks out, the final state of the atom plus the cavity modes becomes a mixed state

$$\rho(t_1) = \frac{1}{2}|g_{-1}, 0_L, 0_R\rangle\langle g_{-1}, 0_L, 0_R| + \frac{1}{2}|g_1, 0_L, 0_R\rangle\langle g_1, 0_L, 0_R|, \tag{3.16}$$

as the first photon is traced out after being emitted into modes outside the cavity.

For $t \in (t_1, t_2]$, the initial state (3.16) is now completely mixed, so we can evolve its different decompositions respectively. In the first case for $|\psi(t_1)\rangle = |g_1, 0_L, 0_R\rangle$, the state can be approximately expanded as

$$|\psi(t)\rangle = d_1(t)|e_1, 0_L, 0_R\rangle + c_0(t)|g_0, 0_L, 1_R\rangle + c_1(t)|g_1, 0_L, 0_R\rangle, \tag{3.17}$$

and governed by an effective Schrödinger equation

$$i\frac{d}{dt}\begin{pmatrix} d_1(t) \\ c_0(t) \\ c_1(t) \end{pmatrix} = \begin{pmatrix} -\Delta - i\frac{\gamma}{2} & -\frac{g}{\sqrt{2}} & \frac{\Omega}{\sqrt{2}} \\ -\frac{g}{\sqrt{2}} & -i\kappa & 0 \\ \frac{\Omega}{\sqrt{2}} & 0 & 0 \end{pmatrix}\begin{pmatrix} d_1(t) \\ c_0(t) \\ c_1(t) \end{pmatrix}.$$

The solutions for $d_1(t)$ and $c_0(t)$ are again analytic and expressed in terms of the roots s_1, s_2, and s_3 of equation

$$2s^3 + (2\kappa + \gamma - i2\Delta)s^2 + (\Omega^2 + \kappa\gamma + g^2 - i2\Delta\kappa)s + \Omega^2\kappa = 0. \tag{3.18}$$

24

Finally after the atom passes through the π-polarized pump field, we find

$$c_0(t) = c_0\left(t_2\right)\left(\frac{s_1 - s_3}{s_1 - s_2}e^{s_1(t-t_2)} + \frac{s_2 - s_3}{s_2 - s_1}e^{s_2(t-t_2)}\right),$$

where s_1 and s_2 are the roots of equation

$$2s^2 + (2\kappa + \gamma - i2\Delta)\,s + g^2 + \kappa\gamma - i2\kappa\Delta = 0, \qquad (3.19)$$

and $s_3 = -\gamma/2 + i\Delta - ig\sqrt{2}d_1(t_2)/[2c_0(t_2)]$. The emission rate of a second photon with right circular polarization during $[t_1, T]$ is therefore $p_R(t) = \kappa|c_0(t)|^2$.
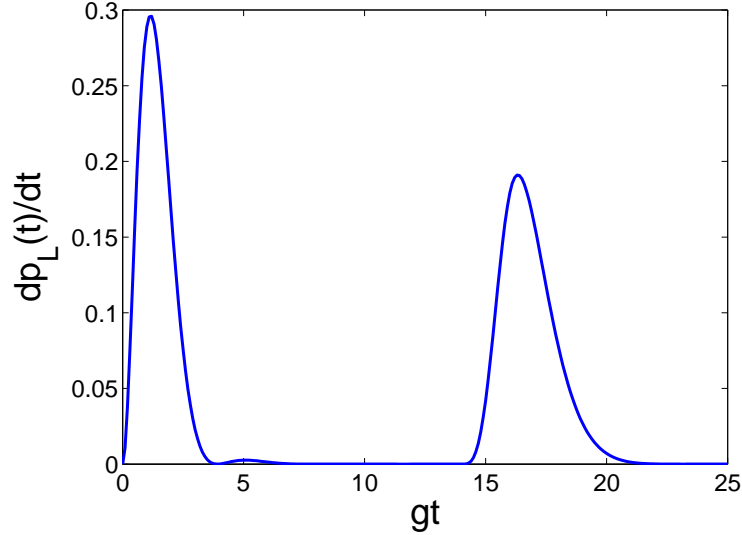
Figure 3.3: The emission rate of a cavity photon with left circular polarization at time t based on solving the master equation (3.9).

3.3 Numerical results

We now compare the above analytical analysis with numerical solutions from the master equation (3.9) and the effective non-Hermitian Hamiltonian (3.12). For the parameter ranges considered, the two numerical approaches give the same results as the analytical one. We find a high fidelity EPR entangled photon pair of the form ($\uparrow \rightarrow 1_L$ and $\downarrow \rightarrow 1_R$) is
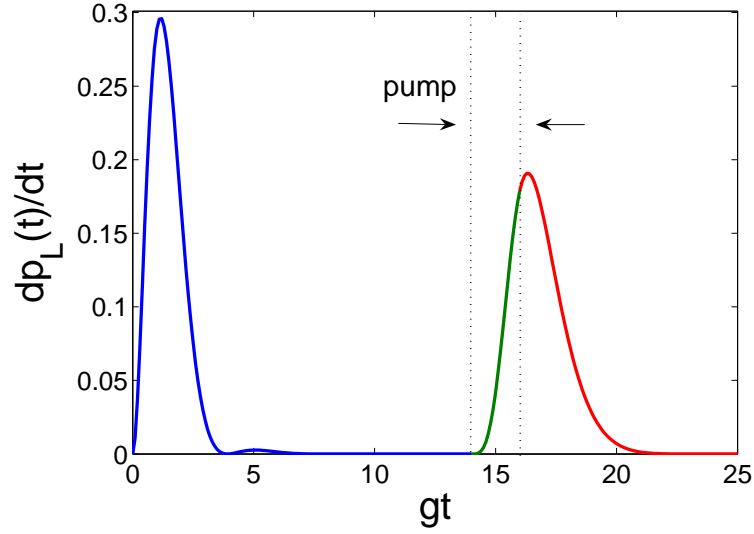
Figure 3.4: The same as Fig. 3.3 but based on the analytic solution to the non-Hermitian Hamiltonian (3.12).

generated with a high efficiency. Like non-classical photon pairs from an atomic ensemble [122], these two photons are distinguishable from their temporal order [123], and can be individually addressed to confirm their EPR correlation.

We have used dimensionless parameters $\Delta = 0$, $g = 1.0$, $\gamma = 0.01$, $\kappa = 1.2$, $\Omega = 1.2$, $t_1 = 14$, $t_2 = 16$, and $T = 25$ in the numerical results shown below. Such a set of parameters can be realized with corresponding physical parameters of $\gamma = (2\pi)\, 0.2$ MHz, $g = (2\pi)\, 20$ MHz, $\kappa = (2\pi)\, 24$ MHz, and $T = 200$ ns [120]. In Figs. 3.3 and 3.4, two single-photon pulses are seen to be emitted sequentially from the cavity. The results from the two numerical approaches agree well with each other. In Fig. 3.5, the probability of generating two single photons are displayed. We see that they are better than 98%. In Fig. 3.6, the occupations of different atomic states are shown. Exactly as expected, the first photon is generated from the decay of the atom in state $|e_0\rangle$ to $|g_1\rangle$ or $|g_{-1}\rangle$, and the second photon is generated from each of these two states when pumped by the π-polarized laser.

Based on our extensive simulation with other parameters, we hope to emphasize three
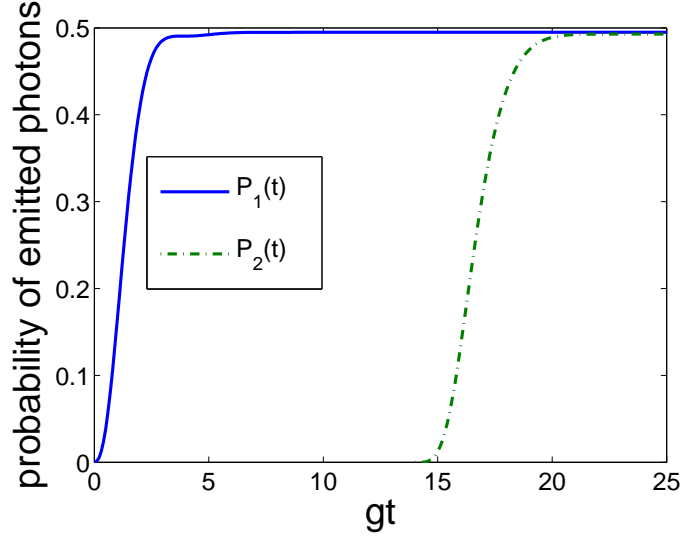
Figure 3.5: The emission probability of the first and second photon of opposite polarization $P_1(t)$ and $P_2(t)$.

points [124]. First, there exists an optimal κ which leads to the fastest photon emission. When $\kappa \ll g$, oscillations emerge, a signature of strong coupling. When $\kappa \gg g$, the probability of emission actually decays linearly and the emission time becomes longer because of the increased bandwidth of the cavity, thus corresponding to reduced strength of emission of the atom into the cavity. Second, there is also an optimal time for the atom to pass the pump laser. When that time is too short, the atom cannot be completely emptied from states $|g_1\rangle$ and $|g_{-1}\rangle$. However, if it is too long, oscillations between states $|e_{\pm 1}\rangle$ and $|g_{\pm 1}\rangle$ arise. More conveniently, it will be desirable to use a trapped atom inside the cavity [125], and replace the transit time over the pump region with a temporal pump pulse. Third, the probability of generating the first photon depends on the atomic decay rate γ. One solution to overcome such a dependence is to use an auxiliary starting state and an additional laser coupled to state $|e_0\rangle$ as in the single photon source protocol [82, 120, 121]. The π-polarization laser then is applied to swap this entanglement from the atom to the second cavity photon. The entanglement of the emitted photon pairs can be easily detected
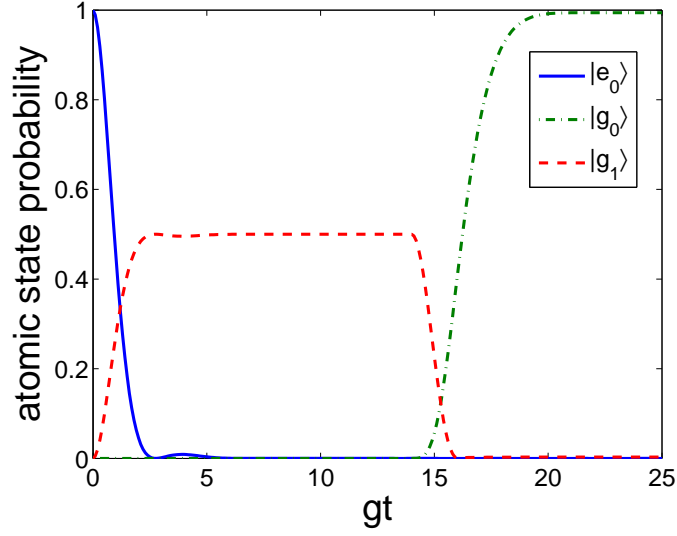
Figure 3.6: The time dependent atomic state populations.

from polarization correlations between the first and second photons using a time resolved detection scheme [123].

Finally, we want to emphasize that dissipations are crucial in our protocol, not only because they lead to the output of cavity photons. Without dissipations, the atom cannot enter the state $|g_0\rangle$, because the quantum amplitudes for the two paths ($|e_0\rangle \rightarrow |g_{-1}\rangle \rightarrow |e_{-1}\rangle \rightarrow |g_0\rangle$ and $|e_0\rangle \rightarrow |g_1\rangle \rightarrow |e_1\rangle \rightarrow |g_0\rangle$) interfere destructively. This balance is broken due to dissipations. We have verified this conclusion numerically. In Fig. 3.7, we show the evolution of atomic state probability for $\kappa = 0$ and $\gamma = 0$. We see the totally different evolution pattern of atomic state probability from the results of Fig. 3.6. First, there are perfect Rabi oscillations between $|e_0\rangle$ and $|g_1\rangle$ when the pump field is absent. Second, the probability of $|e_1\rangle$ starts to change at the pump region, and stays constant after that. Third and the most important, the probability for the atom to return to state $|g_0\rangle$ is indeed 0. In addition, we show the time dependent intracavity photon field in Fig. 3.8. We can see that only a single photon is generated in the whole process. Thus, we conclude that dissipations

are essential to our scheme.
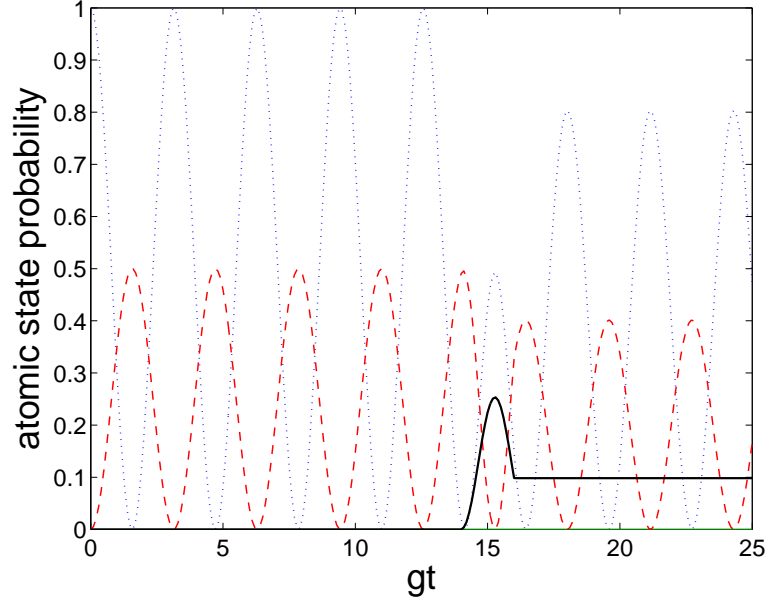
Figure 3.7: The atomic state probability for different energy levels as function of time. The parameters are the same as before except $\kappa = \gamma = 0$. The dotted line is for $|e_0\rangle$, the dashed line is for $|g_1\rangle$, and the solid line is for $|e_1\rangle$. The probability for $|g_0\rangle$ is always 0.

3.4   Modelling the field outside a cavity

A more rigorous formulation is to include the field outside the cavity in the total system dynamics. Different from previous formulations where the environment has been traced out from the system dynamics, here we model the field outside the cavity in terms of continuous one-dimensional plane wave modes [81, 121]. With a high Q cavity in optical frequency region, the outside modes are coupled to the two cavity modes with approximately constant coupling strength [126]. To construct the physical basis for a clear picture of the electric field profiles of the emitted photons, we still use the non-Hermitian effective Hamiltonian to describe the decay of the excited atomic states due to spontaneous emissions. In a more rigorous treatment, we can reproduce the stochastic wave function approach for the conditional dynamics based on continuous photon detections [127]. The system Hamiltonian then becomes

$$H = H_1 + H_2 - i\hbar\frac{\gamma}{2}\sum_q |e_q\rangle\langle e_q| + H_o + H_c, \tag{3.20}$$
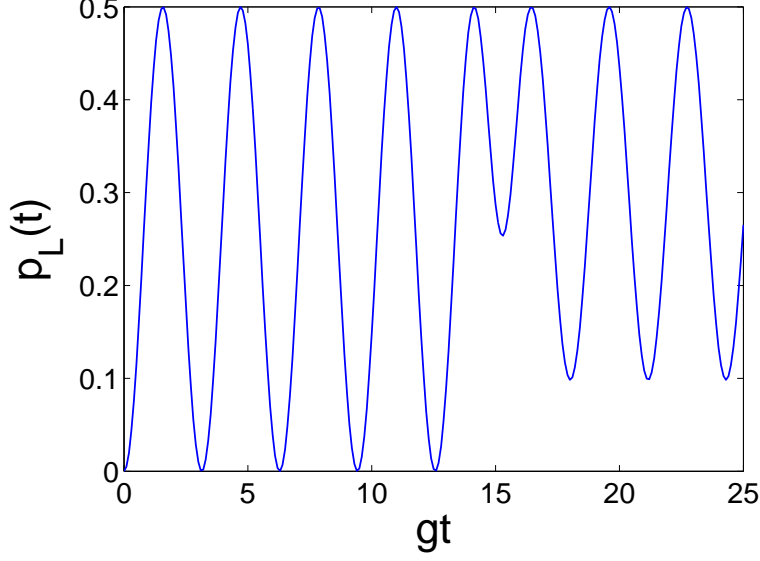
Figure 3.8: Intracavity photon field as function time. The parameters are the same as before except $\kappa = \gamma = 0$.

where H_1 and H_2 are defined in Eqs. (3.2) and (3.3). The free Hamiltonian of the output cavity field is

$$H_o = \int_{-\omega_b}^{\omega_b} d\omega \omega [b_R^\dagger(\omega) b_R(\omega) + b_L^\dagger(\omega) b_L(\omega)], \tag{3.21}$$

and the coupling term between the input and the output cavity field is

$$H_c = i\sqrt{\frac{\kappa}{2\pi}} \int_{-\omega_b}^{\omega_b} d\omega [a_R^\dagger b_R(\omega) - a_R b_R^\dagger(\omega) + a_L^\dagger b_L(\omega) - a_L b_L^\dagger(\omega)]. \tag{3.22}$$

Here $b_\xi(\omega)$ annihilates an outside mode photon with polarization $\xi(= L, R)$ and frequency ω. The commutation relation is $[b_\xi(\omega), b_{\xi'}^\dagger(\omega')] = \delta_{\xi,\xi'}\delta(\omega - \omega')$. We have transformed the frequency $\omega - \omega_C \to \omega$, so the range of the integration of ω is from $-\omega_C$ to $+\infty$. In reality, since only near resonant frequency modes contribute significantly to the system's dynamical evolution, we only need to consider the modes in a finite frequency band $[\omega_C - \omega_b, \omega_C + \omega_b]$. Within this bandwidth, the coupling between the cavity mode a_ξ and the outside mode b_ξ is approximated as a constant, denoted by $\sqrt{\kappa/(2\pi)}$. Quantitatively, the bandwidth ω_b is much larger than the cavity photon decay rate κ and much less than ω_A or ω_C.

For numerical simulations, we model the outside modes with a set of discrete ones. To assure the validity of our numerical simulation, we choose the frequency interval $\delta\omega \ll 1/T$,

where T is the interaction time between the atom and cavity. Then the total mode number for the output field of the cavity is $N = 2\omega_b/\delta\omega$, and the frequency of the j-th mode is $\omega_j = (j - N/2)\delta\omega$.

The initial state of our system is $|e_0; 0_L, 0_R; \text{vac}\rangle$, where the field outside the cavity is assumed to be vacuum. According to the Hamiltonian (3.20), the dynamics of our system are restricted to a finite dimensional subspace of up to two excitations due to the rotating wave approximation. The basis states are therefore

$$|\Xi_1\rangle \equiv |e_0; 0_L, 0_R; \text{vac}\rangle, \ |\Xi_2\rangle \equiv |g_1; 1_L, 0_R; \text{vac}\rangle, \ |\Xi_3\rangle \equiv |g_{-1}; 0_L, 1_R; \text{vac}\rangle,$$

$$|\Xi_4\rangle \equiv |e_1; 1_L, 0_R; \text{vac}\rangle, \ |\Xi_5\rangle \equiv |e_{-1}; 0_L, 1_R; \text{vac}\rangle, \ |\Xi_6\rangle \equiv |g_0; 1_L, 1_R; \text{vac}\rangle,$$

$$|\Xi_7\rangle \equiv |g_1; 0_L, 0_R; 1_{L(\omega)}\rangle, \ |\Xi_8\rangle \equiv |g_{-1}; 0_L, 0_R; 1_{R(\omega)}\rangle,$$

$$|\Xi_9\rangle \equiv |e_1; 0_L, 0_R; 1_{L(\omega)}\rangle, \ |\Xi_{10}\rangle \equiv |e_{-1}; 0_L, 0_R; 1_{R(\omega)}\rangle,$$

$$|\Xi_{11}\rangle \equiv |g_0; 1_L, 0_R; 1_{R(\omega)}\rangle, \ |\Xi_{12}\rangle \equiv |g_0; 0_L, 1_R; 1_{L(\omega)}\rangle,$$

$$|\Xi_{13}\rangle \equiv |g_0; 0_L, 0_R; 1_{L(\omega)}, 1_{R(\omega')}\rangle. \tag{3.23}$$

Here the notation $1_{\xi(\omega)}$ means one outside photon with mode frequency ω and polarization ξ. We thus expand the wave function of the whole system using these basis states with time dependent coefficients

$$|\psi(t)\rangle = \sum_{k=1}^{6} c_k(t)|\Xi_k\rangle + \sum_{k=7}^{12} \int d\omega c_k(\omega, t)|\Xi_k\rangle + \int\int d\omega d\omega' u(\omega, \omega', t)|\Xi_{13}\rangle. \tag{3.24}$$

The corresponding Schrödinger equation gives coupled equations of these coefficients, which can be solved by numerical evolution.

First, let us define the outside mode annihilation operators in the time and frequency domain, respectively,

$$b_\xi(t) = \frac{1}{\sqrt{2\pi}} \int_{-\infty}^{\infty} b_\xi(\omega)e^{-i\omega t}d\omega,$$

$$b_\xi(\omega) = \frac{1}{\sqrt{2\pi}} \int_{-\infty}^{\infty} b_\xi(t)e^{i\omega t}dt \tag{3.25}$$

for polarization $\xi = L, R$. $b(t) = b_L(t) + b_R(t)$. For comparison with the previous results, we numerically evaluate the same quantities with the present method. For example, the

probability for detecting the first photon is approximately given by

$$P_1(t) = \begin{cases} \langle \psi(t)|b^\dagger(0)b(0)|\psi(t)\rangle, & \text{for } t \in [0, t_1], \\ P_1(t_1), & \text{for } t \in [t_1, T], \end{cases} \qquad (3.26)$$

in analogy with the simple approach as used previously. Similarly the probability for detecting the second photon becomes

$$P_2(t) = \begin{cases} 0, & \text{for } t \in [0, t_1], \\ \langle \psi(t)|b^\dagger(0)b(0)|\psi(t)\rangle - P_1(t_1), & \text{for } t \in [t_1, T]. \end{cases} \qquad (3.27)$$

The emission rate of the left circularly polarized photon is
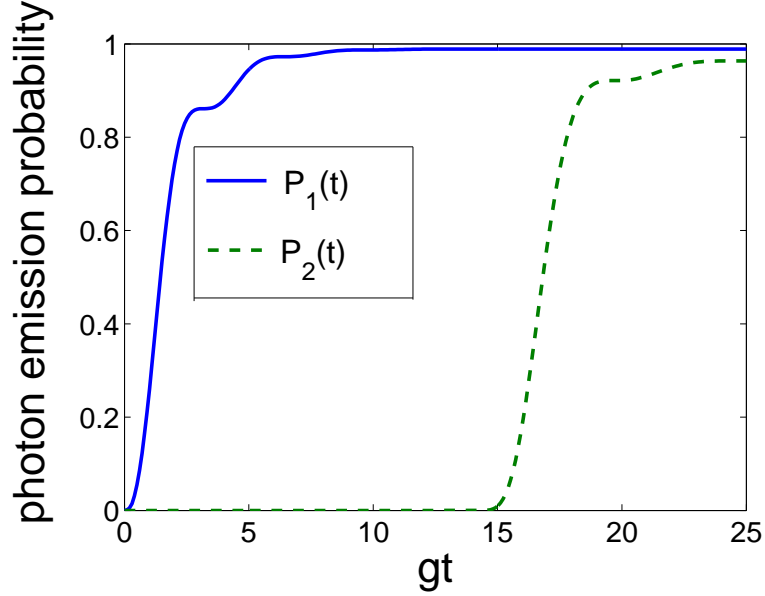
Figure 3.9: The probability of the first and second photon emission $P_1(t)$ and $P_2(t)$. Parameters are the same as before.

$$p_L(t) = \frac{d}{dt}\langle \psi(t)|b_L^\dagger(0)b_L(0)|\psi(t)\rangle. \qquad (3.28)$$

The obvious advantage of the present method is that we can obtain the outside field directly from numerical simulations. The two-photon state is obtained by projecting the final state $|\psi(t)\rangle$ onto the Hilbert space with two outside photons. It is given by

$$|\phi(t)\rangle = \int\int_{-\infty}^{\infty} d\omega d\omega' u(\omega, \omega', t)|g_0; 0_L, 0_R; 1_{L(\omega)}, 1_{R(\omega')}\rangle, \qquad (3.29)$$
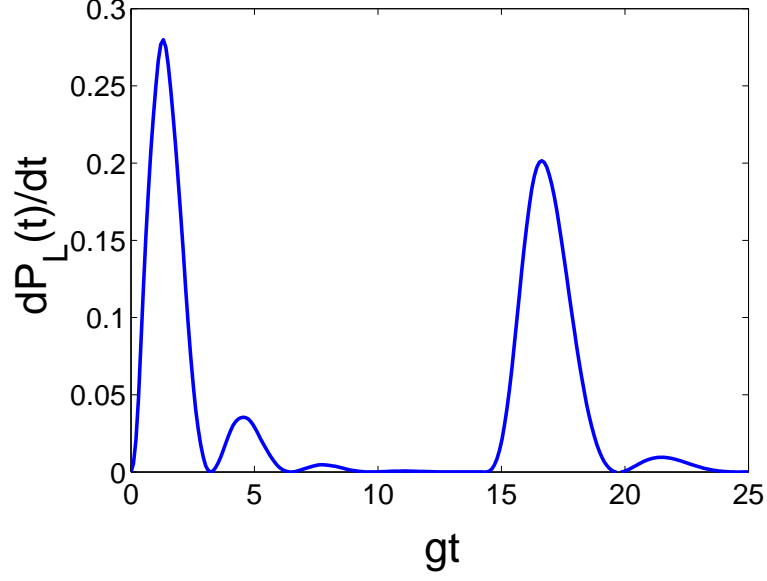
Figure 3.10: The emission rate of a cavity photon with left circular polarization at time t. Parameters are the same as before.

and the probability for outputting two photons from the cavity at time t is

$$P_{LR}(t) = \int\int_{-\infty}^{\infty} d\omega d\omega' \left| u(\omega, \omega', t) \right|^2. \tag{3.30}$$

The numerical result of $P_{LR}(t)$ is shown in Fig. 3.11.

The amplitude of the two-photon wave function at time T is given by

$$\langle g_0; 0_L, 0_R; \text{vac} | b(t) b(t') | \phi(T) \rangle$$

$$= \langle g_0; 0_L, 0_R; \text{vac} | [b_L(t) + b_R(t)][b_L(t') + b_R(t')] | \phi(T) \rangle$$

$$= \langle g_0; 0_L, 0_R; \text{vac} | b_L(t) b_R(t') | \phi(T) \rangle + \langle g_0; 0_L, 0_R; \text{vac} | b_L(t') b_R(t) | \phi(T) \rangle$$

$$= \tilde{u}(t, t', T) + \tilde{u}(t', t, T), \tag{3.31}$$

where

$$\begin{aligned} \tilde{u}(t, t', T) &= \langle g_0; 0_L, 0_R; \text{vac} | b_L(t) b_R(t') | \phi(T) \rangle \\ &= \int\int_{-\infty}^{\infty} d\omega d\omega' u(\omega, \omega', T) e^{-i\omega t - i\omega' t'}. \end{aligned} \tag{3.32}$$

The numerical results for the amplitude of the two-photon wave function are illustrated in Fig. 3.12.

33
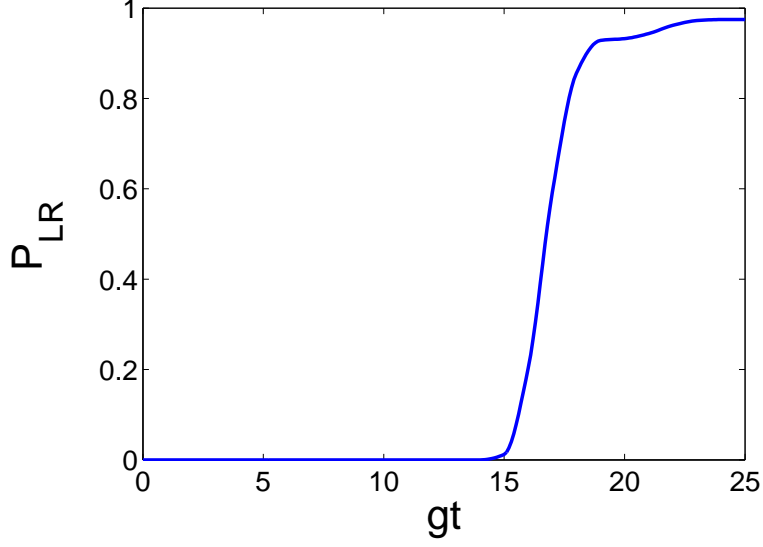
Figure 3.11: The probability of outputting two photons from the cavity at time t. Parameters are the same as before.

We can now discuss under what conditions the time bin entangled EPR photon pairs can be defined explicitly. An obvious requirement is when

$$u(\omega, \omega', T) = \alpha(\omega)\beta(\omega') + \beta(\omega)\alpha(\omega'), \tag{3.33}$$

Then

$$\tilde{u}(t, t', T) = \tilde{\alpha}(t)\tilde{\beta}(t') + \tilde{\beta}(t)\tilde{\alpha}(t'). \tag{3.34}$$

$\tilde{\alpha}(\tilde{\beta})$ are the Fourier transformation of $\alpha(\beta)$ respectively.

Let $\mathcal{A}$ be the anti-symmetrization operation on the amplitude matrix $\tilde{u}$, *i.e.*,

$$\mathcal{A}[\tilde{u}](t, t', T) = \tilde{\alpha}(t)\tilde{\beta}(t') - \tilde{\beta}(t)\tilde{\alpha}(t'), \tag{3.35}$$

then

$$
\begin{aligned}
\frac{1}{2}\left(\tilde{u} + \mathcal{A}[\tilde{u}]\right) &= \tilde{\alpha}(t)\tilde{\beta}(t'), \\
\frac{1}{2}\left(\tilde{u} - \mathcal{A}[\tilde{u}]\right) &= \tilde{\beta}(t)\tilde{\alpha}(t').
\end{aligned}
\tag{3.36}
$$

Thus, $\tilde{\alpha}(t')$ and $\tilde{\beta}(t)$ can be determined from

$$
\begin{aligned}
\int dt' \frac{1}{2}\left(\tilde{u} + \mathcal{A}[\tilde{u}]\right)\tilde{\alpha}(t') &= 0, \\
\int dt \frac{1}{2}\left(\tilde{u} + \mathcal{A}[\tilde{u}]\right)\tilde{\beta}(t) &= 0,
\end{aligned}
\tag{3.37}
$$

34
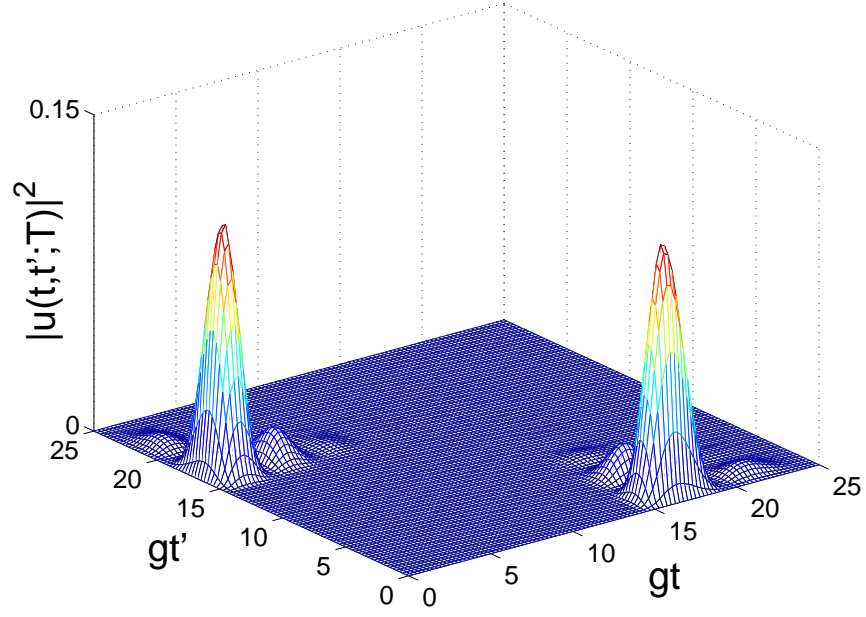
Figure 3.12: The amplitude of the two-photon wave function at time T. Parameters are the same as before.

assuming $\tilde{\alpha}(t)$ and $\tilde{\beta}(t)$ do not overlap. This means $\tilde{\alpha}(t)$ and $\tilde{\beta}(t)$ are the left and right eigenvector of $(\tilde{u} + \mathcal{A}[\tilde{u}])/2$, respectively.

The final state becomes

$$
\begin{aligned}
|\phi(T)\rangle &= \int\int_{-\infty}^{\infty} dt dt' [\tilde{\alpha}(t)\tilde{\beta}(t') + \tilde{\beta}(t)\tilde{\alpha}(t')] b_L^\dagger(t) b_R^\dagger(t') |g_0; 0_L, 0_R; \text{vac}\rangle \\
&= \int\int_{-\infty}^{\infty} dt dt' \tilde{\alpha}(t)\tilde{\beta}(t') [b_L^\dagger(t) b_R^\dagger(t') + b_R^\dagger(t) b_L^\dagger(t')] |g_0; 0_L, 0_R; \text{vac}\rangle. \quad (3.38)
\end{aligned}
$$

Since the time bin distribution functions $\tilde{\alpha}(t)$ and $\tilde{\beta}(t)$ do not overlap, the time bin entanglement of the EPR photon pair is defined explicitly. We have numerically verified the above assumption, and obtained the two time bin distribution functions as in Fig. 3.13, which agree with the earlier results based on simpler approaches, *i.e.*, the non-Hermitian Hamiltonian and density matrix approaches.

From the numerical results, we can see that all three approaches give almost the same results. This in turn proves the accuracy of the density matrix approach and the non-Hermitian Hamiltonian approach. The reason lies in the fact that the intracavity field couples to the outside field with a large number of modes. In the long time limit $(T \gg 1/\kappa)$,
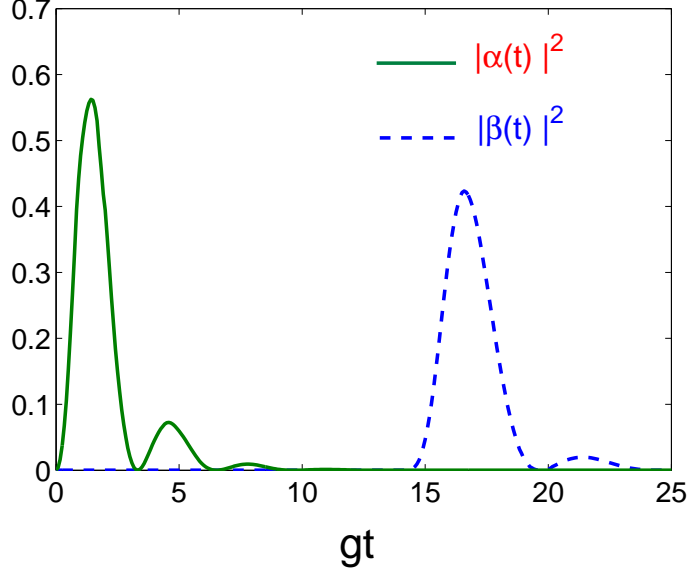
Figure 3.13: The two time bin distribution functions at time T. Parameters are the same as before. $\alpha(t)/\beta(t)$ are the same as $\tilde{\alpha}(t)/\tilde{\beta}(t)$, respectively.

the photon field will distribute over many modes, both inside and outside the cavity. Thus, the intracavity field becomes negligible, and this irreversible process can be well described by a constant κ.

To further explain why the output two-photon state is almost in a maximally entangled state, we follow the method given in Ref. [128] to calculate the entanglement between the two photons. To do so, we project the final state onto the subspace of two outside photons. Such a state is defined in the frequency domain by

$$|\Psi\rangle = \int \int d\omega_1 d\omega_2 A(\omega_1, \omega_2) b_L^\dagger(\omega_1) b_R^\dagger(\omega_2)|\text{vac}\rangle, \tag{3.39}$$

with all of the information contained in the amplitude matrix, $A(\omega_1, \omega_2)$, whose Schmidt decomposition form is then given by

$$A(\omega_1, \omega_2) = \sum_n \sqrt{\lambda_n} \phi_n(\omega_1) \psi_n(\omega_2). \tag{3.40}$$

Here λ_n, $\phi_n(\omega_1)$ and $\psi_n(\omega_2)$ are determined by the following relations,

$$\int K_1(\omega, \omega')\phi_n(\omega')d\omega' = \lambda_n \phi_n(\omega),$$

$$\int K_2(\omega, \omega')\psi_n(\omega')d\omega' = \lambda_n \psi_n(\omega),$$

$$K_1(\omega, \omega') = \int A(\omega, \omega_2)A^*(\omega', \omega_2)d\omega_2,$$

$$K_2(\omega, \omega') = \int A(\omega_1, \omega)A^*(\omega_1, \omega')d\omega_1. \tag{3.41}$$

K_i is nothing but the reduced density matrix for photon i. The natural orbitals ϕ_n and eigenvalues λ_n are obtained by the diagonalization of K_1 or K_2. The natural orbitals of ϕ_n for $n = 1$ and $n = 2$ are shown in Fig. 3.14, corresponding to the two dominant eigenvalues. We find that at final time $t = T$, $\lambda_1 = \lambda_2 \approx 0.4986$, so the fidelity of being in the desired photonic Bell state is around 99.72%. From this result, we conclude that the final state is almost a maximally entangled state.
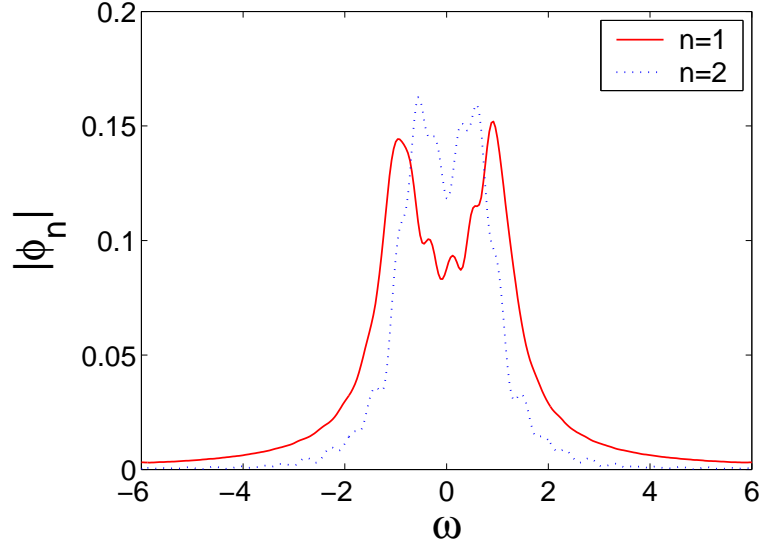
Figure 3.14: Natural orbitals $|\phi_n|$ for $n = 1$ and $n = 2$ respectively. ψ_n is the same as ϕ_n.

3.5   Conclusion

In conclusion, we have proposed a simple but efficient scheme to deterministically generate EPR entangled photon pairs from an atom coupled to a high Q optical cavity. We have performed detailed analysis based on the standard non-Hermitian Hamiltonian and master

equation approaches. By choosing appropriate parameters, our numerical results show a high efficiency for generating a maximally entangled photon pair. In addition, we have also carried out calculations by explicitly including the outside cavity modes in the total system dynamics. This approach allows us to obtain the details of the two-photon state directly. We find good agreement with all three approaches. For the last approach, we have defined a general criterion for a more rigorous characterization of the two-photon pair entanglement. We find that the final state is almost in a maximally entangled state. Compared to the traditional PDC method with very low efficiency, our scheme has the potential for realizing a deterministic source of entangled photon pairs. We hope our study will be helpful in linear optics quantum computation and quantum information science.

This chapter is based on the paper in collaboration with Dr. D. L. Zhou [129].

CHAPTER IV

ENTANGLEMENT BETWEEN TWO ATOMS IN A ONE-DIMENSIONAL HARMONIC TRAP

4.1 Introduction

Experimental development in cold atomic physics has now made it possible to trap atoms in an optical lattice with each lattice site containing several atoms. With the increase of the trap depth, a condensate loaded into a lattice experiences a quantum phase transition, the so-called SF-MI transition [52, 53, 54, 55]. In the MI regime where the tunnelling between neighboring sites is negligible, each lattice site can be viewed as an independent system and the trap potential can sometimes be approximated as harmonic, allowing for an exact analytic treatment. In this chapter, we will therefore limit our study to the simple case of two interacting atoms inside a harmonic trap, focusing on the pair entanglement.

The true interaction potential $V_{\text{int}}(\vec{r})$ between two atoms is generally complicated. For theoretical purposes, $V_{\text{int}}(\vec{r})$ is usually approximated by more amenable forms, which involve a short range strong chemical bonding and a long range van der Waals potential

$$V_{\text{int}}(\vec{r}) \rightarrow -\frac{C_6}{r^6}, \tag{4.1}$$

leading to the van der Waals length scale

$$x_0 = \frac{1}{2} \left(\frac{2\mu C_6}{\hbar^2} \right)^{1/4}. \tag{4.2}$$

For $r \ll x_0$, the scattering wave function oscillates rather rapidly due to the strong attractive interaction potential. In the low energy regime, where two atoms cannot approach each other very closely, there is another length scale $a_0(\gg x_0)$ that comes into play. In this regime, the s-wave scattering dominates, and we can use one single parameter, the s-wave scattering length a_0, to describe this interatomic potential [130]. Further simplification to a contact potential ($\propto a_0 \delta(\vec{r})$) leads to the famous pseudopotential approximation, which has proven very successful in describing dilute atomic systems [131].

We will concentrate on studying the entanglement of two identical atoms in a one-dimensional (1D) harmonic trap. The pair entanglement for two atoms in a three-dimensional (3D) spherical harmonic trap has been investigated in Ref. [59], although only for pure states. The method of Ref. [59] is effective only when the center of mass (CM) motion is in the ground state of the trap. Their extension to a general mixed state with temperature dependence seems difficult due to the very large Hilbert space involved. To uncover the dependence of the pair entanglement on temperature, we instead consider a 1D system to avoid such numerical difficulty. We will explore the dependence of entanglement on the scattering strength and on the temperature. In addition, we also intend to extend the results in Ref. [59] to a general cylindrical harmonic trap, which will be addressed in the next chapter.

4.2   A model system

Our model system consists of two cold atoms interacting via the contact potential in a harmonic trap. First we make clear what a 1D harmonic trap means here. The real experiments involve, of course, 3D traps. A 1D system is achieved by imposing very tight constraints on the transverse directions. The existence of tight transversal confinement will only allow virtual transitions along the transverse directions, leading to a renormalized effective 1D scattering length from the 3D scattering length [132]. The system considered can then be viewed as a quasi one-dimensional system, hereafter referred to as 1D. Such a 1D system possesses some peculiar features, such as "Fermi-Bose duality", only possible in a 1D system.

At very low temperatures, the s-wave scattering is the dominant interaction channel for two identical bosonic atoms. For two identical fermionic atoms, on the other hand, the dominant interaction is p-wave scattering because of the Pauli exclusion principle. Within the pseudopotential approximation, these scattering processes are characterized by the s-wave scattering length a_s and the p-wave scattering volume V_p respectively, which are

defined as

$$a_s = -\lim_{k \to 0} \frac{\tan \delta_s(k)}{k}, \tag{4.3}$$

$$V_p = -\lim_{k \to 0} \frac{\tan \delta_p(k)}{k^3}, \tag{4.4}$$

where $\delta_{s,p}(k)$ is the s/p-wave scattering phase shift. k is the asymptotic scattering momentum.

The above definitions of the scattering length/volume are only valid in the Wigner regime, *i.e.*, $ka_s \ll 1$ or $k^3 V_p \ll 1$. Inside an external trap, this requires that the scattering length be much smaller than the trap width. Otherwise, it should be replaced by an energy dependent scattering length [133, 134]. In this case, the spectrum of the energy dependent Hamiltonian can be solved self-consistently [134]. However, in this chapter, we treat the scattering length/volume as an independent parameter.

For two spinless/polarized bosonic atoms, the effective interaction is found to be [41]

$$V_{\text{int}}^B(x_{12}) = -\frac{2\hbar^2}{ma_{1D}^e}\delta(x_{12}), \tag{4.5}$$

where $x_{12} = x_1 - x_2$ and $a_{1D}^e = -a_\perp^2(1 - c\,a_s/a_\perp)/2a_s$ with a constant $c \simeq 1.4603$, is the effective 1D scattering length for s-wave scattering [132]. $\delta(x)$ is the Dirac δ function. For two spin polarized fermionic atoms, the effective interaction is [135]

$$V_{\text{int}}^F(x_{12}) = \frac{2\hbar^2 a_{1D}^o}{m}\frac{\overleftarrow{d}}{d(x_{12})}\delta(x_{12})\frac{\overrightarrow{d}}{d(x_{12})}, \tag{4.6}$$

where $a_{1D}^o = 6(V_p/a_\perp^2)(1 + c'V_p/a_\perp^3)^{-1}$ with a constant $c' \simeq 2.4948$, is the effective 1D scattering length for p-wave scattering [136, 137]. The arrows indicate the directions of derivative operation. In the following, we will discuss the entanglement properties for these two types of interaction potentials separately.

4.3   Two identical bosonic atoms in a 1D harmonic trap

First we consider the bosonic case. The Hamiltonian is

$$H = \sum_{i=1}^{2}\left(-\frac{\hbar^2}{2m}\frac{d^2}{dx_i^2} + \frac{1}{2}m\omega^2 x_i^2\right) + V_{\text{int}}^B(x_{12}). \tag{4.7}$$

41

Here ω is the external 1D trap frequency. The interaction is given by

$$V_{\text{int}}^B(x_{12}) = -\frac{2\hbar^2}{ma_{1D}^e}\delta(x_1 - x_2). \tag{4.8}$$

The interaction strength is $g_{1D}^B = -2\hbar^2/(ma_{1D}^e)$. Unlike the 3D case, the pseudopotential in 1D does not need regularization [138].

Following the method of Refs. [41, 135], we separate the motion of two bosonic atoms into the center of mass (CM) and the relative (rel) motion, $i.e.$, $H = H_{\text{CM}} + H_{\text{rel}}$, with

$$
\begin{aligned}
H_{\text{CM}} &= -\frac{\hbar^2}{2m}\frac{d^2}{dX^2} + \frac{1}{2}m\omega^2 X^2, \\
H_{\text{rel}} &= -\frac{\hbar^2}{2m}\frac{d^2}{dx^2} + \frac{1}{2}m\omega^2 x^2 + V_{\text{int}}^B(\sqrt{2}x).
\end{aligned} \tag{4.9}
$$

The coordinate transformation is

$$
\begin{aligned}
X &= \frac{x_1 + x_2}{\sqrt{2}}, \\
x &= \frac{x_1 - x_2}{\sqrt{2}}.
\end{aligned} \tag{4.10}
$$

The above Hamiltonian (4.9) commutes with the parity operators of both the CM coordinate $P(X \to -X)$ and the relative coordinate $P(x \to -x)$, which also commutes with each other in harmonic traps. Thus the parities $P(X \to -X)$ and $P(x \to -x)$ of the eigenfunctions are definite, $i.e.$, either odd or even. In this chapter, we will use $\sqrt{\hbar/(m\omega)}$ and $\hbar\omega$ as our length scale and energy scale, respectively. The CM motion is a harmonic oscillator whose dimensionless form is

$$\left(-\frac{1}{2}\frac{d^2}{X^2} + \frac{1}{2}X^2\right)\psi(X) = E\psi(X). \tag{4.11}$$

The solutions are well known, given by

$$\phi_n(X) = \sqrt{\frac{1}{2^n n!\sqrt{\pi}}}e^{-X^2/2}H_n(X), \tag{4.12}$$

where n labels the discrete energy levels and $H_n(X)$ is the n-th order Hermite polynomial. The corresponding eigenenergy is $E_n = n + 1/2$. The parities of these eigenfunctions are $(-1)^n$ under the CM coordinate parity exchange $P(X \to -X)$, and are invariant under particle exchange, $i.e.$, the relative coordinate parity exchange $P(x \to -x)$.

We concentrate on the non-trivial relative motion. The equation is

$$\left(-\frac{1}{2}\frac{d^2}{dx^2} + \frac{1}{2}x^2 - \frac{\sqrt{2}}{a_{1D}^e}\delta(x)\right)\psi(x) = E\psi(x). \tag{4.13}$$

The parity of this Hamiltonian is even under coordinate parity exchange $P(x \to -x)$, so the eigenfunctions should have fixed parities. The odd parity eigenfunctions vanishing at $x = 0$ are unperturbed by the pseudopotential. So $\phi_{2n+1}(x)(n = 0, 1, 2...)$ are the obvious solutions of the above equation. Those even parity eigenfunctions are obtained by expanding the wave function $\psi(x)$ in the complete basis of the harmonic oscillator [41, 135]. The even parity eigenfunctions are found to be

$$\psi_{\nu_e}(x) = \frac{A_{\nu_e}}{\sqrt{\pi}}e^{-\frac{x^2}{2}}\Gamma\left(-\nu_e\right)U\left(-\nu_e, \frac{1}{2}; x^2\right), \tag{4.14}$$

with the relative energy $E_{\nu_e} = 2\nu_e + 1/2$. $\Gamma(x)$ is the gamma function and $U(a, c; x)$ is the confluent hypergeometric function of the second kind [139]. E_{ν_e} and the effective scattering length $1/a_{1D}^e$ are constrained by the following quantization condition

$$\frac{\Gamma(-\frac{E_{\nu_e}}{2} + \frac{3}{4})}{\Gamma(-\frac{E_{\nu_e}}{2} + \frac{1}{4})} = \frac{1}{\sqrt{2}a_{1D}^e}. \tag{4.15}$$

The normalization constant A_{ν_e} is given by

$$A_{\nu_e} = \left(\frac{\Gamma(-\nu_e + \frac{1}{2})}{\Gamma(-\nu_e)}\frac{1}{\mathcal{F}(-\nu_e + \frac{1}{2}) - \mathcal{F}(-\nu_e)}\right)^{\frac{1}{2}}, \tag{4.16}$$

where $\mathcal{F}$ is the digamma function [139]. In particular, when the effective scattering length $1/a_{1D}^e = 0$, all the ν_e's reduce to non-negative integers, and the corresponding eigenfunctions are simply the even parity orbitals of the harmonic oscillator, i.e., $\psi_{\nu_e}(x) = \phi_{2\nu_e}(x)$.

In Fig. 4.1, we show the spectrum for the relative Hamiltonian. The solid curves are for the eigenenergies corresponding to even parity, and the horizontal dotted lines are for unperturbed eigenenergies with odd parity. We can see that the energy is a decreasing function of $1/a_{1D}^e$. Also, we note that there are no level crossing unless $1/a_{1D}^e \to \pm\infty$, where the energy coincides with the odd parity one. An interesting feature is the existence of a single bound state for $1/a_{1D}^e > 0$, which corresponds to the right part of the lowest branch in Fig. 4.1.
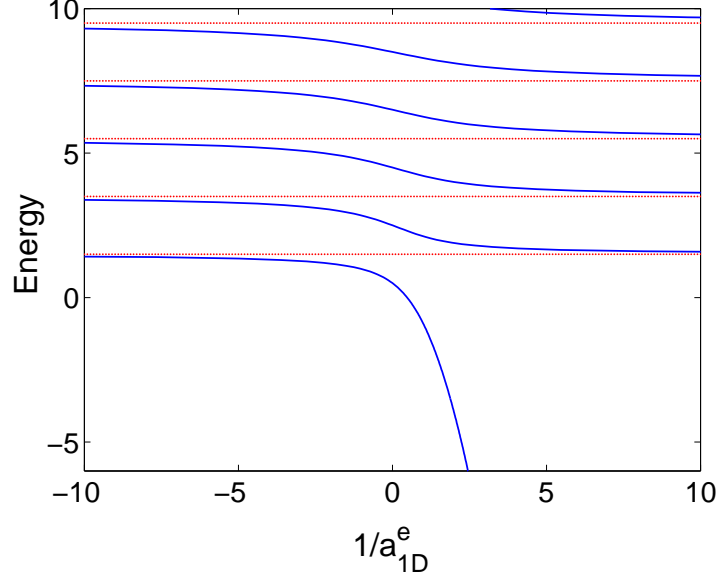
Figure 4.1: Even parity eigenenergies E_{ν_e} (solid) are plotted as function of $1/a_{1D}^e$, and odd parity eigenenergies (dotted) are not affected by $1/a_{1D}^e$.

The monotonicity of the energy versus $1/a_{1D}^e$ can be proved directly from the quantization condition Eq. (4.15). It can also be explained in a simpler way using the Hellman-Feynman theorem [140] as follows:

$$\frac{\partial E_{\nu_e}}{\partial \frac{1}{a_{1D}^e}} = \left\langle \frac{\partial H}{\partial \frac{1}{a_{1D}^e}} \right\rangle$$
$$\rightarrow \quad 2\frac{\partial \nu_e}{\partial \frac{1}{a_{1D}^e}} = \left\langle -\sqrt{2}\delta(x) \right\rangle$$
$$\rightarrow \quad \frac{\partial \nu_e}{\partial \frac{1}{a_{1D}^e}} = -\frac{|\psi_{\nu_e}(0)|^2}{\sqrt{2}}. \tag{4.17}$$

From the energy quantization Eq. (4.15), we can see that for $|1/a_{1D}^e| \ll 1$, the energy shift to the unperturbed trap ground state, the so-called quantum defect, is computed to be $\mu = 2\nu_e = -\sqrt{2/\pi}/a_{1D}^e$, which is the same as the result $\langle 0| - \sqrt{2}/a_{1D}^e\delta(x)|0\rangle$ using the perturbation calculations.

The eigenfunctions of the two lowest eigenstates with even parity are shown in Figs. 4.2 and 4.3 for $1/a_{1D}^e = 1$ and $1/a_{1D}^e = -1$, respectively. We note that all of the wave functions have discontinuous derivatives at $x = 0$, which is due to the scattering term.

By combining the CM and relative motion, the eigenstate of the total Hamiltonian can

44
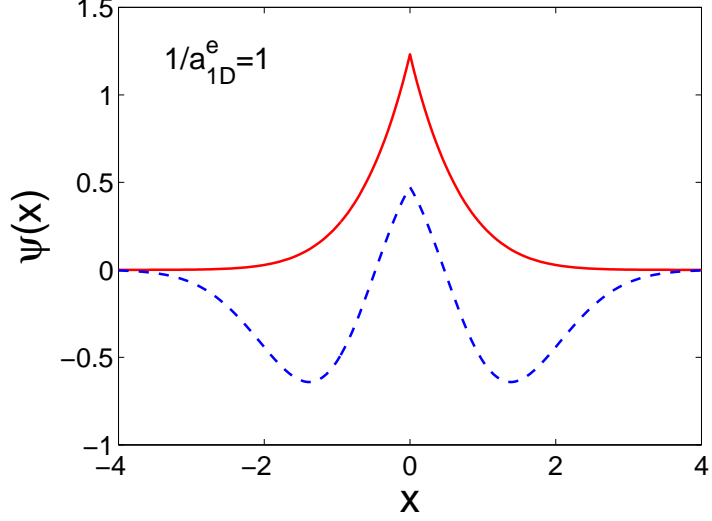
Figure 4.2: Wave functions of the two lowest even-parity eigenstates for $1/a_{1D}^e = 1$. The solid line is for ground state, and the dashed line is for the first excited state with even parity.

be written as

$$
\begin{aligned}
\Psi_{n\nu_e}(x_1, x_2) &= \phi_n(X)\psi_{\nu_e}(x) \\
&= \phi_n\left(\frac{x_1 + x_2}{\sqrt{2}}\right)\psi_{\nu_e}\left(\frac{x_1 - x_2}{\sqrt{2}}\right),
\end{aligned}
\tag{4.18}
$$

with total eigenenergy $E_{n\nu_e} = n + 2\nu_e + 1$. Here ν_e includes eigenvalues of both parities.

4.3.1 Entanglement in the ground state

At $T = 0$, the system is in the ground state, which is given by

$$
\Psi_{0\nu_e^0}(x_1, x_2) = \phi_0(X)\psi_{\nu_e^0}(x),
\tag{4.19}
$$

where ν_e^0 is the minimal value that satisfies the quantization condition (4.15). We can transform the above wave function into the following expression in the single particle basis

$$
\phi_0(X)\psi_{\nu_e^0}(x) = \sum_{pq} \alpha_{pq}\phi_p(x_1)\phi_q(x_2),
\tag{4.20}
$$

with

$$
\alpha_{pq} = \frac{-2}{\pi^{3/4}}\left(\frac{\Gamma(-\nu_e^0 + \frac{1}{2})}{\Gamma(-\nu_e^0)}\frac{1}{\mathcal{F}(-\nu_e^0 + \frac{1}{2}) - \mathcal{F}(-\nu_e^0)}\right)^{\frac{1}{2}}\frac{1 + (-1)^{p+q}}{2}\frac{(-1)^{\frac{p-q}{2}}\Gamma(\frac{p+q+1}{2})}{(2\nu_e^0 - p - q)\sqrt{p!q!}}.
\tag{4.21}
$$

45
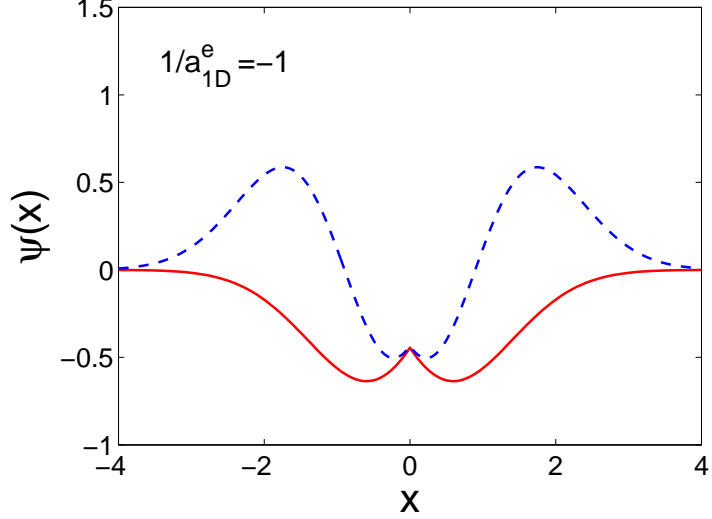
Figure 4.3: Same as Fig. 4.2 except $1/a_{1D}^e = -1$.

The detailed proof can be found in appendix A. For two identical bosonic atoms, we can also write the wave function in the following symmetric form

$$|\phi_0 \psi_{\nu_e^0}\rangle = \frac{1}{\sqrt{2}} \sum_{pq} \alpha_{pq} |pq\rangle, \tag{4.22}$$

here $|pq\rangle = (|p_1 q_2\rangle + |p_2 q_1\rangle)/\sqrt{2}$ and $\langle x|n\rangle = \phi_n(x)$. $|p_i\rangle$ means atom i in the p-th orbital of the harmonic oscillator. The two-atom density matrix is $\rho_B = |\phi_0 \psi_{\nu_e^0}\rangle\langle\phi_0 \psi_{\nu_e^0}|$. Because the two bosonic atoms are identical particles, there is only one single-particle density matrix ρ^b, normalized to one, which is computed to be $\rho^b = (\alpha^\dagger \alpha)^{\mathrm{T}}$ [19]. Here T is the transposition operation on the matrix.

We use von Neumann entropy as a pure state entanglement measure. The Schmidt decomposition of the wave function gives

$$|\phi_0 \psi_{\nu_e^0}\rangle = \frac{1}{\sqrt{2}} \sum_i \sqrt{\lambda_i} |ii\rangle, \tag{4.23}$$

where λ_i's are the eigenvalues of the reduced density matrix and $\sum_i \lambda_i = 1$. Then the entropy of entanglement is

$$\mathbb{E} = -\sum_i \lambda_i \ln(\lambda_i). \tag{4.24}$$

In Fig. 4.4, we show the numerical results for the ground state entanglement for different effective scattering lengths up to ± 10 in arbitrary dimensionless units. As we can see, the

entropy of entanglement increases as $|1/a_{1D}^e|$ increases, irrespective of the signs of their interaction. There are also some limiting cases which are very interesting and will be discussed later.
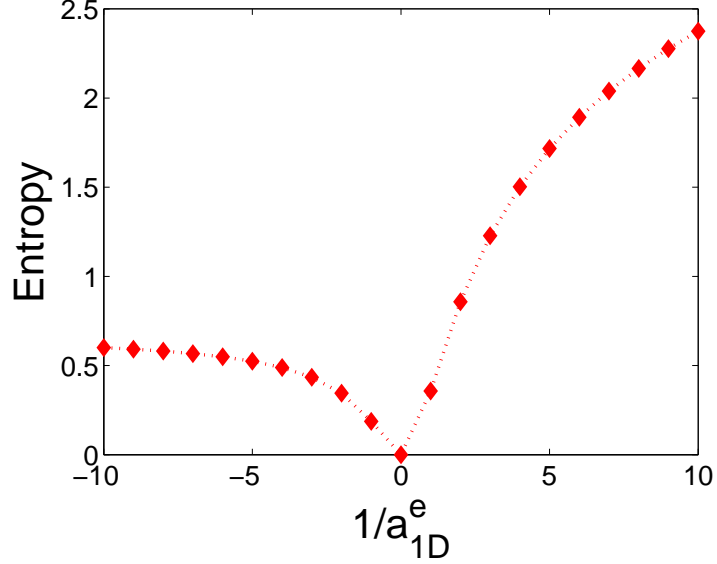
Figure 4.4: Entropy of entanglement versus effective scattering length $1/a_{1D}^e$ at $T = 0$. As $1/a_{1D}^e$ approaches $-\infty$, entanglement saturates to about 0.683. When $1/a_{1D}^e$ approaches $+\infty$, entanglement increases without limit.

For comparison, we use another more intuitive pure state entanglement measure which is based on geometric considerations. This quantity turns out to be calculable in our case. For any pure state $|\psi\rangle$, we can use a separable pure state $|\phi\rangle$ and define its entanglement via the distance $d = \min_{|\phi\rangle}|||\phi\rangle - |\psi\rangle||$. Equivalently, define $\Lambda_{\max} = \max_{|\phi\rangle}||\langle\phi|\psi\rangle||$ under the constraint $\langle\phi|\phi\rangle = 1$. We adopt $\mathbb{E}_{\sin^2} = 1 - \Lambda_{\max}^2$ as our entanglement measure [141]. In our case, we assume $|\phi\rangle = \bigotimes_{i=1}^2 \sum_p \eta_p|p_i\rangle$ with $\sum_p |\eta_p|^2 = 1$. The reason we use the same coefficients η_p for different atoms is that $|\psi\rangle$ is symmetric under atom interchange. So we expect that the state maximizing the above expression should also be symmetric. This reduces the necessary number of variables in the maximization. We also note that the maximization shall occur for real optimization parameters. Now $\Lambda_{\max} = \max_{|\phi\rangle}||\langle\phi|\psi\rangle|| = \max_{\eta_p}|\sum_{pq} \eta_p\eta_q\alpha_{pq}|$. α is a real symmetric matrix, which results in $\alpha_{pq} = \sum_k U_{pk}A_k U_{kq}^T$, with U being an orthogonal matrix. So $\Lambda_{\max} = \max_{\eta_p}|\sum_k A_k \sum_p U_{pk}\eta_p \sum_q U_{kq}^T\eta_q| = \max_{\xi_k}|\sum_k A_k\xi_k^2|$ under the constraint $\sum_k |\xi_k|^2 = 1$. It's obvious $\Lambda_{\max} \leqslant (\max|A_k|)\sum_k |\xi_k|^2 = \max|A_k|$. In Fig. 4.5,

we show the dependence of $\mathbb{E}_{\sin^2}$ on the effective scattering length. Not surprisingly, we find that the curve has the same behavior as entropy because the geometric one is also an entanglement measure.
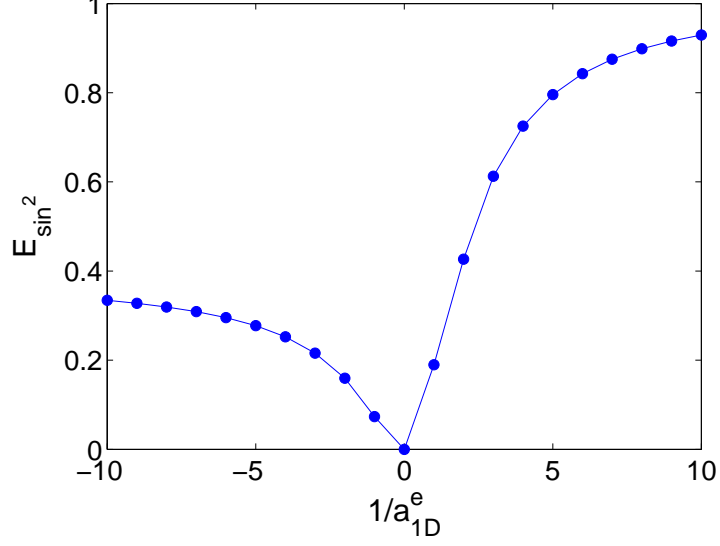
Figure 4.5: $\mathbb{E}_{\sin^2}$ as function of the effective scattering length.

4.3.2 Entanglement at finite temperatures

When $T > 0$, the system is in thermal equilibrium. In general, it is a mixed state described by the density matrix

$$\rho_e(T) = \frac{e^{-\beta H}}{\text{Tr}(e^{-\beta H})}, \tag{4.25}$$

where $\beta = 1/(k_B T)$.

Expanding the density matrix in the eigenstates of H and further transforming it into the single particle basis, we obtain

$$
\begin{aligned}
\rho_e(T) &= \sum_{n\nu_e} P_{n\nu_e}(T)|\Psi_{n\nu_e}\rangle\langle\Psi_{n\nu_e}| \\
&= \sum_{pq;p'q'} \left(\sum_{n\nu_e} P_{n\nu_e}(T)\alpha_{pq}^{(n\nu_e)} \left(\alpha_{p'q'}^{(n\nu_e)} \right)^* \right) |p_1 q_2\rangle\langle p_1' q_2'| \\
&= \sum_{pq;p'q'} \rho_{pq;p'q'}|p_1 q_2\rangle\langle p_1' q_2'|,
\end{aligned}
\tag{4.26}
$$

with the thermal distribution $P_{n\nu_e}$ given by

$$P_{n\nu_e}(T) = \frac{e^{-(n+\nu_e)/T}}{\sum_{n\nu_e} e^{-(n+\nu_e)/T}}. \tag{4.27}$$

Here we have used the temperature scale $\hbar\omega/k_B$. The density matrix elements in the single particle basis are given by

$$\rho_{pq;p'q'} = \sum_{n\nu_e} P_{n\nu_e}(T) \alpha_{pq}^{(n\nu_e)} \left(\alpha_{p'q'}^{(n\nu_e)} \right)^*. \tag{4.28}$$

To calculate the entanglement for a mixed state, we adopt negativity [22] as our entanglement measure, which makes use of partial transposition of the density matrix. In this case, the partial transposition of the density matrix gives

$$\rho_e^{\mathrm{T}_1} = \sum_{pqp'q'} \rho_{p'q;pq'} |p_1 q_2\rangle \langle p'_1 q'_2|. \tag{4.29}$$

Here T_i means the transposition with respect to the i-th subsystem. After rearranging the basis order, we have

$$\rho_{pq;p'q'}^{\mathrm{T}_1} = \sum_{n\nu_e} P_{n\nu_e} \alpha_{p'q}^{(n\nu_e)} \left(\alpha_{pq'}^{(n\nu_e)} \right)^*. \tag{4.30}$$

We calculate the negativity of $\rho_e^{\mathrm{T}_1}$ by direct diagonalization for various T and $1/a_{1D}^e$. The numerical results are shown in Fig. 4.6. Here we emphasize two points. First, negativity at $T = 0$ resembles the von Neumann entropy. This means that negativity can also be used as a pure state entanglement measure. Actually, for a pure state with Schmidt decomposition $|\Psi\rangle_{12} = \sum_k c_k |\phi_k\rangle_1 |\psi_k\rangle_2$, we have $\mathbb{N} = [(\sum_k c_k)^2 - 1]/2$ [142]. Second, negativity decreases as temperature increases, which is consistent with our intuitive understanding that temperature acts as noise to deteriorate quantum correlation. This is in stark contrast to von Neumann entropy, which increases with temperature and is shown in Fig. 4.7. It's not surprising that the entanglement does not show any "sudden death" [143, 144], since we are dealing with two atoms, each containing infinite energy levels.

4.3.3 Some limiting cases of ground state entanglement

We discuss some limiting cases in this section: $1/a_{1D}^e = 0$, $1/a_{1D}^e \to -\infty$, and $1/a_{1D}^e \to +\infty$.
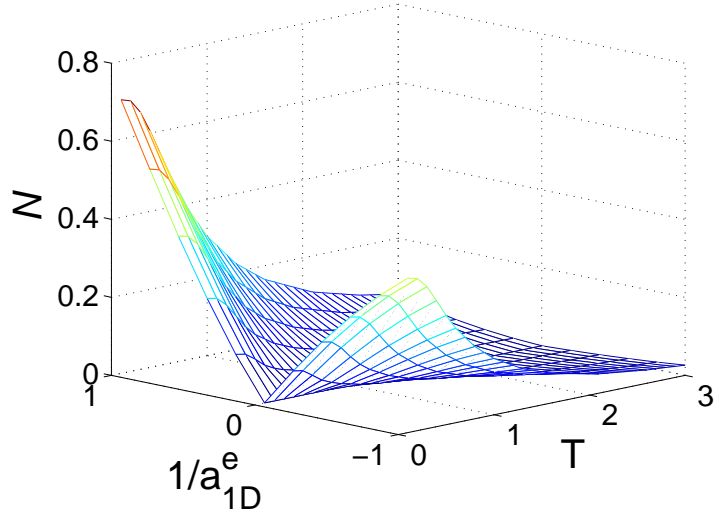
Figure 4.6: Negativity $\mathbb{N}$ as function of T and $1/a_{1D}^e$ for two bosonic atoms.

For $1/a_{1D}^e = 0$, the corresponding interaction strength $g_{1D}^e = 0$. The entanglement vanishes since there is no interaction between the two bosonic atoms. In this case, both atoms are in the lowest harmonic orbital.

For $1/a_{1D}^e \to -\infty$, the corresponding interaction strength g_{1D}^e approaches $+\infty$. There is very strong repulsion between the two bosonic atoms, the so-called impenetrable boson model. The total wave function asymptotically simplifies to

$$\Psi_{0\nu_e^0} = \sqrt{\frac{2}{\pi}} e^{-\frac{1}{2}X^2 - \frac{1}{2}x^2}|x|, \tag{4.31}$$

with the total energy $E_{0\nu_e^0} = 2$. The simplified wave function comes from the expansion of the confluent hypergeometric function $U(-\nu_e^0, 1/2; x^2)$ at $\nu_e^0 = 1/2$, which turns out to be $|x|$. In this limit, the two bosonic atoms are in the so-called "Tonks-Girardeau" regime [145, 146], where they behave similarly to two ideal (polarized) fermionic atoms. Their local properties, such as energy and density, are the same, but their non-local properties, such as momentum distribution and correlation, are generally quite different [132]. The "Tonks-Girardeau" regime has been realized in an optical lattice and the results of momentum distribution are in excellent agreement with a theory of fermionized trapped Bose gases [147]. For comparison, we show the reduced density matrix of Tonks bosons $\rho_B(x_1, x_1')$ and ideal fermions $\rho_F(x_1, x_1')$ in Figs. 4.8 and 4.9, respectively. We can see that the two matrices share the same diagonal elements, which are related to the local properties, while
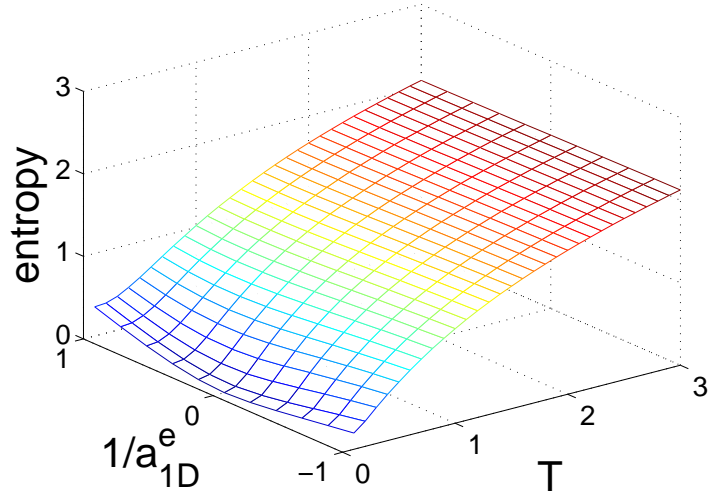
Figure 4.7: von Neumann entropy as function of T and $1/a_{1D}^e$ for two bosonic atoms.

the off-diagonal elements, which are related to correlation properties, are quite different. The Schmidt coefficients of ρ_B are calculated to be $\{0.7744, 0.1767, 0.041, \dots \}$, with an entanglement of about 0.683, which is slightly smaller than $\ln 2$ ($\simeq 0.693$), the entanglement of two ideal fermionic atoms in the same trap.
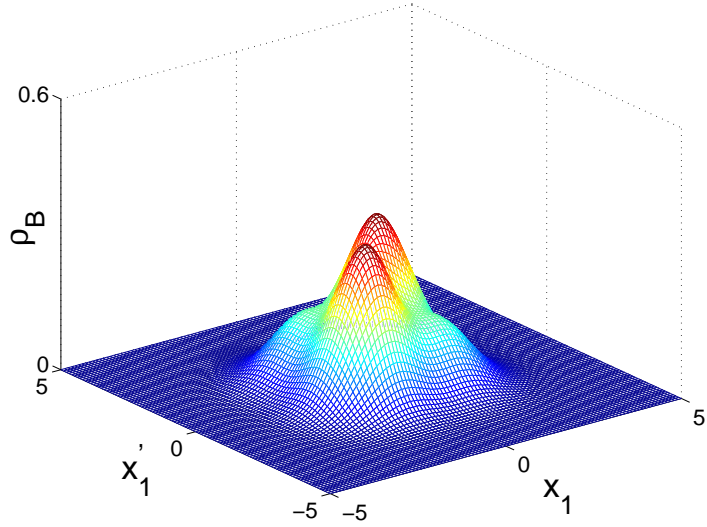
Figure 4.8: The reduced density matrix $\rho_B(x_1, x_1')$ of two bosonic atoms in the "Tonks-Girardeau" regime.

For $1/a_{1D}^e \to +\infty$, the corresponding interaction strength g_{1D}^e approaches $-\infty$, and there is very strong attraction between the two bosonic atoms. We identify this limit as the

51
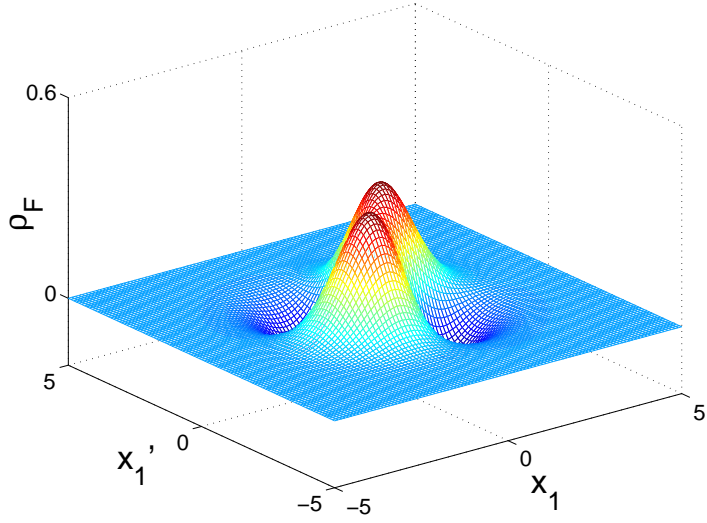
Figure 4.9: The reduced density matrix $\rho_F(x_1, x_1')$ for two ideal fermionic atoms.

bound state regime because the wave function takes the asymptotic form

$$\Psi_{0\nu_e^0}(X, x) = \left(\frac{2}{\pi(a_{1D}^e)^2}\right)^{1/4} e^{-\frac{X^2}{2}} e^{-\frac{\sqrt{2}|x|}{a_{1D}^e}}, \tag{4.32}$$

with a total energy $E_{0\nu_e^0} \simeq -1/(a_{1D}^e)^2$, which is the typical form for a bound state. a_{1D}^e is proportional to the size of the bound state. As $1/a_{1D}^e$ increases, the entanglement increases and asymptotically approaches $\propto \ln(1/a_{1D}^e)$.

One way to obtain the wave function is to use the expansion of the confluent hypergeometric function for $\nu_e^0 \to -\infty$. By matching the expansion coefficients, we can obtain the asymptotic wave function. Another more instructive method is to solve the relative motion directly

$$-\frac{1}{2}\frac{d^2}{dx^2}\psi + \frac{1}{2}x^2\psi - \frac{\sqrt{2}}{a_{1D}^e}\delta(x)\psi(x) = E\psi(x). \tag{4.33}$$

For deep bound state solutions, the effect of the external trap can be ignored since the size of the bounded pair approaches 0. We then use a trial wave function $\psi = \sqrt{\kappa}e^{-\kappa|x|}$, where κ is determined from the appropriate boundary condition. We obtain $E = -\kappa^2/2$ by inserting the trial function into the above equation for both $x < 0$ and $x > 0$. Then imposing of $\int_{0^-}^{0^+}$ on both sides leads to $\kappa = \sqrt{2}/a_{1D}^e$, the same form as in Eq. (4.32). Clearly, it is consistent

with the boundary condition at $x = 0$ [135], *i.e.*,

$$\left(\frac{1}{\psi(x)}\frac{d\psi(x)}{dx}\right)_{x\to 0^+} = -\frac{\sqrt{2}}{a^e_{1D}}. \tag{4.34}$$

4.4 Two identical fermionic atoms in a 1D harmonic trap

For two spin-polarized fermionic atoms, the Pauli principle excludes s-wave scattering. We consider p-wave scattering, which turns out to be non-trivial in this case. The interaction potential is given by [135]

$$V^F_{\text{int}}(x_{12}) = \frac{2\hbar^2 a^o_{1D}}{m}\frac{\overleftarrow{d}}{dx_{12}}\delta(x_{12})\frac{\overrightarrow{d}}{dx_{12}}. \tag{4.35}$$

The interaction strength is $g^o_{1D} = 2\hbar^2 a^o_{1D}/m$. Here the first derivative acts to the left and the second to the right, *i.e.*,

$$\int_{-\infty}^{+\infty}\phi^*(x)V_{\text{int}}(x)\chi(x)dx = \frac{2\hbar^2 a^o_{1D}}{m}\frac{d\phi(0)}{dx}\frac{d\chi(0)}{dx}, \tag{4.36}$$

with the short hand notation

$$\frac{d\phi(0)}{dx} = \left[\frac{d\phi(x)}{dx}\right]_{x=0}. \tag{4.37}$$

Using the same scaled unit, the dimensionless interaction potential is

$$V^F_{\text{int}} = \frac{a^o_{1D}}{\sqrt{2}}\frac{\overleftarrow{d}}{dx}\delta(x)\frac{\overrightarrow{d}}{dx}. \tag{4.38}$$

The CM motion is still a harmonic oscillator. For the relative motion,

$$H_{\text{rel}} = -\frac{1}{2}\frac{d^2}{dx^2} + \frac{1}{2}x^2 + \frac{a^o_{1D}}{\sqrt{2}}\frac{\overleftarrow{d}}{dx}\delta(x)\frac{\overrightarrow{d}}{dx}, \tag{4.39}$$

the eigenfunction is again solved in Ref. [135]

$$\psi_{\nu_o}(x) = \frac{A_o}{\sqrt{\pi}}xe^{-\frac{x^2}{2}}\Gamma\left(-\nu_o\right)U\left(-\nu_o,\frac{3}{2};x^2\right), \tag{4.40}$$

with the relative energy $E_o = 2\nu_o + 3/2$. E_o and the effective scattering length a^o_{1D} are constrained by the following quantization condition

$$\frac{\Gamma(-\frac{E_o}{2} + \frac{3}{4})}{\Gamma(-\frac{E_o}{2} + \frac{1}{4})} = \frac{1}{\sqrt{2}a^o_{1D}}, \tag{4.41}$$

the same form as in Eq. (4.15). The normalization constant A_o is given by

$$A_o = \left(\frac{\Gamma\left(-\nu_o - \frac{1}{2}\right)}{\Gamma\left(-\nu_o\right)} \frac{1}{\mathcal{F}(-\nu_o) - \mathcal{F}(-\nu_o - \frac{1}{2})} \right)^{\frac{1}{2}}. \tag{4.42}$$

In Fig. 4.10, we show the relative energy spectrum of two spin-polarized fermionic atoms under p-wave scattering. The overall shape of the spectrum is similar to that for a 3D s-wave scattering [41], as both have the velocity dependent scattering potential associated with d/dx or $\partial/\partial r$. Different from a 1D s-wave scattering, we find that the eigenenergy is an increasing function of a_{1D}^o, which can be easily seen from the quantization condition Eq. (4.41) (cf. Eq. (4.15)). We note that a single bound state exists for any scattering length, irrespective of its sign. Here the threshold energy for the bound state is $3/2$, which is the lowest energy for two ideal fermionic atoms in the same trap. For $a_{1D}^o < 0$, the appearance of such a bound state is purely due to the confinement, since no bound state can be formed in free space for $a_{1D}^o < 0$.
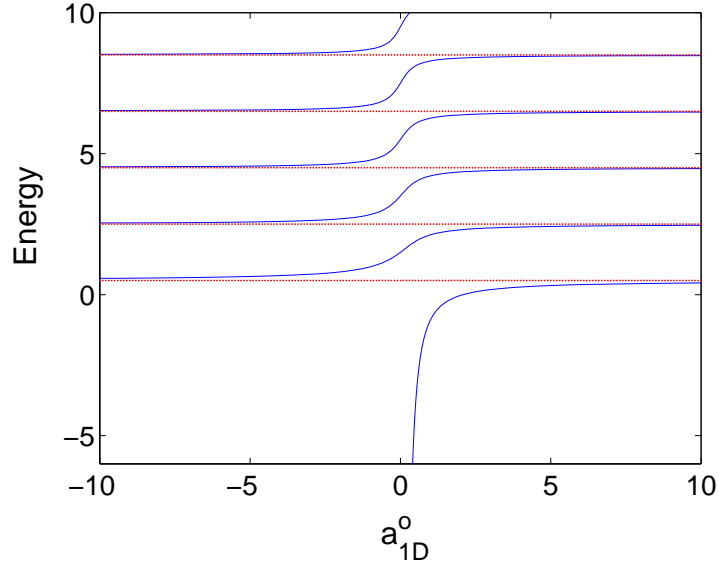
Figure 4.10: The spectrum as function of the effective scattering length a_{1D}^o for two spin-polarized fermionic atoms. The solid lines are for odd-parity modes, and the dotted lines are for unperturbed even-parity modes.

The wave functions of the two lowest eigenstates for the relative motion are shown in Figs. 4.11 and 4.12, for $a_{1D}^o = 1$ and $a_{1D}^o = -1$, respectively. We note that the discontinuity in the wave function at $x = 0$ is due to the presence of the interaction term. However, the

derivative is continuous in this case.
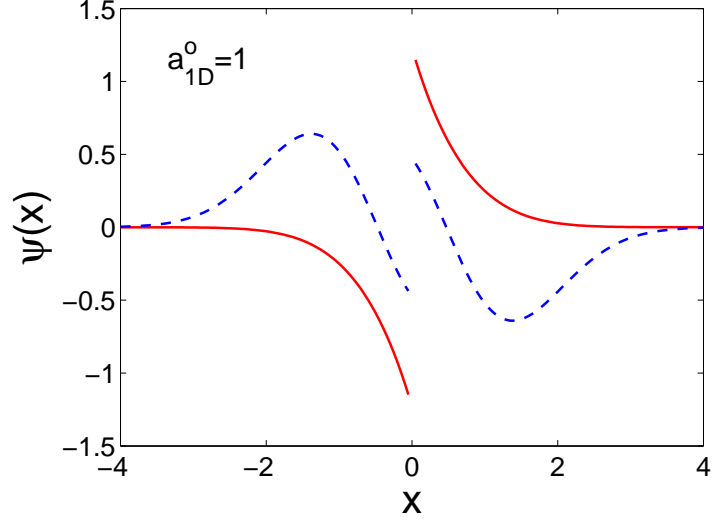
Figure 4.11: Wave functions of the two lowest eigenstates for $a^o_{1D} = 1$ with odd parity. The solid line is for ground state, and the dashed line is for the first excited state with odd parity.

The total eigenfunction including both the CM and relative motion is

$$\Psi_{n\nu_o} = \phi_n\left(\frac{x_1 + x_2}{\sqrt{2}}\right)\psi_{\nu_o}\left(\frac{x_1 - x_2}{\sqrt{2}}\right), \tag{4.43}$$

with a total energy $E_{n\nu_o} = n + 2\nu_o + 2$.

4.4.1 Entanglement in the ground state

At $T = 0$, the ground state wave function is

$$\Psi_{0\nu_o^0}(x_1, x_2) = \phi_0\left(\frac{x_1 + x_2}{\sqrt{2}}\right)\psi_{\nu_o^0}\left(\frac{x_1 - x_2}{\sqrt{2}}\right), \tag{4.44}$$

where ν_o^0 is the minimal value that satisfies Eq. (4.41). In the single particle basis

$$\Psi_{0\nu_o^0}(x_1, x_2) = \sum_{pq}\beta_{pq}\phi_p(x_1)\phi_q(x_2), \tag{4.45}$$

with β_{pq} given by

$$\beta_{pq} = \frac{-2}{\pi^{3/4}}\left(\frac{\Gamma(-\nu_o^0 - \frac{1}{2})}{\Gamma(-\nu_o^0)}\frac{1}{\mathcal{F}(-\nu_o^0) - \mathcal{F}(-\nu_o^0 - \frac{1}{2})}\right)^{\frac{1}{2}}\frac{1 - (-1)^{p+q}}{2}\frac{(-1)^{\frac{p-q-1}{2}}\Gamma(\frac{p+q+2}{2})}{(2\nu_o^0 + 1 - p - q)\sqrt{p!q!}} \tag{4.46}$$
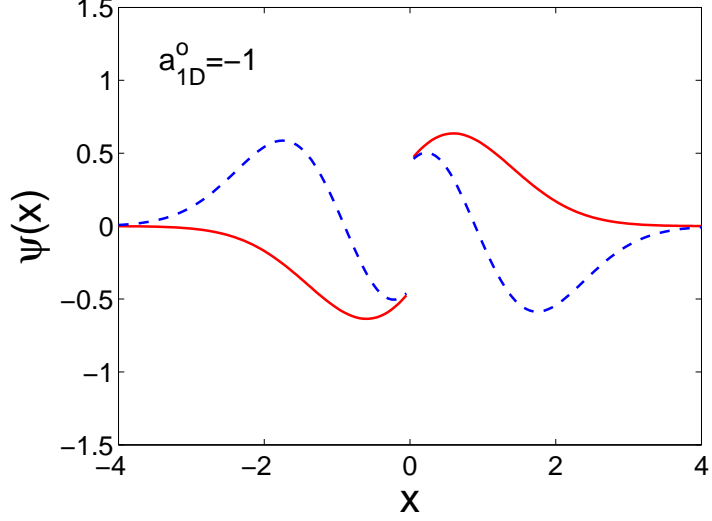
Figure 4.12: The same as in Fig. 4.11 except for $a^o_{1D} = -1$.

which is similar to the expansion in the s-wave scattering. For identical fermions, we can also write the wave function in the following form

$$|\phi_0\psi_{\nu^0_e}\rangle = \frac{1}{\sqrt{2}}\sum_{pq}\beta_{pq}|pq\rangle, \tag{4.47}$$

here

$$|pq\rangle = \begin{cases} (|p_1q_2\rangle - |q_1p_2\rangle)/\sqrt{2} & (p \neq q), \\ 0 & (p = q). \end{cases} \tag{4.48}$$

The two-atom density matrix is $\rho_F = |\phi_0\psi_{\nu^0_e}\rangle\langle\phi_0\psi_{\nu^0_e}|$. Because the two fermionic atoms are identical particles, there is only one single-particle density matrix ρ^f, normalized to one, which is computed to be $\rho^f = (\beta^\dagger\beta)^T$ [19].

We calculate the von Neumann entropy using the same technique as in the s-wave scattering. The numerical results are shown in Fig. 4.13. We note that there are three features different from the bosonic case. First, the von Neumann entropy is discontinuous with respect to the coupling strength. Second, the entropy is always larger than $\ln(2)$ in the whole range of the coupling strength. Third, the entropy does not monotonically increase as $|a^o_{1D}|$ increases.
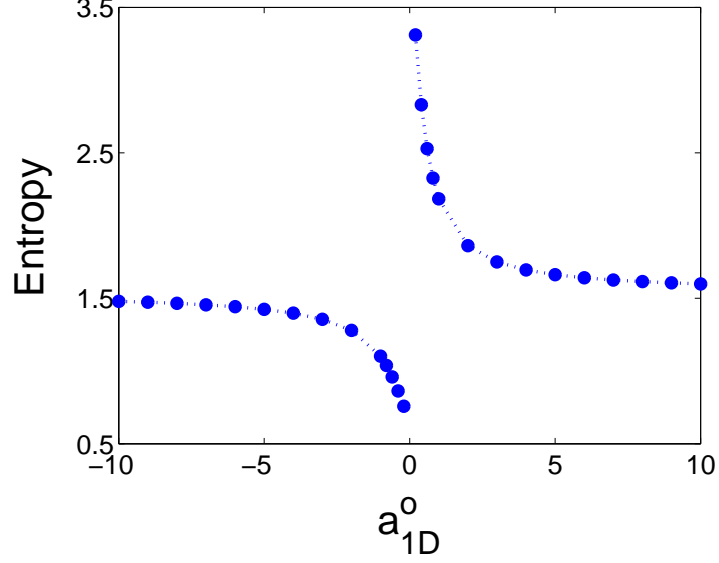
Figure 4.13: Von Neumann entropy as function of the effective scattering length a^o_{1D} for two spin-polarized fermionic atoms. At $a^o_{1D} \to \pm\infty$, the entanglement saturates to about 1.520.

4.4.2 Entanglement at finite temperatures

In this case, the density matrix is

$$
\begin{aligned}
\rho_o(T) &= \sum_{n\nu_o} P_{n\nu_o}(T) |\Psi_{n\nu_o}\rangle\langle\Psi_{n\nu_o}| \\
&= \sum_{pq;p'q'} \left(\sum_{n\nu_o} P_{n\nu_o}(T) \beta^{(n\nu_o)}_{pq} \left(\beta^{(n\nu_o)}_{p'q'} \right)^* \right) |p_1 q_2\rangle\langle p'_1 q'_2|,
\end{aligned}
\tag{4.49}
$$

here ν_o only includes odd parity. The thermal distribution $P_{n\nu_o}$ is given by

$$
P_{n\nu_o}(T) = \frac{e^{-(n+\nu_o)/T}}{\sum_{n\nu_o} e^{-(n+\nu_o)/T}}.
\tag{4.50}
$$

Following the same technique as in the bosonic case, we calculate negativity of two spin-polarized fermionic atoms. The numerical results are shown in Fig. 4.14. Clearly, negativity is not continuous at vanishing coupling strength for any temperature we considered, and there is no "sudden death" either [143, 144]. We also find that negativity decreases as the temperature increases. This again agrees with our intuitive understanding.

4.4.3 Some limiting cases of ground state entanglement

We will discuss some limiting cases in this section: $a^o_{1D} \to \pm\infty$, $a^o_{1D} \to 0^+$, and $a^o_{1D} \to 0^-$.
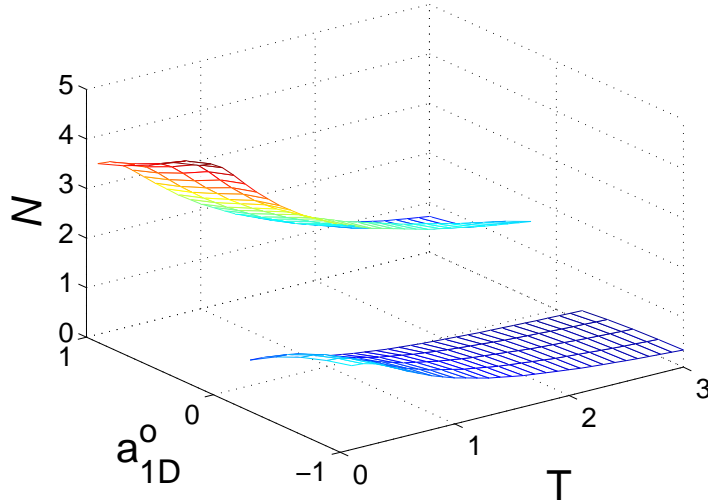
Figure 4.14: Negativity as function of T and the effective scattering length a_{1D}^o for two spin-polarized fermionic atoms.

For $a_{1D}^o \to \pm\infty$, the interaction strength g_{1D}^F approaches $\pm\infty$. There is a very strong interaction (repulsion or attraction) between the two fermionic atoms. The total wave function in both cases simplifies to

$$\Psi_{0\nu_o} = \frac{1}{\sqrt{\pi}} e^{-\frac{1}{2}X^2 - \frac{1}{2}x^2} \mathrm{sgn}(x), \tag{4.51}$$

with the eigenenergy $E_{0\nu_o} = 1$. Here $\mathrm{sgn}(x) = x/|x|$. The wave function comes from the expansion of $xU(-\nu_o, 3/2; x^2)$ at $\nu_o = -1/2$, which turns out to be $\mathrm{sgn}(x)$. Analogously, the two fermionic atoms are in the so-called "fermionic Tonks-Girardeau" regime [148, 149], where they behave similarly to two ideal bosonic atoms. Different from the bosonic case, the two bosonic atoms are in a bound state when the interaction strength approaches $-\infty$. We find that the behavior of the two fermionic atoms does not fall into the bound state regime for the same interaction strength. The entanglement of the two fermionic atoms saturates to about 1.520, while there does not exist any entanglement for the ground state of two ideal bosonic atoms in the same trap. This remarkable difference is due to the different symmetry properties under permutation between bosonic and fermionic atoms.

For $a_{1D}^o \to 0^+$, the interaction strength g_{1D}^F approaches 0^+. There is very weak repulsion between the two fermionic atoms. We identify this limit as the bound state regime because

the wave function takes the asymptotic form

$$\Psi_{0\nu_o^0}(X,x) = \left(\frac{2}{\pi(a_{1D}^o)^2}\right)^{1/4} e^{-\frac{X^2}{2}} e^{\frac{-\sqrt{2}|x|}{a_{1D}^o}} \operatorname{sgn}(x). \tag{4.52}$$

The corresponding energy takes the asymptotic value $E_{0\nu_o^0} \simeq -1/(a_{1D}^o)^2$, which is the typical binding energy for a bound state. As the size of the bound state ($\propto a_{1D}^o$) becomes smaller, the entanglement increases asymptotically approaches $\propto \ln(1/a_{1D}^o)$. The wave function can be obtained by a similar method as in the bosonic case, with the trial wave function $\psi = \sqrt{\kappa}\operatorname{sgn}(x)e^{-\kappa|x|}$, reflecting the symmetry requirement. Starting from Eq. (4.39), we multiply from the left by $f(x) = 1$ and then impose $\int_0^{+\infty}$ on both sides. Thus, we obtain $E = -\frac{1}{2}\kappa^2$. κ can be determined by noticing that $\psi'(x) = -\kappa\operatorname{sgn}(x)\psi(x) + 2\psi(0^+)\delta(x)$ due to the discontinuity in the wave function. A little algebra shows that $\kappa = \sqrt{2}/a_{1D}^o$, which is consistent with the boundary condition at $x = 0$, *i.e.*,

$$\left(\frac{1}{\psi(x)}\frac{d\psi(x)}{dx}\right)_{x\to 0^+} = -\frac{\sqrt{2}}{a_{1D}^o}. \tag{4.53}$$

For $a_{1D}^o \to 0^-$, the interaction strength g_{1D}^F approaches 0^-, which means that there is very weak attraction between the two fermionic atoms. We identify this limit as the ideal fermion regime because the wave function is

$$\begin{aligned}
\Psi_{0\nu_o^0}(X,x) &= \sqrt{\frac{2}{\pi}}xe^{-\frac{X^2}{2}-\frac{x^2}{2}} \\
&= \frac{1}{\sqrt{2}}[\phi_1(x_1)\phi_0(x_2) - \phi_0(x_1)\phi_1(x_2)]. \tag{4.54}
\end{aligned}$$

The Schmidt coefficients are $\lambda_0 = \lambda_1 = 1/2$, so the entropy is $\ln(2)$. This value is purely due to the antisymmetry property, and it does not reflect any useful quantum correlations between the two fermionic atoms [19].

The counterintuitive features of $a_{1D}^o \to 0^\pm$ originate from the d/dx differentiation, which makes V_{int}^F similar to a 3D regularized pseudopotential. For $a_{1D}^o > 0$, V_{int}^F behaves like an attractive interaction as far as the bound-state properties are concerned, while it scatters like a repulsive potential. For $a_{1D}^o < 0$, matters are reversed—there is no bound state, but V_{int}^F scatters as if an attractive interaction were at work. The limit $a_{1D}^o \to 0^+$ exhibits an anomaly: the binding energy grows without bound and the scattering cross section vanishes [41].

4.5 A duality between bosons and fermions

The physics of 1D Bose systems differ from ordinary 3D quantum gases in many aspects. For example, by decreasing the particle density n, a typical 3D quantum many-body system becomes more ideal, whereas in a 1D Bose gas the role of interactions becomes more important [147]. The reason is that in a 3D system, the kinetic energy per particle at the mean interparticle separation is $K_{3D} \sim n^{2/3}$ and the interaction energy per particle is $I_{3D} \sim n$. The ratio of the interaction to kinetic energy, $\gamma_{3D} = I_{3D}/K_{3D}$, characterizing the different physical regimes of a 3D quantum gas, approaches 0 as n decreases to 0, *i.e.*, an ideal gas. On the other hand, for a 1D system, the kinetic energy per particle at the mean interparticle separation is $K_{1D} \sim n^2$ and the interaction energy per particle is still $I_{1D} \sim n$, so $\gamma_{1D} = I_{1D}/K_{1D}$ approaches infinity as n decreases to 0. Here the dimensionality plays an important role. For a large value of γ_{1D}, the gas enters the "Tonks-Girardeau" (TG) regime [146]. It was shown that the many-body problem of hard-sphere bosons in 1D can be mapped exactly onto that of an ideal Fermi gas, so that many properties of such Bose systems are Fermi-like [146]. This fact is now known as "Fermi-Bose duality". It is not restricted to the hard-sphere model, and relates strongly interacting bosons to weakly interacting fermions and vice versa. The duality has been discussed in Ref. [135]. Their results confirm the perfect mapping between bosons and fermions if the condition $g_{1D}^B g_{1D}^F = -1$ is satisfied (coupling strengths have been appropriately scaled). Here we can recover the duality in this special two-atom case. Following the above mapping condition, it turns out that the scattering lengths need to satisfy $a_{1D}^e = a_{1D}^o$. Under this condition, the energy spectrums for the bosonic and fermionic cases are the same, which leads to $\nu^e - \nu^o = 1/2$ for each corresponding level. On the other hand, the eigenfunctions of two bosonic atoms and two fermionic atoms are

$$
\begin{aligned}
\Psi^B(x_1, x_2) &\propto \phi_n(X) e^{-\frac{x^2}{2}} U\left(-\nu^e, \frac{1}{2}; x^2\right), \\
\Psi^F(x_1, x_2) &\propto \phi_n(X) x e^{-\frac{x^2}{2}} U\left(-\nu^o, \frac{3}{2}; x^2\right),
\end{aligned}
\tag{4.55}
$$

respectively. By using Kummer transformation $U(a, c; x) = x^{1-c}U(a-c+1, 2-c; x)$ [139], we can rewrite the latter as

$$\Psi^F(x_1, x_2) \quad \propto \quad \phi_n(X)\text{sgn}(x)e^{-\frac{x^2}{2}}U\left(-\nu^o - \frac{1}{2}, \frac{1}{2}; x^2\right). \tag{4.56}$$

If $\nu_e = \nu_o + 1/2$, we obtain

$$\Psi^F(x_1, x_2) = \text{sgn}(x_1 - x_2)\Psi^B(x_1, x_2). \tag{4.57}$$

It means that the wave function of two fermionic (bosonic) atoms can be obtained by anti-symmetrizing (symmetrizing) the corresponding wave function of two bosonic (fermionic) atoms. The sign change in the wave function does not affect local properties. However, it does affect non-local properties, such as correlation, which we have emphasized before.

4.6   A T-matrix approach for finding the spectrum

The spectrum can also be obtained with the help of a T-matrix approach, where the eigenenergies are just the simple poles. The detailed discussion for the 3D case has been carried out in Ref. [150]. The idea is to find the T-matrix for a reference Hamiltonian, which is usually easier to solve, and then use the Lupu-Sax theorem to obtain the desired T-matrix [151]. Here we follow the same procedure and limit our discussion to a 1D system.

First we set the background Hamiltonian which is free from the external trap potential,

$$H' = -\frac{\hbar^2}{2m}\frac{d^2}{dx^2} + E. \tag{4.58}$$

The energy independent Green function is

$$\langle x|G_{H'}|x'\rangle = \frac{m}{\hbar^2}|x - x'|, \tag{4.59}$$

which can be easily verified from the definition $(E - H')G_{H'} = I$ (I is the identity operator). In the presence of a point scatter $V(x) = g\delta(x), g = -\sqrt{2}\hbar^2/(ma_0)$. The T-matrix in the long wave length limit is found to be

$$\langle x|T_{H',V}|x'\rangle = g\delta(x)\delta(x'). \tag{4.60}$$

If we add a harmonic trap $U(x) = \frac{1}{2}m\omega^2 x^2$, the new Hamiltonian is

$$H = -\frac{\hbar^2}{2m}\frac{d^2}{dx^2} + \frac{1}{2}m\omega^2 x^2. \tag{4.61}$$

In this case, the Green function is

$$\langle x|G_H(E)|x'\rangle = \sum_{n=0}^{\infty} \frac{\phi_n(x)\phi_n^*(x')}{E - (n + \frac{1}{2})\hbar\omega}, \tag{4.62}$$

where $\phi_n(x)$ are the eigenfunctions of H. We can use the Lupu-Sax theorem [151], which relates the T-matrix of the scatter V in the background Hamiltonian H to the T-matrix for the same scatter in a different background Hamiltonian H'. To be explicit, we have the following identity

$$T_{H,V}(E) = [1 - T_{H',V}(E)[G_H(E) - G_{H'}(E)]]^{-1} T_{H',V}(E). \tag{4.63}$$

With the help of the above identity, we obtain

$$T_{H,V} = \frac{g|0\rangle\langle 0|}{1 - g\langle 0|G_H - G_{H'}|0\rangle}, \tag{4.64}$$

with

$$\begin{aligned}
&\langle 0|G_H - G_{H'}|0\rangle \\
&= \sum_{n=0}^{\infty} \frac{|\phi_n(0)|^2}{E - (n + \frac{1}{2})\hbar\omega} \\
&= -\frac{1}{a_{ho}2\hbar\omega} \frac{\Gamma(-\frac{E}{2\hbar\omega} + \frac{1}{4})}{\Gamma(-\frac{E}{2\hbar\omega} + \frac{3}{4})},
\end{aligned} \tag{4.65}$$

where $a_{ho} = \sqrt{\hbar/(m\omega)}$ is the trap width. This result is exactly the same as the energy quantization condition in Eq. (4.15). However, for fermionic case, we met difficulties due to the double derivatives.

4.7 Conclusion

In conclusion, we have systematically studied the quantum entanglement properties of two interacting spin-polarized atoms in a 1D harmonic trap. At very low temperature, the interaction potential is modelled by the well-known contact potential. We then discuss the eigen-spectrum for bosonic and fermionic atom pair, respectively. The ground state entanglement is measured by von Neumann entropy. The different amount of entanglement between bosonic and fermionic pairs can be traced partially to different symmetries of their wave functions. In most cases, the ground state entanglement of two atoms is

found to increase with interaction strength. However for two fermionic atoms with repulsive interactions, the ground state entanglement decreases with the increase of interaction strength. For the temperature dependence, we use negativity as the mixed state entanglement measure. We find that with increasing temperature, entanglement between two atoms decreases, which means temperature acts as noise to deteriorate the entanglement. As a general rule, we conclude that the nature of atom-atom interaction, being attractive or repulsive, also influences the quantum entanglement properties. Furthermore, we briefly discuss the "Fermi-Bose mapping" in a 1D system. We find that the results of the model potential are consistent with this mapping condition. Finally, as an alternative method, we show how to obtain the eigen-spectrum by using the T-matrix approach.

CHAPTER V

ENTANGLEMENT BETWEEN TWO FERMIONIC ATOMS INSIDE A CYLINDRICAL HARMONIC TRAP

5.1 Introduction

In this chapter, we will study the entanglement of two fermionic atoms in a cylindrical harmonic trap across Feshbach resonance. This is motivated by the recent experiments at ETH [56, 57]. The experiments began with two fermionic atoms in a single lattice site in the MI phase due to the negligible tunnelling. The experiment showed that two initially non-interacting fermionic atoms will acquire orbital deformation and entanglement during the BCS-BEC crossover. During the whole process, the two fermionic atoms remain in different internal states, so the two fermionic atoms actually interact via the s-wave scattering which is different from that for two polarized fermionic atoms. Because of this, the results can also be applied to two identical bosonic atoms in the same trap. The spectrum of s-wave scattering has been studied in Ref. [41] for a spherical harmonic trap and in Ref. [42] for a general cylindrical harmonic trap. The pair entanglement of two bosonic atoms in a spherical harmonic trap has also been obtained in Ref. [59]. All of the above results are based on the single channel scattering model. We want to extend the earlier results [59] to general cylindrical symmetry and to also allow for the possibility that the two fermionic atoms may form a molecular bound state, albeit in the broad resonance regime. The entanglement dependence on the trap geometry and on the scattering strength in the complete range of the effective BCS to BEC crossover will be explored.

5.2 A model system

We begin with the successful model as proposed in Ref. [58], where two fermionic atoms are assumed to be located in the same lattice trap, which is approximated as a harmonic trap for the purpose of this thesis. Each optical lattice site represents an independent system,

since the quantum tunnelling, or hopping, is negligible for a deep optical lattice potential of interest here. The Hamiltonian for the two fermionic atoms is given by

$$H = \sum_{\mathbf{m}\sigma} E_{\mathbf{m}} a^{\dagger}_{\mathbf{m}\sigma} a_{\mathbf{m}\sigma} + \bar{\nu} b^{\dagger} b + \sum_{\mathbf{m},\mathbf{n}} \alpha_{\mathbf{m},\mathbf{n}} [a^{\dagger}_{\mathbf{m}\uparrow} a^{\dagger}_{\mathbf{n}\downarrow} b + \text{H.c.}], \quad (5.1)$$

where $E_{\mathbf{m}} = \sum_{j=x,y,z} \hbar\omega_j(m_j + 1/2)$ is the harmonic oscillator energy for the state labelled by $\mathbf{m} = (m_x, m_y, m_z)$ with angular frequencies $(\omega_x, \omega_y, \omega_z)$. $a^{\dagger}_{\mathbf{m}\sigma}$ is the creation operator for a fermionic atom in the open channel with energy $E_{\mathbf{m}}$ and spin σ. $b^{\dagger}$ is the creation operator for a two-atom bound state, a bosonic molecule in the two fermionic closed channel with its center of mass wave function fixed exactly at the ground state of the trap, a result of the simple approximation that the optical lattice trap potential for the bound state molecule is the sum of the trap potentials on the two atoms. $\bar{\nu}$ is the energy difference between the closed-channel bosonic molecule and the two fermionic atoms in the open channel. $\alpha_{\mathbf{m},\mathbf{n}}$ is the coherent coupling element converting two open channel fermionic atoms into a closed channel bosonic molecule, which is defined to contain a common constant pre-factor α. The relative motional part of the molecular ground state will be approximated as a contact $\delta(\vec{r})$ function, since it is typically of atomic size [58, 152], much less than other length scales in the problem. Such a simplification contains an ultra-violet divergence that can be removed by a suitable momentum cutoff with a renormalized detuning. An alternative formulation involves the use of a regularized delta function [153]. The cylindrical harmonic trap is characterized by the trap frequencies $\omega_x = \omega_y = \omega_{\perp} = \omega_z/\lambda$ with λ parameterizing the trap aspect ratio. Within this model, the two fermionic atoms in the open channel (being atoms) at a band $\mathbf{m}$ and $\mathbf{n}$ can be converted into a closed channel bosonic molecule, or vice versa. The eigenstate is

$$|\Psi\rangle = (\beta b^{\dagger} + \sum_{\mathbf{m},\mathbf{n}} \eta_{\mathbf{m},\mathbf{n}} a^{\dagger}_{\mathbf{m}\uparrow} a^{\dagger}_{\mathbf{n}\downarrow})|\text{vac}\rangle. \quad (5.2)$$

These coefficients are determined by the following coupled equations

$$\eta_{\mathbf{m,n}} = \beta \frac{\alpha_{\mathbf{m,n}}}{E - E_{\mathbf{m,n}}}, \tag{5.3}$$

$$E - \bar{\nu} = \sum_{\mathbf{m,n}} \frac{\alpha_{\mathbf{m,n}}^2}{E - E_{\mathbf{m,n}}}, \tag{5.4}$$

$$\beta^{-2} = 1 + \sum_{\mathbf{m,n}} \frac{\alpha_{\mathbf{m,n}}^2}{(E - E_{\mathbf{m,n}})^2}. \tag{5.5}$$

As in Ref. [58], $\bar{\nu}$ is to be renormalized to ν^*. The parameters ν^* and α are matched to the experimentally relevant parameters a_s and r_0, where a_s is the s-wave scattering length between fermionic atoms in different internal states, and r_0 is the effective range. r_0 is defined in terms of the s-wave scattering phase shift δ by the equation

$$k\cot\delta = -\frac{1}{a_s} + \frac{1}{2}r_0 k^2 + O(k^4), \tag{5.6}$$

with k being the wave number for the relative motion. The so-called broad resonance typically corresponds to the regime of $|r_0| \ll d_\perp [\equiv \sqrt{\hbar/(m\omega_\perp)}]$. A dimensionless parameter $x = E/(2\hbar\omega_\perp) - 1 - \lambda/2$ is defined, with which the energy quantization condition becomes

$$\sqrt{2\lambda} \left[\frac{d_\perp}{a_s} + \frac{|r_0|}{d_\perp} \left(x + 1 + \frac{\lambda}{2} \right) \right] = -\frac{\lambda}{\sqrt{\pi}} F\left(-\frac{x}{\lambda}, \frac{1}{\lambda} \right), \tag{5.7}$$

where the function on the right hand side is defined in Ref. [42]

$$F(u, \eta) = \int_0^\infty dt \left(\frac{\eta e^{-ut}}{\sqrt{1 - e^{-t}}(1 - e^{-\eta t})} - \frac{1}{t^{3/2}} \right). \tag{5.8}$$

A spherical trap reduces to the well known result of $F(-x, 1) = -2\sqrt{\pi}\,\Gamma(-x)/\Gamma(-x - 1/2)$ [41]. Furthermore, if $r_0 \equiv 0$, the energy spectrum and eigenfunctions coincide with the results of two bosonic atoms in a harmonic trap as studied previously in Ref. [41, 42]. This is a straightforward conclusion, since for $r_0 = 0$ the current model describes the same physical process quantified by a single s-wave parameter a_s [41, 42]. A non-zero r_0 as incorporated in Ref. [58] allows for a more general model including both open channel fermionic atoms and a closed channel molecule.

The spectrum versus inverse scattering length $-d_\perp/a_s$ is shown in Fig. 5.1. As in previous studies [41, 42], the energy is still an increasing function of the inverse scattering

length $-d_\perp/a_s$. The state $|e\rangle$ corresponds to a deep bound state. The binding energy is computed to be $E_b = -\frac{\hbar^2}{ma_s^2}\left(1 + \frac{r_0}{a_s}\right)$ from Eq. (5.7), which is the same result obtained in Ref. [154]. We emphasize that the closed molecular channel is not the lowest two-atom (bound) state as shown in Fig. 5.1.
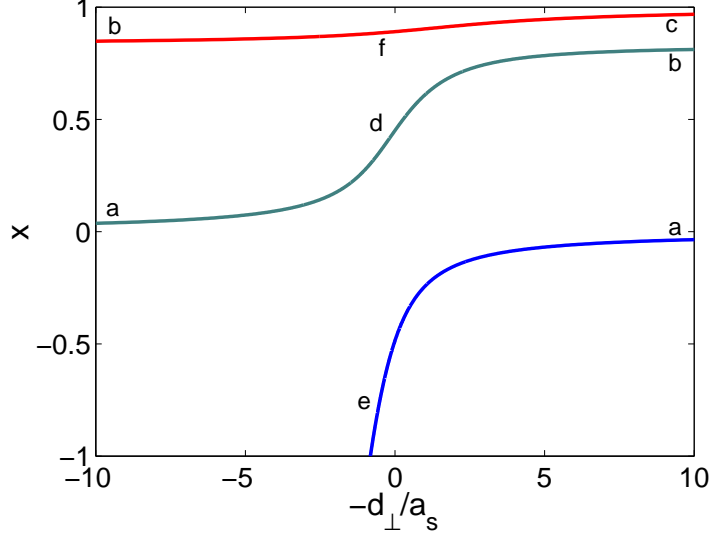
Figure 5.1: Energy spectrum of two fermionic atoms in a harmonic trap versus inverse scattering length in the broad resonance regime. Here we choose $\lambda = 5/6$ and $|r_0|/d_\perp = 0.04$.

The inclusion of the effective range allows us to introduce an effective scattering length as defined below,

$$\sqrt{2\lambda}\frac{d_\perp}{a_{\text{eff}}} = \sqrt{2\lambda}\left[\frac{d_\perp}{a_s} + \frac{|r_0|}{d_\perp}\left(x_0 + 1 + \frac{\lambda}{2}\right)\right],$$

$$\sqrt{2\lambda}\frac{d_\perp}{a_{\text{eff}}} = -\frac{\lambda}{\sqrt{\pi}}F\left(-\frac{x_0}{\lambda}, \frac{1}{\lambda}\right). \tag{5.9}$$

Further simplification gives the following result [155]

$$a_{\text{eff}} = \left(\frac{1}{a_s} - \frac{Er_0}{2d_\perp^2\,\hbar\omega_\perp}\right)^{-1}, \tag{5.10}$$

which is an energy-dependent scattering length.

In the following, we limit our discussion to the pair entanglement for the regime of broad resonance. Also, we focus on two adiabatic eigenstates labelled $|a\text{-}d\text{-}b\rangle$ and $|b\text{-}f\text{-}c\rangle$ in Fig. 5.1.

First, we briefly review the result on the molecular component according to Ref. [58].

Starting from a small positive scattering length, when adiabatically following the state $|$a-d-b$\rangle$, the molecular component P_{mol} ($\equiv \beta^2 \ll 1$) is small in the broad resonance regime [58, 156]. More precisely, it can be shown that

$$\beta^2 = \frac{|r_0|}{d_\perp} \frac{\partial x}{\partial \left(-\frac{d_\perp}{a_s}\right)}, \tag{5.11}$$

i.e., the molecular component is always small because of the small pre-factor $|r_0|/d_\perp$. An even smaller P_{mol} is expected along the state $|$b-f-c$\rangle$, which has a weaker dependence on the x-axis as shown in Fig. 5.1. Numerically we find the molecule probability remains less than 1% for $|r_0|/d_\perp = 0.04$.

5.3 Entanglement in the broad Feshbach resonance regime

In a spherical harmonic trap, the entanglement properties for $r_0 = 0$ have already been studied [59]. By making use of the model from Ref. [58], we can extend the earlier results to a multi-channel scattering model and also to a cylindrical harmonic trap. To begin with, we approximate the wave function of the two fermionic atoms (5.2) by neglecting the small molecular component, obtaining

$$|\Psi\rangle = \sum_{\mathbf{m},\mathbf{n}} \eta_{\mathbf{m},\mathbf{n}} a^\dagger_{\mathbf{m}\uparrow} a^\dagger_{\mathbf{n}\downarrow} |\text{vac}\rangle, \tag{5.12}$$

with the normalization constraint $\sum_{\mathbf{m},\mathbf{n}} |\eta_{\mathbf{m},\mathbf{n}}|^2 = 1$. $\eta_{\mathbf{m},\mathbf{n}}$ are assumed real and symmetric with $\eta_{\mathbf{m},\mathbf{n}} = \eta_{\mathbf{n},\mathbf{m}}$. In the single particle basis, the above becomes

$$|\Psi\rangle = \sum_{\mathbf{m},\mathbf{n}} \eta_{\mathbf{m},\mathbf{n}} |\mathbf{m}_1 \mathbf{n}_2\rangle \frac{|\uparrow_1\downarrow_2\rangle - |\downarrow_1\uparrow_2\rangle}{\sqrt{2}}. \tag{5.13}$$

Such a state has both spatial and spin degrees of freedom, but the two degrees of freedom remain factorized. We therefore adopt the von Neumann entropy as our entanglement measure for pure states. The factorized spin degree part simply contributes $\ln(2)$, and the total entropy becomes $\mathbb{E} = \mathbb{E}_{\text{spatial}} + \ln(2)$ [18]. While non-trivial, the spatial part of entanglement $\mathbb{E}_{\text{spatial}}$ can be computed from the Schmidt decomposition of the spatial wave function, *i.e.*, we need to find

$$\sum_{\mathbf{m},\mathbf{n}} \eta_{\mathbf{m},\mathbf{n}} |\mathbf{m}\rangle_1 |\mathbf{n}\rangle_2 = \sum_{\mathbf{m}} \kappa_{\mathbf{m}} |\phi_{\mathbf{m}}\rangle_1 |\psi_{\mathbf{m}}\rangle_2, \tag{5.14}$$

with the same $\phi_{\mathbf{m}} \equiv \psi_{\mathbf{m}}$, because $\eta_{\mathbf{m},\mathbf{n}}$ is symmetric. From this, the von Neumann entropy is found to be $\mathbb{E}_{\text{spatial}} = -\sum_{\mathbf{m}} \kappa_{\mathbf{m}}^2 \ln(\kappa_{\mathbf{m}}^2)$. Numerically finding the direct Schmidt decomposition for the 3D wave function turns out to be quite demanding. Fortunately, we can simplify this problem to an effectively 1D Schmidt decomposition, which is discussed in appendix B.

For the two adiabatic states $|\text{a-d-b}\rangle$ and $|\text{b-f-c}\rangle$, we have numerically evaluated their pair entanglement. First, we consider a nearly spherical trap of $\lambda \sim 1$. We take $\lambda = 5/6, 7/6$ and 1 in our numerical work with the results shown in Figs. 5.2 and 5.3. For both states, we find that pair entanglement first increases to some maximal value, then decreases and saturates to certain finite value. The overall dependence on the atom interaction strength remains essentially the same as before [59]. We can see that the maximal entanglement does not occur precisely at resonance for $|\text{a-d-b}\rangle$ and $|\text{b-f-c}\rangle$. It's the trap aspect ratio and effective range that determine the position of the maximal entanglement.
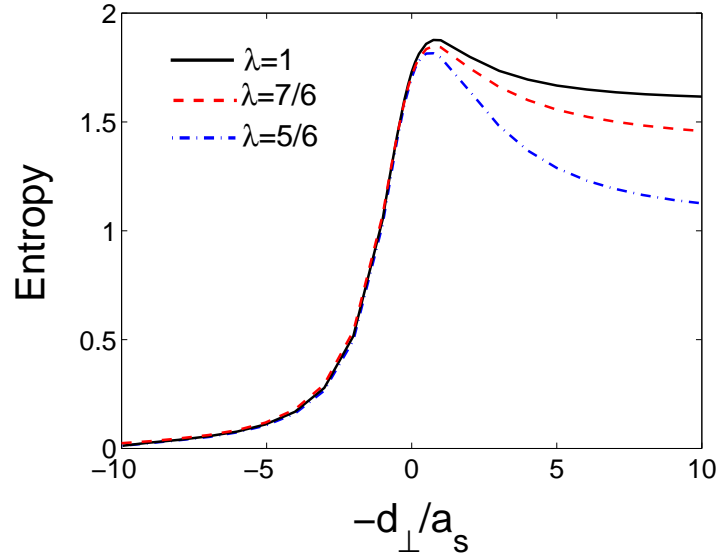
Figure 5.2: Pair entanglement versus the atomic interaction strength at different trap aspect ratio λ for state $|\text{a-d-b}\rangle$. Here $|r_0|/d_\perp = 0.04$ is assumed. The dependence on r_0 is very small within the broad resonance regime.

Next, we consider two extreme cases of $\lambda \ll 1$ and $\lambda \gg 1$, corresponding to the quasi-one- and quasi-two-dimensional limits, respectively [42]. The results of pair entanglement are shown in Figs. 5.4 and 5.5 for $\lambda = 1/20$ and $\lambda = 20$ respectively. We find that the
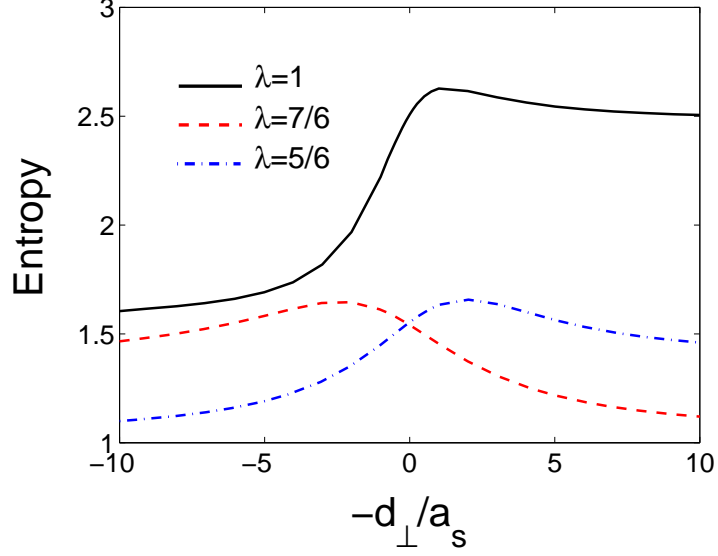
Figure 5.3: The same as in Fig. 5.2 except for state $|b$-f-$c\rangle$.

overall trend of the curves is still increasing at first and decreasing afterwards. The pair entanglement saturates to a lower value in the quasi-one-dimensional limit at $\lambda = 1/20$, again because of the reduced motional state degeneracy. The results can also be recovered by using an appropriately renormalized 1D (2D) scattering length a_{1D} (a_{2D}).

5.4   Some limiting cases for $\lambda \sim 1$

We now discuss some interesting cases for $-d_\perp/a_s \rightarrow \pm\infty$ in both processes $|a$-d-$b\rangle$ and $|b$-f-$c\rangle$. We ignore the discussions on $|d\rangle$ and $|f\rangle$ corresponding to states at resonance, because they are much more complicated and do not allow for a simple theoretical analysis here.

The adiabatic state $|a$-d-$b\rangle$ corresponds to $-d_\perp/a_s \rightarrow -\infty$ or $+\infty$ at $|a\rangle$ or $|b\rangle$, respectively. For $\lambda = 5/6$, we find

$$|b\rangle \propto \left[\sum_{n=1,2} (c^\dagger_{nz})^2 - 2c^\dagger_{1z}c^\dagger_{2z} \right] |000\rangle_1 |000\rangle_2, \tag{5.15}$$

whose spatial pair entanglement is $\ln(2\sqrt{2}) \approx 1.04$. Here we again follow the notation of Ref. [58] with $c^\dagger_{nj}$ the creation operator for a fermionic atom indexed by n in the j-th trap direction. State $|m_1 m_2 m_3\rangle_n$ therefore refers to atom n in the motional state m_j along the
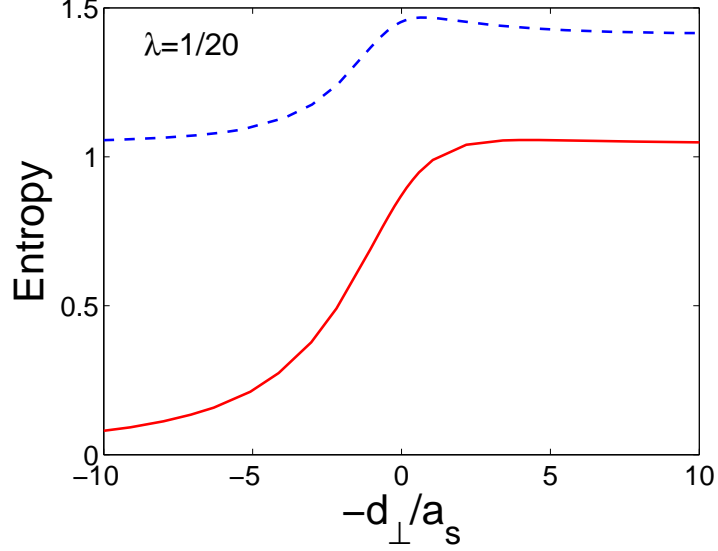
Figure 5.4: Entropy as function of the inverse scattering length for processes $|a\text{-}d\text{-}b\rangle$ and $|b\text{-}f\text{-}c\rangle$ at $\lambda = 1/20$. The solid line is for $|a\text{-}d\text{-}b\rangle$, and the dashed line is for $|b\text{-}f\text{-}c\rangle$.

j-th direction. For $\lambda = 7/6$, we find

$$|b\rangle \propto \left[\sum_{n=1,2;j=x,y} (c_{nj}^\dagger)^2 - 2 \sum_{j=x,y} c_{1j}^\dagger c_{2j}^\dagger \right] |000\rangle_1 |000\rangle_2 \qquad (5.16)$$

with a pair entanglement $\ln(4) \approx 1.39$. For $\lambda = 1$, we find

$$|b\rangle \propto \left[\sum_{n=1,2;j=x,y,z} (c_{nj}^\dagger)^2 - 2 \sum_{j=x,y,z} c_{1j}^\dagger c_{2j}^\dagger \right] |000\rangle_1 |000\rangle_2 \qquad (5.17)$$

with a pair entanglement $\ln(2\sqrt{6}) \approx 1.59$. We find that the pair entanglement is always larger at the limit of a spherical trap with $\lambda = 1$.

For the adiabatic state $|b\text{-}f\text{-}c\rangle$, we find generally that the pair entanglement at $\lambda = 1$ is well separated from $\lambda \neq 1$ because of the increased motional state degeneracy. State $|c\rangle$ corresponds to the limit of $-d_\perp/a_s \to +\infty$, which for $\lambda = 7/6$ becomes

$$|c\rangle \propto \left[\sum_{n=1,2} (c_{nz}^\dagger)^2 - 2 c_{1z}^\dagger c_{2z}^\dagger \right] |000\rangle_1 |000\rangle_2, \qquad (5.18)$$

which is precisely the state $|b\rangle$ for $\lambda = 5/6$ in the adiabatic state $|a\text{-}d\text{-}b\rangle$, whose pair entanglement therefore remains the same $\ln(2\sqrt{2}) \approx 1.04$. This correspondence persists also for $\lambda = 5/6$, where the state $|c\rangle$ is the same as state $|b\rangle$ for $\lambda = 7/6$ in the adiabatic

71
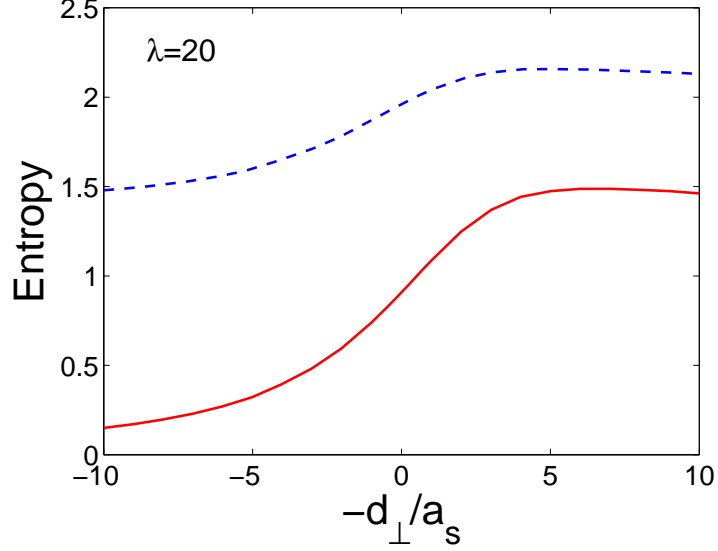
Figure 5.5: Entropy as function of inverse scattering length for processes $|a\text{-}d\text{-}b\rangle$ and $|b\text{-}f\text{-}c\rangle$ at $\lambda = 20$. The solid line is for $|a\text{-}d\text{-}b\rangle$, and the dashed line is for $|b\text{-}f\text{-}c\rangle$.

state $|a\text{-}d\text{-}b\rangle$. The state $|c\rangle$ at $\lambda = 1$ is expressible as a more complicated linear combination of different single particle states as

$$
|c\rangle \propto \left[-\sum_{n=1,2;j=x,y,z} (c_{nj}^{\dagger})^4 - \sum_{n,m;j\neq k} (c_{mj}^{\dagger})^2 (c_{nk}^{\dagger})^2 - 6\sum_{j}(c_{1j}^{\dagger})^2 (c_{2j}^{\dagger})^2 \right.
$$
$$
\left. +4\sum_{n\neq m;j} c_{mj}^{\dagger}(c_{nj}^{\dagger})^3 + 4\sum_{n;j\neq k} c_{1j}^{\dagger} c_{2j}^{\dagger}(c_{nk}^{\dagger})^2 - 8\sum_{j\neq k} c_{1j}^{\dagger} c_{1k}^{\dagger} c_{2j}^{\dagger} c_{2k}^{\dagger} \right] |000\rangle_1 |000\rangle_2, \quad (5.19)
$$

whose pair entanglement is $55\ln(2)/24 + 7\ln(3)/8 - \ln(5)/24 \approx 2.48$.

The reason that states $|b\rangle$ for $\lambda = 5/6$ and $|c\rangle$ for $\lambda = 7/6$ are the same is purely due to our choice of the trap aspect ratio $\lambda \sim 1$, so this conclusion does not hold in general. In our case, it can be easily understood as follows. As shown in the expression of $\alpha_{\mathbf{mn}}$, the parity of $\mathbf{m} - \mathbf{n}$ for each direction is conserved in the whole process, as is $\mathbf{m} + \mathbf{n}$. Thus, starting from $(\mathbf{m}, \mathbf{n}) = (\mathbf{0}, \mathbf{0})$, for both processes $|a\text{-}d\text{-}b\rangle$ and $|b\text{-}f\text{-}c\rangle$, $\mathbf{m} + \mathbf{n}$ is always even in each direction. So the excitation along any direction j must be a multiple of $2\hbar\omega_j$. This amount of excitation will be distributed between the two atoms. If $\lambda = 5/6$, the excitation along the z direction has lower energy, so the first excited state has the total excitation energy $2\hbar\omega_z$. The second excited state is along the transverse directions since $2\hbar\omega_\perp < 4\hbar\omega_z$. For $\lambda = 7/6$, we see the reverse situation, where the first excited state has excitation $2\hbar\omega_\perp$

along the transverse directions and the second excited state along the z direction. Clearly, this symmetry in states $|b\rangle$ and $|c\rangle$ is unambiguously based on the trap aspect ratio.

5.5 Generalization to a narrow resonance

We point out here that our current study cannot be generalized to the case of a narrow Feshbach resonance, where the bound-state molecular component in Eq. (5.2) cannot be simply neglected. To calculate the entanglement of the molecular component, we must know the details of its wave function. In our current study, the details of the molecular wave function are not important since its population is negligibly small. Actually, we do not even know the precise form of the molecular wave function in Ref. [58]. Recall that the spatial wave function is first approximated as being proportional to $\phi_0(\mathbf{R})\delta(\mathbf{r})$. This wave function cannot be normalized, and results in a divergence of the molecular energy. In Ref. [58], this divergence is removed by appropriate renormalization, which leaves the molecular wave function undetermined.

If we know the details of the molecular wave function, the pair entanglement inside the molecular component can be included by performing an analogous symmetric Schmidt decomposition Eq. (5.14) on Eq. (5.2). The total pair correlation can then be computed analogously in terms of the entropy of the independent Schmidt orbital expansion. Such calculations for a narrow resonance are subjected to future study.

5.6 Conclusion

In conclusion, we have studied the pair entanglement between two fermionic atoms inside a single optical lattice site approximated by a cylindrical harmonic trap. We thoroughly investigated the dependence of the pair entanglement on the atom-atom interaction strength and trap geometry along the complete BCS-BEC crossover in the broad resonance regime. We developed a formalism capable of studying the pair entanglement including the effect of an effective range r_0 at low energy. In the limit of a broad Feshbach resonance, where the effect of r_0 becomes negligibly small, our results reduce to the theory developed before for evaluating pair entanglement in a single open channel of two atoms without the presence of

a bound molecular state. We find that the pair entanglement changes significantly against atomic pair interaction because of the induced motional orbital deformations. In general, however, the exact value of the spatial pair entanglement is also governed by the motional state degeneracies, or the aspect ratio of the single optical lattice trap. As a rule of thumb, we find that spherically symmetric traps generally give rise to larger pair entanglement because of the enhanced level degeneracy due to a higher symmetry of the trap. We hope our study will provide new insights into the applications of quantum degenerate lattice systems to quantum information science.

CHAPTER VI

COHERENT SPIN MIXING OF TWO ATOMS IN A
SINGLE SITE OF AN OPTICAL LATTICE

6.1   Introduction

In the previous chapters, we have studied several archetypal examples of two-body entanglement involving atoms without significant internal degrees of freedom. This chapter will instead concentrate on the properties of internal degrees of freedom. This is motivated by recent successes of coherent spin mixing inside Bose condensed atoms both in the limit of a condensate with large number of atoms [60, 61], and the limit of many identical trapping sites, each containing two atoms [62, 63, 64]. These experiments have generated much interest in the quantum dynamics of atomic internal degrees of freedom [157, 158, 159], and raise significant hope for the long discussed applications of atomic quantum gases to the emerging field of quantum information science. The long spin coherence time observed rivals the best motional state coherence ever achieved in neutral atoms [160], and is ideally suited for quantum state processing applications, particularly when arranged with the periodically spaced identical copies as in an optical lattice [161].

In this chapter, we consider a system consisting of two ^{87}Rb atoms inside a cylindrical harmonic trap, which is an extension to the original experimental setup as in Ref. [62, 63]. We will focus on the development of a complete theory for two-atom spin mixing including a quantum treatment for their motional states, as well as the dipolar interaction. We first discuss several widely used approximation schemes for motional states in a spherical harmonic trap. As the dipolar effect is known to be very small in spherical traps, this case study turns out to be an excellent choice for calibrating the strength of the small spin exchange interaction. We find that the discrepancies spread over different approximation schemes by up to 10%, and the most accurate results constitute about a 20% error to the

experimental results. This surely calls for more precise theoretical estimates for the spin mixing process. We then consider the spin dipolar effect in a cylindrical harmonic trap. Our calculations show that for ^{87}Rb atom as the experiments concerned, the dipolar effect turns out to be very important in pancake traps with large $\lambda(\equiv \omega_z/\omega_\rho)$. This provides a feasible method for detecting such dipolar effects through coherent spin mixing dynamics in an optical lattice [162].

6.2 A model system

We focus on the system where spin mixing of two ^{87}Rb atoms was recently observed [62, 63]. A ^{87}Rb condensate is first loaded into an optical lattice with each site containing several atoms. The lattice potential is then increased to the Mott-insulator regime so that the tunnelling between neighboring sites is negligible. Sites with a single atom will not contribute to the spin mixing, and the sites with more than two atoms can be selectively emptied. We therefore restrict our study to the spin mixing dynamics in the sites containing only two atoms. Following the usual procedure of a harmonic approximation to the trap, we extend the trap geometry to a general cylindrical symmetry. Being bosonic with internal spin, the interactions between two ^{87}Rb atoms at low energy are dominated by the s-wave scattering and the spin dipolar interaction. For ^{87}Rb atom, the electronic spin is $s = 1/2$ and the nuclear spin is $i = 3/2$, so the hyperfine spin f can be either 1 or 2. As we know, for two colliding spin-f particles, the interaction strength is characterized by $2f$ independent scattering lengths a_F, where F is the total spin of the two particles. The particle symmetry, $i.e.$, bosons or fermions, further restricts F to take even or odd values between 0 and $2f$, respectively. In our case, F must take even values between 0 and $2f$ since ^{87}Rb is bosonic. We thus adopt the regularized pseudopotential as the scattering interaction with a_F characterizing the scattering in different channels. The dominant spin dipolar interaction is due to the intrinsic magnetic dipole moment of the atom, which is related to its total angular momentum by $\vec{\mu}_f = -\mathbf{g}_f\mu_B\vec{f}$, with μ_B being the Bohr magneton and $\mathbf{g}_f$ the Landé g-factor. For ^{87}Rb atom, $\mathbf{g}_f = [f(f+1) + s(s+1) - i(i+1)]/[f(f+1)]$. Both interactions depend on the hyperfine spin f, so we discuss spin mixing for $f = 1$ and

$f = 2$ separately.

Before we present the detailed analysis, we briefly comment on the two types of inter-action. We model the s-wave scattering with a contact potential, which is short range and isotropic. For dipolar interactions, it is long range and anisotropic. A crucial fact, as pointed out by Yi and You [163, 164], shows that the scattering length can also depend on the dipolar interaction. To properly account for the dipolar interaction, the "dipole-normalized" s-wave scattering length should be used instead of the "bare" s-wave scattering length [165]. For $f = 2$ ^{87}Rb atom, we estimate such correction is about 0.03% with respect to the bare scattering length, and is even smaller for $f = 1$. Both corrections are much less than other errors we will discuss. Thus, for our case, effects of the dipolar interaction on the scattering length can be completely neglected.

6.3 The $f = 1$ Zeeman manifold

The total spin F is 0 or 2 in this case. The total Hamiltonian can be written as $H = \sum_{i=1}^{2} H_0^{(i)} + H_s + H_{dd} + H_B$, with each term given by

$$
\begin{aligned}
H_0^{(i)} &= \left[-\frac{\hbar^2}{2m}\nabla_i^2 + \frac{1}{2}m\omega_\rho^2(\rho_i^2 + \lambda^2 z_i^2) \right], \\
H_s &= (g_0\mathcal{P}_0 + g_2\mathcal{P}_2)\delta^{(\mathrm{reg})}(\vec{r}_1 - \vec{r}_2), \\
H_{dd} &= \frac{c_d}{|\vec{r}_1 - \vec{r}_2|^3}\left[\vec{f}_1 \cdot \vec{f}_2 - 3(\vec{f}_1 \cdot \hat{r})\cdot(\vec{f}_2 \cdot \hat{r}) \right].
\end{aligned}
\tag{6.1}
$$

Here $H_0^{(i)}$ describes the non-interacting motion of atom i in a trap with aspect ratio λ. H_s is the elastic scattering interaction modelled by a contact potential. It has already been expressed in the form of different total spin F channels. H_{dd} is for the spin dipolar interaction. H_B accounts for the single-atom Zeeman effect. $\hat{r} \equiv (\vec{r}_1 - \vec{r}_2)/|\vec{r}_1 - \vec{r}_2|$ is the unit vector along the two atoms. $\delta^{(\mathrm{reg})}(\vec{r}) \equiv \delta(\vec{r})(\partial/\partial r)r$ is the regularized pseudopotential [41]. $\mathcal{P}_{0(2)}$ is the projector onto the total spin $F = 0(2)$ channel, which takes the form of $\mathcal{P}_0 = 1/4 - \vec{f}_1 \cdot \vec{f}_2$ and $\mathcal{P}_2 = 3/4 + \vec{f}_1 \cdot \vec{f}_2$. $g_F = 4\pi\hbar^2 a_F/m$ is the s-wave scattering strength, where $a_{0(2)}$ is the s-wave scattering length for the combined channel of total $F = 0(2)$. Both a_0 and a_2 are fixed as we are away from any Feshbach resonance. $c_d = \mu_0\mathbf{g}_1^2\mu_B^2/(4\pi)$ characterizes the strength of the dipolar interaction. The g-factor for $f = 1$ is calculated to

be $\mathbf{g}_1 = -1/2$.

We note that the interactions only depend on the relative coordinate and that the trap is harmonic, which again motivates us to work in the center of mass (CM) and the relative (rel) frame. The system Hamiltonian then becomes $H = H_{\mathrm{CM}} + H_{\mathrm{rel}}$ with

$$H_{\mathrm{CM}} \quad = \quad -\frac{\hbar^2}{2M}\nabla_{\vec{R}}^2 + \frac{1}{2}M\omega_\rho^2(\varrho^2 + \lambda^2 Z^2), \tag{6.2}$$

$$H_{\mathrm{rel}} \quad = \quad H_0 + H_s + H_{dd} + H_B, \tag{6.3}$$

for the CM- and rel-motion, respectively, with coordinates $\vec{R} = (\vec{r}_1 + \vec{r}_2)/2$ and $\vec{r} = \vec{r}_1 - \vec{r}_2$. $M = 2m$ is the total mass, while $\mu = m/2$ is the reduced mass. $\vec{\varrho}$ and Z ($\vec{\rho}$ and z) are the transversal and longitudinal component of $\vec{R}$ ($\vec{r}$) respectively. H_{rel} contains several parts as outlined below,

$$H_0 \quad = \quad -\frac{\hbar^2}{2\mu}\nabla_{\vec{r}}^2 + \frac{1}{2}\mu\omega_\rho^2(\rho^2 + \lambda^2 z^2),$$

$$H_s \quad = \quad (c_0 + c_2\vec{f}_1 \cdot \vec{f}_2)\delta^{(\mathrm{reg})}(\vec{r}),$$

$$H_{dd} \quad = \quad \frac{c_d}{r^3}\left[\vec{f}_1 \cdot \vec{f}_2 - 3(\vec{f}_1 \cdot \hat{r}) \cdot (\vec{f}_2 \cdot \hat{r})\right], \tag{6.4}$$

where H_0 describes the relative motional of the trap. We split H_s into spin independent and dependent parts, with the interaction coefficients listed below

$$c_0 \quad = \quad \frac{4\pi\hbar^2}{m}\frac{a_0 + 2a_2}{3}, \tag{6.5}$$

$$c_2 \quad = \quad \frac{4\pi\hbar^2}{m}\frac{a_2 - a_0}{3}. \tag{6.6}$$

Without considering the dipolar interaction and the Zeeman effect, the spin dependent scattering potential determines the magnetic ground state of the system, *e.g.*, $c_2 < 0(> 0)$ for a ferromagnetic (antiferromagnetic) ground state.

Due to the spin interaction term ($\propto \vec{f}_1 \cdot \vec{f}_2$) in H_s, there is spin mixing between the two spin states $|m_f = 0, m'_f = 0\rangle$ and $|1, -1\rangle$. Hereafter the spin states have been symmetrized and we have omitted the common $f = 1$ in the notation. The same notation will apply for $f = 2$. For ^{87}Rb atom with $f = 1$, the accepted scattering lengths are $a_0 = 101.8a_B$ and $a_2 = 100.4a_B$ [166, 167, 168], leading to $|c_2/c_0| \simeq 0.00462657$, and the spin mixing dynamics become much more sensitive to c_2 than c_0. It's easy to see that the total magnetization

is conserved in the spin mixing process. However, this is not the case for the spin dipolar interaction, as it drives the system to other spin states, *i.e.*, $|1, 1\rangle$, $|-1, -1\rangle$, $|0, 1\rangle$ and $|0, -1\rangle$. We further notice that $|c_d/c_2| \simeq 0.0902$, which means that the dipolar interaction can be treated as a perturbation. Thus, we assume the total magnetization is conserved, which limits our discussion to a two-level like system. The detailed analysis of this approximation, the relaxation due to the dipolar interaction, will be investigated later in this chapter. Under this circumstance, H_B only includes the second order Zeeman effect since the first order Zeeman effect cancels out due to the approximate conservation of system magnetization. For ^{87}Rb atom, $\delta(B) \simeq \pm 72 (\vec{f} \cdot \vec{B})^2$ Hz/Gauss^2 defined relative to the $m_f = 0$ state, with "+" sign corresponding to $f = 1$ and "$-$" to $f = 2$, respectively.

With the above simplification, the relative Hamiltonian in the subspace spanned by spin states $|0, 0\rangle$ and $|1, -1\rangle$ can be written as

$$H_{\text{rel}} = \begin{pmatrix} H_0 + c_0 \delta^{(\text{reg})}(\vec{r}) & \sqrt{2} c_2 \delta^{(\text{reg})}(\vec{r}) + \sqrt{2} \frac{c_d}{r^3} P_2(\cos\theta) \\ \sqrt{2} c_2 \delta^{(\text{reg})}(\vec{r}) + \sqrt{2} \frac{c_d}{r^3} P_2(\cos\theta) & H_0 + (c_0 - c_2) \delta^{(\text{reg})}(\vec{r}) + 2 \frac{c_d}{r^3} P_2(\cos\theta) + H_B \end{pmatrix} \quad (6.7)$$

Assuming a two-state expansion for the two-atom wave function

$$\psi(t) = \alpha_{0,0}(t) |0, 0\rangle \psi_{0,0}(\vec{r}_1, \vec{r}_2) + \alpha_{1,-1}(t) |1, -1\rangle \psi_{1,-1}(\vec{r}_1, \vec{r}_2), \quad (6.8)$$

the spin mixing element can be calculated as

$$\frac{\hbar \Omega}{2} = \int d\vec{r}_1 \int d\vec{r}_2 \psi_{0,0}^*(\vec{r}_1, \vec{r}_2) \langle 0, 0 | (H_s + H_{dd}) | 1, -1 \rangle \psi_{1,-1}(\vec{r}_1, \vec{r}_2). \quad (6.9)$$

The effective spin mixing frequency is defined as $f_{\text{eff}} \equiv \Omega_{\text{eff}}/(2\pi)$, where the effective angular Rabi frequency $\Omega_{\text{eff}} = \sqrt{\Delta^2 + \Omega^2}$ with $\Delta = (E_{1,-1} - E_{0,0})/\hbar$.

To our knowledge, the diagonalization of the relative Hamiltonian is almost impossible due to the entangling of the spin and spatial degrees of freedom even without the dipolar term ($c_d = 0$). Thus, we simply replace the true motional states of $|m_f, m_f'\rangle$ with the ground state of $\langle m_f, m_f' | H_{\text{rel}} | m_f, m_f' \rangle$, *i.e.*, neglect the off-diagonal spin mixing interaction. This approximation is valid as long as $|c_2/c_0| \ll 1$, which is the case for ^{87}Rb atom.

6.4 Approximations for motional states

The observed quantity in spin mixing dynamics is the effective Rabi frequency, which can be measured with relatively high precision (~ 0.1 Hz). However, the experimental data deviate from the simple theoretical estimate by up to 10% as shown in Refs. [62, 63]. One possible source of error is from the approximation of the motional wave function. To investigate it in detail, we study the spin mixing in various approximation schemes. We focus on a spherical harmonic trap where the dipolar effect turns out to be negligible, as this allows for a clear discussion of the motional state approximations. The harmonic trap is approximated from a true lattice potential $V(\vec{r}) = sE_r\sin^2(kr)$ with $s = 40$ and $\lambda_L = 2\pi/k = 840$nm as in Refs. [62, 63], which we will consistently use in our numerical simulation. Here k is the wave vector of the trap laser and $E_r = h^2/(2m\lambda_L^2)$ is the recoil energy. The trap frequency is calculated to be $\omega = 2\sqrt{s}E_r/\hbar \simeq (2\pi)41126.3$ Hz, which leads to a trap width $\sigma = \sqrt{\hbar/(\mu\omega)} = 0.0752$ μm. The dimensionless scattering lengths are $a_0/\sigma \simeq 0.0716559$ and $a_2/\sigma \simeq 0.0706704$. The average density with a Gaussian mode function is estimated to be

$$
\begin{aligned}
\langle n \rangle_0 &= 2\int |\phi|^4 d\vec{r} \\
&= \frac{1}{\sqrt{2}\pi^{3/2}w^3}.
\end{aligned}
\tag{6.10}
$$

Thus for ^{87}Rb atoms in the $f = 1$ manifold, $c_0\langle n \rangle_0/\hbar \simeq (2\pi)6589$ Hz, $c_2\langle n \rangle_0/\hbar \simeq (2\pi)(-30)$ Hz, and $c_d\langle n \rangle_0/\hbar \simeq (2\pi)2.71$ Hz, all much less than the trap level spacing. The relative strengths are $c_2/c_0 \simeq -0.00462657$ and $c_d/c_2 \simeq -0.0902$. The former ratio is the origin of c_2 sensitive spin mixing dynamics. The latter ratio allows for a perturbative treatment of the dipolar interaction. In the following, we will discuss various approximation schemes for the motional states, labelled as ϕ_0, $\phi^{(v)}$, ϕ_c, $\phi^{(e)}$, and $|\nu\rangle$, respectively.

6.4.1 ϕ_0

This is the approximation used in Refs. [62, 63]. The motional states for spin states $|0,0\rangle$ and $|1,-1\rangle$ are both assumed to be the ground state of H_0, *i.e.*,

$$
\psi_{0,0}(\vec{r}) = \psi_{1,-1}(\vec{r}) = \phi_0(\vec{r}) = \frac{1}{\pi^{3/4}\sigma^{2/3}}e^{-\frac{r^2}{2\sigma^2}}
\tag{6.11}
$$

with $\sigma = \sqrt{\hbar/(\mu\omega)}$. This approximation is developed because the motional wave function is insensitive to the relatively small scattering terms in both spin states. Since the contact interaction is only important near $r = 0$, the dimensionless spin-independent term $\tilde{c}_0 = c_0/(\pi^{3/2}\hbar\omega\sigma^3) = 0.08$ and the even smaller spin-dependent term $|c_2/c_0| = 0.0046$ only make the true motional states deviate negligibly from ϕ_0. Thus, this non-interacting basis is a good approximation. The bare detuning can be calculated as $\Delta = \langle\phi_0| - c_2\delta(\vec{r})|\phi_0\rangle = -c_2/(\pi^{3/2}\hbar\sigma^3)$. The bare Rabi frequency is $\Omega = |2\langle\phi_0|\sqrt{2}c_2\delta(\vec{r})|\phi_0\rangle| = 2\sqrt{2}|\Delta|$. So the effective Rabi frequency $f_{\text{eff}} = \sqrt{\Delta^2 + \Omega^2}/(2\pi) = 3|c_2|/(2\pi^{5/2}\hbar\sigma^3)$. This linear relation allows us to extract the absolute value of the scattering length difference directly from the experimentally measured Rabi frequency. The sign of this difference can be further determined by measuring the B-field dependence, which amounts to a positive shift in $E_{1,-1}$. If $c_2 < 0$, the Rabi frequency increases monotonically with B, while for $c_2 > 0$, the effective Rabi frequency first decreases with B till some finite value B_c (determined by c_2), and increases afterwards. For $f = 1$ ^{87}Rb atom with a predicted $c_2 < 0$, we expect that the effective Rabi frequency increases monotonically with B, which indeed has been confirmed in the experiments [63, 64].

6.4.2 $\phi^{(v)}$

To find a more accurate motional ground state, we use the Gaussian ansatz for each spin state $|m_f, m'_f\rangle$ with the widths as variational parameters

$$\psi_{m_f,m'_f}(\vec{r}) = \frac{1}{\pi^{3/4}w_{m_f,m'_f}^{3/2}}\exp\left(-\frac{r^2}{2w_{m_f,m'_f}^2}\right). \tag{6.12}$$

Such an approach has been used extensively in the past [163, 164]. The energy functional is

$$\frac{E_{m_f,m'_f}}{\hbar\omega} = \frac{3}{4}\left(\frac{\sigma^2}{w_{m_f,m'_f}^2} + \frac{w_{m_f,m'_f}^2}{\sigma^2}\right) + \frac{c_{m_f,m'_f}}{\pi^{3/2}\hbar\omega w_{m_f,m'_f}^3} \tag{6.13}$$

with $c_{0,0} = c_0$ and $c_{1,-1} = c_0 - c_2$. The actual width w_{m_f,m'_f} is found by minimizing the energy functional for each spin state separately. Using the same trap parameters, we find $w_{0,0}/\sigma \simeq 1.036$ and $w_{1,-1}/\sigma \simeq 1.037$, respectively. The variational widths are larger than

the trap width σ because the two atoms are repelling each other overall. The tiny deviation of the ansatz wave functions from the harmonic ground state reinforces the validity of the ϕ_0 approximation. The bare Rabi frequency can be expressed as

$$\Omega = \frac{2\sqrt{2}|c_2|}{\pi^{3/2}\hbar(w_{0,0}w_{1,-1})^{3/2}}. \tag{6.14}$$

Compared with the ϕ_0 approximation, the calculated effective Rabi frequency is not strictly linear with c_2 because the motional wave functions also depend on c_2. However, we find that the nonlinearity is very weak based on numerical work, again due to the fact that $|c_2/c_0| \ll 1$.

6.4.3 ϕ_c

A mean field approach is sometimes used in the literature where the two-atom motional state $\psi_{m_f,m'_f}(\vec{r}_1, \vec{r}_2)$ is approximated by $\phi_c^{m_f,m'_f}(\vec{r}_1)\phi_c^{m_f,m'_f}(\vec{r}_2)$ as for a two-atom condensate with $\phi_c^{m_f,m'_f}(\vec{r})$ obtained from the corresponding Gross-Pitaevskii equation

$$\left[-\frac{\hbar^2}{2m}\nabla_{\vec{r}}^2 + \frac{1}{2}m\omega^2 r^2 + V_{\text{int}}[\phi_c]\right]\phi_c(\vec{r}) = \mu_c\phi_c, \tag{6.15}$$

with $V_{\text{int}} = c_0|\phi_c(\vec{r})|^2$, or $V_{\text{int}} = (c_0 - c_2)|\phi_c(\vec{r})|^2$ for state $|0,0\rangle$ and $|1,-1\rangle$, respectively. We still use a Gaussian ansatz for each spin state as in the $\phi^{(\text{v})}$ approximation. In this single-atom picture, the calculated widths become $w_{0,0(1,-1)}/\Sigma = 1.01910(1.01918)$ with $\Sigma = \sigma/\sqrt{2}$. This means that the effective repulsion between the two atoms is weaker compared to the $\phi^{(\text{v})}$ approximation. Because we are dealing with two separate atoms, the bare detuning is now twice that of the single atom detuning, $i.e.$, $\Delta = 2(\varepsilon_{1,-1} - \varepsilon_{0,0})/\hbar$. The bare Rabi frequency is found to be

$$\begin{aligned}\Omega &= \left|-\frac{2\sqrt{2}c_2}{\hbar}\int d\vec{r}\phi_c^{(0,0)}(r)\phi_c^{(0,0)}(r)\phi_c^{(1,-1)}(r)\phi_c^{(1,-1)}(r)\right| \\ &= \frac{2\sqrt{2}|c_2|}{\pi^{3/2}\hbar(w_{0,0}^2 + w_{1,-1}^2)^{3/2}}. \end{aligned} \tag{6.16}$$

6.4.4 $\phi^{(\text{e})}$

The spectrum of $H_0 + c_{m_f,m'_f}\delta^{(\text{reg})}(\vec{r})$ can be solved exactly [41]. This prompts us to use the corresponding analytic ground state as the motional wave function. Using dimensionless

length ($\sigma \equiv \sqrt{\hbar/(\mu\omega)}$) and energy ($\hbar\omega$) scales appropriate for the harmonic trap, the solutions are given by (omitting the constant quadratic Zeeman shift)

$$
\begin{aligned}
E_{m_f,m_f'} &= 2\nu_{m_f,m_f'} + \frac{3}{2}, \\
\frac{\pi}{\tilde{c}_{m_f,m_f'}} &= \frac{\Gamma(-\nu_{m_f,m_f'})}{\Gamma(-\nu_{m_f,m_f'} - \frac{1}{2})}, \\
\psi_{m_f,m_f'}(\vec{r}) &= A_{m_f,m_f'} e^{-\frac{r^2}{2}} U\left(-\nu_{m_f,m_f'}, \frac{3}{2}; r^2\right) Y_{00}(\theta,\phi),
\end{aligned}
\tag{6.17}
$$

where $\tilde{c}_{m_f,m_f'} = c_{m_f,m_f'}/(\hbar\omega\sigma^3)$ and the normalization constant $A_{m_f,m_f'}$ is given by

$$
A_{m_f,m_f'} = \sqrt{\frac{2}{\pi}} \left[\frac{\Gamma(-\nu_{m_f,m_f'})\Gamma(-\nu_{m_f,m_f'} - \frac{1}{2})}{\mathcal{F}(-\nu_{m_f,m_f'}) - \mathcal{F}(-\nu_{m_f,m_f'} - \frac{1}{2})} \right]^{1/2}.
\tag{6.18}
$$

We expand the above confluent hypergeometric function U around $r \to 0$, finding that

$$
\begin{aligned}
U\left(-\nu, \frac{3}{2}; r^2\right) &\to \frac{\sqrt{\pi}}{\Gamma(-\nu)r} - \frac{2\sqrt{\pi}}{\Gamma(-\nu - 1/2)} \\
&\propto 1 - \frac{\tilde{c}}{2\pi r} \\
&= 1 - \frac{c}{2\pi\hbar\omega\sigma^3}\frac{\sigma}{r} \\
&= 1 - \frac{4\pi\hbar^2 a/m}{2\pi\hbar\omega\sigma^2}\frac{1}{r} \\
&= 1 - \frac{a}{r},
\end{aligned}
\tag{6.19}
$$

consistent with the result in the homogeneous space as the trap effect is negligible for $r \to 0$. Thus, the bare Rabi frequency can be calculated as

$$
\begin{aligned}
\Omega &= \left| -\frac{2\sqrt{2}c_2}{\hbar} \langle \psi_{0,0} | \delta^{(\text{reg})} | \psi_{1,-1} \rangle \right| \\
&= \left| \frac{2\sqrt{2}c_2 A_{0,0} A_{1,-1}}{\hbar\Gamma(-\nu_{0,0} - \frac{1}{2})\Gamma(-\nu_{1,-1} - \frac{1}{2})} \right|.
\end{aligned}
\tag{6.20}
$$

Here the regularization is necessary to remove the divergence. The analytic wave function of $\psi_{0,0}$ is compared to that using $\phi^{(\text{v})}$ approximation in Fig. 6.1.

6.4.5 $|\nu\rangle$

All of the above approximations neglect the coupling terms in the estimation of the motional ground state, so the motional state used is actually not the true motional state of each spin
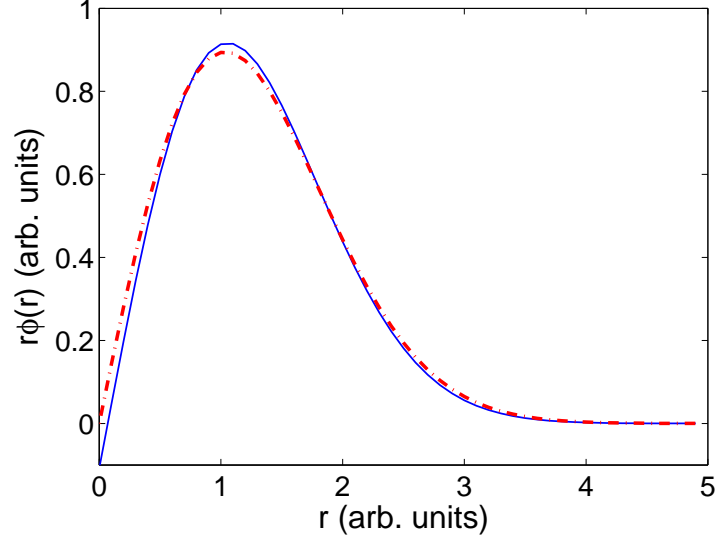
Figure 6.1: Comparison of the wave functions. The solid line is for the analytic result, and the dash-dotted line is for the $\phi^{(\mathrm{v})}$ approximation. All other gaussian ansatz wave functions (except ϕ_c) are almost indistinguishable from that of the $\phi^{(\mathrm{v})}$ approximation.

state. To treat this problem more accurately, we expand the motional state into the complete basis of $H_0 + c_0 \delta^{(\mathrm{reg})}(\vec{r})$, labelled as $|\nu\rangle$. The relative wave function is then written as

$$|\Psi(t)\rangle = \sum_\nu (\alpha_\nu(t)|m_f = 0, m'_f = 0\rangle|\nu\rangle + \beta_\nu(t)|m_f = 1, m'_f = -1\rangle|\nu\rangle). \qquad (6.21)$$

In the interaction picture, the coupled equations become

$$i\hbar\dot{\alpha}_\nu = \sqrt{2}c_2 \sum_{\nu'} \Gamma_{\nu,\nu'} e^{2i\omega t(\nu-\nu')} \beta_{\nu'},$$

$$i\hbar\dot{\beta}_\nu = -c_2 \sum_{\nu'} \Gamma_{\nu,\nu'} e^{2i\omega t(\nu-\nu')} \beta_{\nu'} + \sqrt{2}c_2 \sum_{\nu'} \Gamma_{\nu,\nu'} e^{2i\omega t(\nu-\nu')} \alpha_{\nu'} + \delta(B)\beta_\nu. \quad (6.22)$$

Here $\Gamma_{\nu,\nu'}$ is proportional to the coupling matrix element

$$\begin{aligned}
\Gamma_{\nu,\nu'} &\equiv \langle \nu | \delta^{(\mathrm{reg})}(\vec{r}) | \nu' \rangle \\
&= \left[\left(\frac{\partial}{\partial r} r \Psi_\nu(\vec{r}) \right) \left(\frac{\partial}{\partial r} r \Psi_{\nu'}(\vec{r}) \right) \right]_{r \to 0} \\
&= \frac{2\hbar\omega}{c_0} \left(\frac{1}{\mathcal{F}(-\nu) - \mathcal{F}(-1/2 - \nu)} \right)^{1/2} \left(\frac{1}{\mathcal{F}(-\nu') - \mathcal{F}(-1/2 - \nu')} \right)^{1/2}. \quad (6.23)
\end{aligned}$$

We then evolve the system from the initial state $|0,0\rangle|0\rangle$. The population of $P_{0,0}(t) \equiv \sum_\nu |\alpha_\nu(t)|^2$ in the spin state $|0,0\rangle$ and $P_{1,-1}(t) \equiv \sum_\nu |\beta_\nu(t)|^2 = 1 - P_{0,0}(t)$ in $|1,-1\rangle$, can be independently obtained from a spin selective measurement. In Fig. 6.2, we show the

84

time evolution for both $P_{0,0}$ and $P_{1,-1}$ at an external magnetic field of $B = 0.4$ Gauss. We see that almost perfect oscillations exist in each spin state. This is true again due to the fact $|c_2/c_0| \ll 1$, which is the basis of all the above approximate treatment schemes.
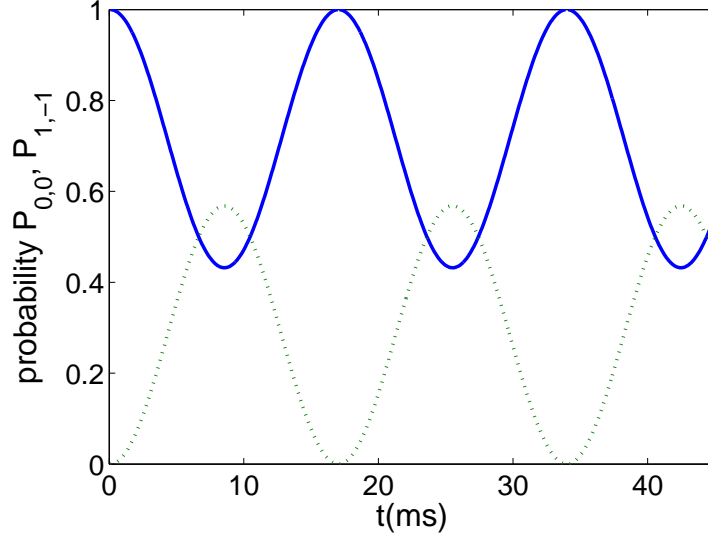
Figure 6.2: Population of different spin states in the spin mixing calculated by complete basis expansion. The solid line is for $P_{0,0}$, while the dashed line is for $P_{1,-1}$. The magnetic field is fixed at 0.4 Gauss.

6.4.6   Numerical results

We calculate spin mixing frequency under various approximations with the results shown in Table 6.1. We have chosen the scattering lengths as the accepted ones, $a_0 = 101.8a_B$ and $a_2 = 100.4a_B$. The B-field is 0.4 Gauss. The experimental value of $f_{\text{eff}}^{(\text{exp})}$ is found to be around 47 Hz in this case [63]. We take the result using a complete basis expansion as the "true" value and compare other frequencies to it. From the results in Table 6.1, we comment on three points. First, different theoretical estimates can constitute errors up to about 10%. The approximation in Ref. [63] thus has a noticeable error. Second, the experimental result is far away from the true value. Even after including the anharmonic correction, this result still does not agree with the true value very well. Third, the spin mixing frequencies with $\phi^{(\text{e})}$ and $|\nu\rangle$ approximations are very close to each other, thus both motional states are almost the ground state of the relative Hamiltonian.

To reveal the scattering length dependence on the spin mixing frequency for various

approximation schemes, we present our numerical results of the effective Rabi frequency versus $c_2 \propto \Delta a [\equiv a_2 - a_0]$ in Fig. 6.3. We fix c_0 to the commonly accepted value, since spin mixing dynamics are insensitive to c_0. From Fig. 6.3, we can extract the scattering length difference Δa from the corresponding effective Rabi frequency measurement.

Table 6.1: Spin mixing frequency using various approximation schemes at $B = 0.4$ Gauss. "EXP" stands for the experimental value. All of the errors are defined relative to that using the $|\nu\rangle$ approximation.

	$\phi^{(e)}$	$|\nu\rangle$	ϕ_c	ϕ_0	$\phi^{(v)}$	EXP
$f_{\text{eff}}(\text{Hz})$	59.03	58.93	55.32	54.73	53.35	47
error	0.17%	0%	6.13%	7.13%	9.47%	20.24%
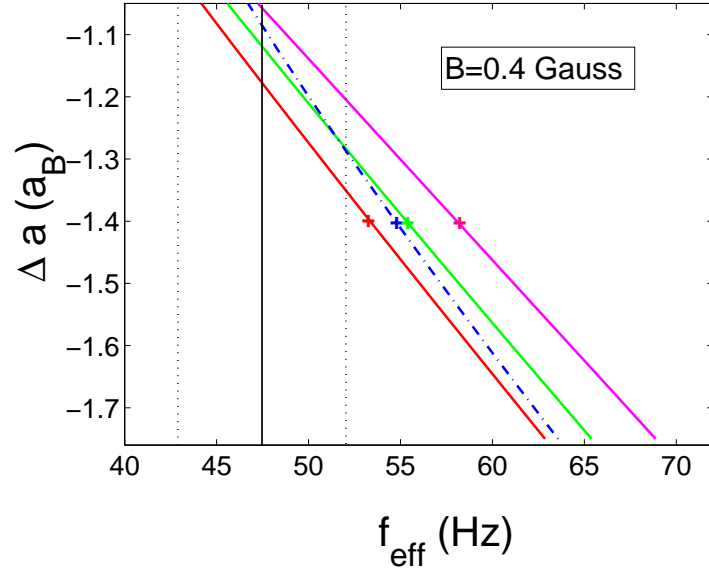
Figure 6.3: Scattering length difference versus spin mixing frequency. From left to right, solid lines represent $\phi^{(v)}$, ϕ_c, and $\phi^{(e)}$. The dash-dot line stands for ϕ_0. Results for approximation $|v\rangle$ is almost indistinguishable from that of $\phi^{(e)}$. The spin mixing frequencies at predicted scattering length difference for different approximations are labelled with "+". The experimental value is located on the vertical solid line. The vertical dotted lines mark the boundary of the estimated experimental error.

From Fig. 6.3, we can see that the scattering length difference is very sensitive to the spin mixing frequency. A 3.2 Hz frequency error can cause a $0.1a_B$ error in the scattering length difference. This surely calls for a more precise measurement for the spin mixing frequency. We also note that the theoretical values are almost all linear in Δa, again due

to the fact that $|c_2/c_0| \ll 1$.

6.5   Cylindrical traps with dipolar interaction

While the dipolar effect is negligible in a spherical harmonic trap, it may be enhanced in a cylindrical harmonic trap [69]. To calibrate the dipolar effect in such a trap with $\lambda = \omega_z/\omega_\rho$, we adopt the $\phi^{(v)}$ approximation. We take a Gaussian ansatz with its widths $w_{\rho 1/z1}$ as variational parameters

$$\phi_{1,-1}(\vec{r}) = \frac{1}{\pi^{3/4}(w_{\rho 1}^2 w_{z1})^{1/2}} \exp\left(-\frac{x^2 + y^2}{2w_{\rho 1}^2} - \frac{z^2}{2w_{z1}^2}\right). \tag{6.24}$$

The cylindrically symmetric z-axis is chosen as the quantization axis for spin dipoles. The relative energy functional (omitting the constant quadratic Zeeman shift) for minimization then becomes

$$\begin{aligned}
\frac{E}{\hbar\omega_\rho} &= \frac{1}{4}\left(2\frac{a_\rho^2}{w_{\rho 1}^2} + \frac{a_\rho^2}{w_{z1}^2}\right) + \frac{1}{4}\left(2\frac{w_{\rho 1}^2}{a_\rho^2} + \lambda^2\frac{w_{z1}^2}{a_\rho^2}\right) \\
&+ \frac{c_0 - c_2}{\pi^{3/2} w_{\rho 1}^2 w_{z1} \hbar\omega_\rho} - \frac{2}{3\sqrt{\pi}}\frac{c_d}{w_{\rho 1}^2 w_{z1} \hbar\omega_\rho}\chi(\kappa_1),
\end{aligned} \tag{6.25}$$

with

$$\begin{aligned}
\chi(\kappa) &= \frac{2\kappa^2 + 1 - 3\kappa^2 H(\kappa)}{2(\kappa^2 - 1)} + (\kappa^2 - 1)H(\kappa), \\
H(\kappa) &= \frac{\tanh^{-1}\sqrt{1 - \kappa^2}}{\sqrt{1 - \kappa^2}}.
\end{aligned} \tag{6.26}$$

$a_z = \sqrt{\hbar/(\mu\omega_z)}$ is the axial width of the trap, and $\kappa_1 = w_{\rho 1}/w_{z1}$ is the aspect ratio of the variational ground state, which is not spherical (or $\kappa_1 \neq 1$) even in a spherical harmonic trap with $\lambda = 1$ because of the dipolar interaction [163, 164]. The functions $\chi(\kappa)$ and $H(\kappa)$ are plotted in Figs. 6.4 and 6.5, respectively. $\phi_{0,0}(\vec{r})$ is obtained from the result of $\phi_{1,-1}(\vec{r})$ by excluding the dipolar interaction or taking $c_d = 0$ and adjusting to its own s-wave scattering strength by taking $c_2 = 0$. The corresponding widths are denoted as $w_{\rho 0/z0}$ and the ratio as $\kappa_0 = w_{\rho 0}/w_{z0}$.

We have used the anisotropic pseudopotential in the evaluation of the dipolar term in Eq. (6.25). In momentum space, the pseudopotential is given by [169]

$$v(\vec{k}, \vec{k}') = -\frac{\sqrt{5}\hbar^2 a_{sd}}{2\pi^2 m}\left[P_2(\cos\theta_{k'}) + \left(\frac{k}{k'}\right)^2 P_2(\cos\theta_k)\right], \tag{6.27}$$
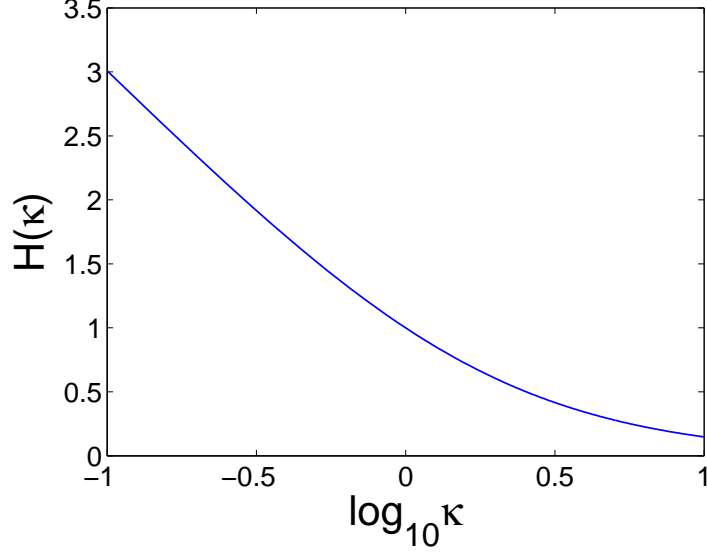
Figure 6.4: The graph of $H(\kappa)$.

with

$$a_{sd} = \frac{\sqrt{2}}{12\sqrt{5}} \frac{mc_d}{\hbar^2}.$$ (6.28)

Because the complete motional wave function is Gaussian shaped, we find that $\langle\phi_{1,-1}|H_{dd}|\phi_{0,0}\rangle$ can also be evaluated analytically. The bare Rabi frequency is calculated to be

$$\hbar\frac{\Omega}{2} = \left| \frac{1}{3}\sqrt{\frac{2}{\pi}} c_d \left(\frac{1}{w_{\rho 1} w_{z1}^{1/2} w_{\rho 0} w_{z0}^{1/2}} \frac{2\kappa_0^2 + 1 - 3\kappa_0^2 H(\kappa_0)}{2(\kappa_0^2 - 1)} + \frac{w_{\rho 1} w_{\rho 0}}{w_{z1}^{9/2} w_{z0}^{1/2}} \frac{\kappa_1^2 - 1}{\kappa_1^4} H(\kappa_0) \right) \right|. (6.29)$$

In Fig. 6.6, we show the dependence of f_{eff} on the trap aspect ratio λ at an external magnetic field of $B = 0.1$ Gauss. To facilitate a fair comparison, we have fixed the geometric average of the trap frequencies $(\omega_\rho^2 \omega_z)^{1/3}$ to the value for the spherical trap of $\omega_\rho = \omega_z = (2\pi)41.1$ kHz [63]. From Fig. 6.6, we can see that the dipolar induced shift (frequency of solid line minus dotted line) based on various approximation schemes is much larger. Furthermore, it remains rather stable. Thus we conclude that, although the different approximations may not lead to very accurate motional states, the resulting Rabi frequency is highly accurate. In fact, after careful comparison, we find that the dipolar induced shifts from different approximation schemes differ by less than 1%, which is much less than the estimated noise.

In Fig. 6.7, we show the B-field dependence of f_{eff}. Based on the current experimental
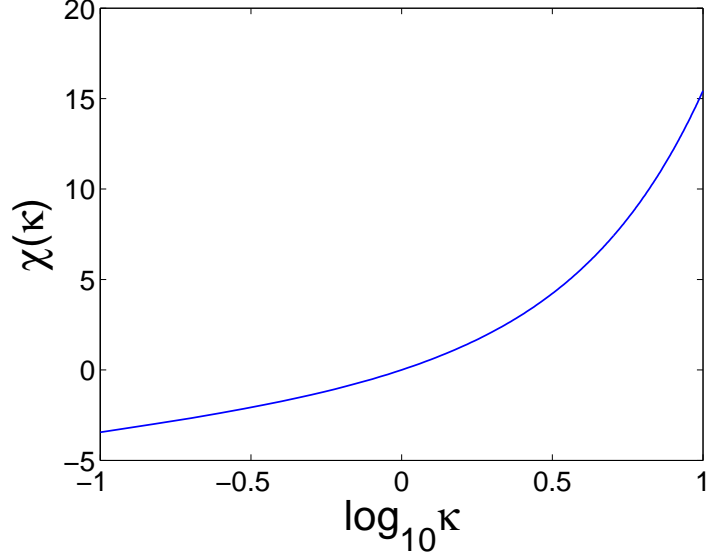
Figure 6.5: The graph of $\chi(\kappa)$.

sensitivity, dipolar effects should be detectable for $\lambda > 3$ and can constitute a more than 10% increase in f_{eff}. They are minimized for a spherical trap as shown in Fig. 6.7 with an actual shift of about 10^{-6} or less for the experiment of Ref. [63].

6.6 Spin relaxation processes

With the dipolar interaction, the conservation of the total magnetization is only approximately valid. To include spin relaxation in the spin mixing dynamics, we need to calculate the full system dynamics in the spin space spanned by all the possible basis $|e_1\rangle = |0,0\rangle$, $|e_2\rangle = |1,-1\rangle$, $|e_3\rangle = |1,1\rangle$, $|e_4\rangle = |-1,-1\rangle$, $|e_5\rangle = |0,1\rangle$, and $|e_6\rangle = |0,-1\rangle$. The spin states with different magnetization can only be coupled by the dipolar interaction. The relative Hamiltonian in the above spin basis has a 6×6 structure to the first approximation when each element has only motional dependence. We list the non-trivial matrix elements
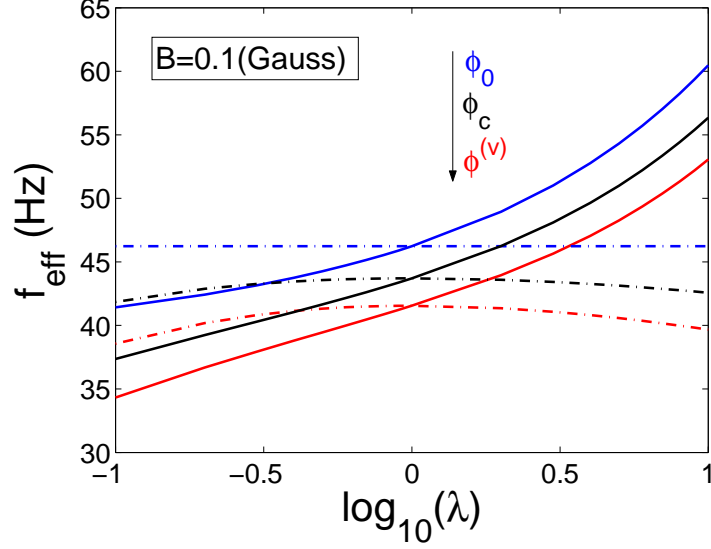
Figure 6.6: The aspect ratio dependence of f_{eff} computed with the three approximation schemes as labelled. The solid lines include the dipolar interaction, while the dashed-dot lines are the corresponding ones without the dipolar interaction. The geometric average of the trap frequency is fixed at $(\omega_\rho^2 \omega_z)^{1/3} = (2\pi)41.1$ kHz.

in the following ($\langle e_i|H|e_j\rangle = \langle e_j|H|e_i\rangle^*$):

$$\langle e_1|H|e_1\rangle = H_0 + c_0\delta^{(\text{reg})}(\vec{r}),$$

$$\langle e_2|H|e_1\rangle = \sqrt{2}c_2\delta^{(\text{reg})}(\vec{r}) + \sqrt{2}\frac{c_d}{r^3}P_2(\cos\theta),$$

$$\langle e_3|H|e_1\rangle = -\sqrt{\frac{24\pi}{5}}\frac{c_d}{r^3}Y_{2,-2}(\theta,\phi),$$

$$\langle e_4|H|e_1\rangle = -\sqrt{\frac{24\pi}{5}}\frac{c_d}{r^3}Y_{2,2}(\theta,\phi),$$

$$\langle e_2|H|e_2\rangle = H_0 + (c_0 - c_2)\delta^{(\text{reg})}(\vec{r}) + 2\frac{c_d}{r^3}P_2(\cos\theta),$$

$$\langle e_5|H|e_2\rangle = -\sqrt{\frac{12\pi}{5}}\frac{c_d}{r^3}Y_{2,-1}(\theta,\phi),$$

$$\langle e_6|H|e_2\rangle = -\sqrt{\frac{12\pi}{5}}\frac{c_d}{r^3}Y_{2,1}(\theta,\phi),$$

$$\langle e_3|H|e_3\rangle = H_0 + (c_0 + c_2)\delta^{(\text{reg})}(\vec{r}) - 2\frac{c_d}{r^3}P_2(\cos\theta),$$

$$\langle e_5|H|e_3\rangle = \sqrt{\frac{24\pi}{5}}\frac{c_d}{r^3}Y_{2,1}(\theta,\phi),$$

$$\langle e_4|H|e_4\rangle = H_0 + (c_0 + c_2)\delta^{(\text{reg})}(\vec{r}) - 2\frac{c_d}{r^3}P_2(\cos\theta),$$

$$\langle e_6|H|e_4\rangle = \sqrt{\frac{24\pi}{5}}\frac{c_d}{r^3}Y_{2,-1}(\theta,\phi),$$

$$\langle e_5|H|e_5\rangle = H_0 + (c_0 + c_2)\delta^{(\text{reg})}(\vec{r}) + \frac{c_d}{r^3}P_2(\cos\theta),$$
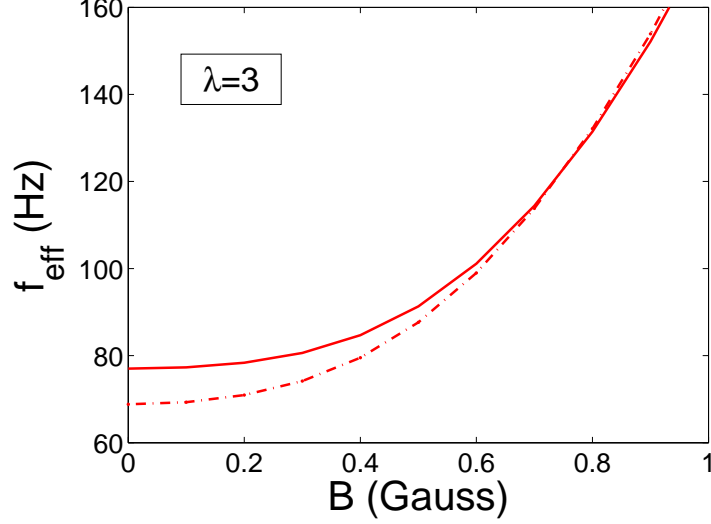
Figure 6.7: The B-field dependence of f_{eff} computed within the $\phi^{(\text{v})}$ approximation for $\lambda = 3$. The solid line includes the dipolar interaction while the dashed-dot line does not. Here, unlike in Fig. 6.6, we fix $\omega_\rho = (2\pi)41.1$ kHz.

$$\langle e_6|H|e_5\rangle = -\sqrt{\frac{24\pi}{5}}\frac{c_d}{r^3}Y_{2,2}(\theta,\phi),$$

$$\langle e_6|H|e_6\rangle = H_0 + (c_0 + c_2)\delta^{(\text{reg})}(\vec{r}) + \frac{c_d}{r^3}P_2(\cos\theta).$$

$Y_{l,m}(\theta,\phi)$ are the usual spherical harmonics. In a spherical harmonic trap, we choose the eigenstates of $\langle e_1|H|e_1\rangle$, labelled as $|\nu\rangle$, as the complete motional basis. In the diagonalization procedure, we have used the fact that $L_z + F_z$ is a conserved quantity [76]. This can be easily seen from the expression $H_{dd} \propto \sum_{q=-2}^{2}(-1)^q Y_{-q}^{(2)}[F_1 \otimes F_2]_q^{(2)}$ [170]. We consider the initial wave function as $|e_1\rangle|\nu = 0\rangle$. It implies $L_z = 0$ and $F_z = 0$, which rules out the unmatched basis, *i.e.*, those basis states with $L_z + F_z \neq 0$. Since the dipolar interaction is weak, we first use perturbation methods to estimate the transition amplitude, *e.g.*, $|e_2\rangle = |1,-1\rangle \leftrightarrow |e_5\rangle = |0,1\rangle$. The energy detuning is about $\hbar\omega$, and the dipolar interaction about c_d/a_{ho}^3. With the help of the first order perturbation approach, we estimate the transition amplitude as $\sim c_d/(a_{ho}^3\hbar\omega) \sim 10^{-4}$. Thus, starting from spin states in the manifold $|e_1\rangle$ and $|e_2\rangle$, the probability outside this manifold is on the order of 10^{-8}.

To accurately calculate the relaxation rate, we need to study the full system dynamics. We first carry out numerical simulation for a vanishing magnetic field. We evolve the system from state $|e_1\rangle|\nu = 0\rangle$, and find the almost perfect Rabi oscillation within the manifold $|e_1\rangle$

and $|e_2\rangle$. The wave function at any time t can be written as

$$\Psi(t) = \sum_{i=1}^{6} \sum_{p} \alpha_{i,p} |e_i\rangle |p^{(i)}\rangle. \tag{6.30}$$

$|p^{(i)}\rangle$ is the motional eigenstate for spin state $|e_i\rangle$ which may have angular dependence. The population outside this spin manifold is denoted as $P_{\text{out}} \equiv \sum_{i=3}^{6} \sum_{p} |\alpha_{i,p}|^2$. The numerical results are shown in Fig. 6.8. We can see that P_{out} is typically very small, with the maximal probability less than 10^{-6} in the first oscillation period.
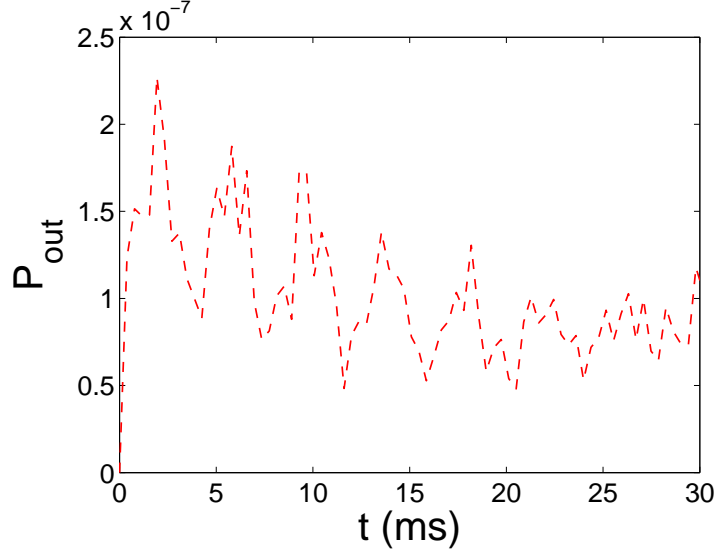
Figure 6.8: The spin relaxation due to the dipolar interaction is shown for the first oscillation period. The trap parameters are the same as before. The external B-field is 0.

At finite values of the B-field, except for accidental resonances when other spin states in higher motional states are shifted into near resonance with the two-state doublet in the ground motional state, the linear Zeeman effect generally leads to large detunings, further validating the approximation. The pictorial illustration is shown in Figs. 6.9 and 6.10, for the off-resonance case ($B = 0$) and the on-resonance case ($B = B_c \simeq \hbar\omega/(\mu_B g_f m_F)$), respectively. Even at accidental resonances, the total population out of the two-state doublet is found to be only less than 10^{-3} for a spherical trap, as shown in Fig. 6.11.

For a cylindrical trap, we use the same technique as mentioned above. We find that the leakage is only several times enhanced and thus can be neglected. We conclude that the spin relaxation is always negligible in the typical cases we consider. This conclusion is
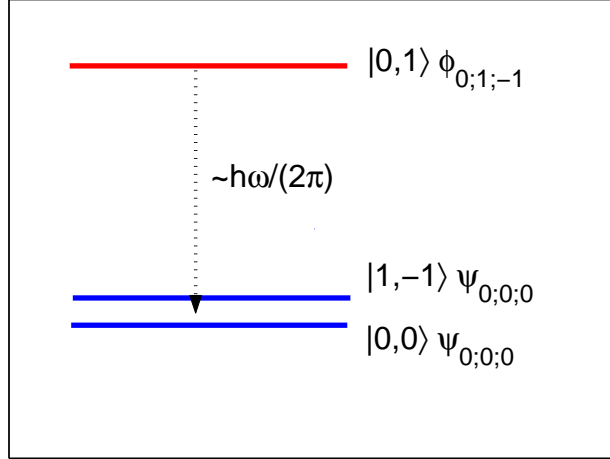
Figure 6.9: Illustration of some energy levels at $B = 0$. The detuning between the spin state $|0, 1\rangle$ and the two-state doublet of $|0, 0\rangle$ and $|1, -1\rangle$ is about $\hbar\omega$. $\psi_{0;0;0}$ is the motional ground state, and $\phi_{0;1;-1}$ is the first excited motional state. Both are expressed in the spherical coordinate. The graph is not drawn to scale.

found to remain true for $f = 2$.

6.7 The $f = 2$ Zeeman manifold

We now consider two ^{87}Rb atoms with $f = 2$. In this case, three s-wave scattering lengths a_F ($F = 0, 2, 4$) are required to describe the collisional process with each parameter corresponding to the scattering in the total spin F channel. The phase diagram for the magnetic ground state of a condensate has been investigated in Ref. [171]. In addition to the ferromagnetic and antiferromagnetic phase as in $f = 1$, the cyclic phase can also arise. The extraction of the scattering length differences is more complicated as it requires frequency measurements of spin mixing dynamics in two different spin channels [64]. The experimental results in Ref. [64] favor the antiferromagnetic ground state, but the error bars touch the phase boundary to the cyclic phase. Thus, the extraction of the scattering length differences from frequency measurements should also consider the error due to motional approximation. Similar analysis can be done as in the $f = 1$ case and the error due to the motional approximation is found to be of the same order. So we put our emphasis on the dipolar effect and omit the analysis on the motional state approximation here.

The total magnetization is still assumed to be conserved as the dipolar relaxation is
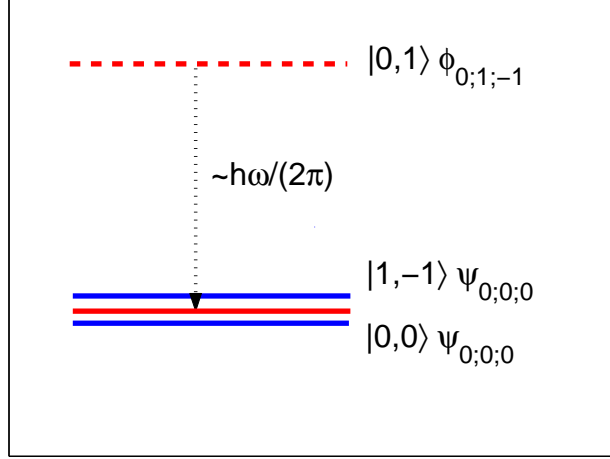
Figure 6.10: Illustration of some energy levels at $B = B_c$. The spin state $|0, 1\rangle$ is brought into near resonance with the two-state doublet of $|0, 0\rangle$ and $|1, -1\rangle$.

negligible. Different from the $f = 1$ case, there are more possibilities in the spin mixing dynamics for $f = 2$. For example, starting from $|0, -2\rangle$, the system evolves in the spin space spanned by $|0, -2\rangle$ and $|-1, -1\rangle$, which resembles the two-level Rabi oscillation as in $f = 1$. If it starts from $|0, 0\rangle$, the system evolves in the spin space spanned by $|0, 0\rangle$, $|1, -1\rangle$ and $|2, -2\rangle$, which has a three-level structure. In this case, there is an obvious deviation from pure sinusoidal oscillation, as for a two-level system.

Analogous to the case of $f = 1$, we can separate the total Hamiltonian into the center of mass (CM) and the relative (rel) motion $H = H_{\mathrm{CM}} + H_{\mathrm{rel}}$. Different from that in $f = 1$, the scattering interaction has three channels

$$H_s = (g_0 \mathcal{P}_0 + g_2 \mathcal{P}_2 + g_4 \mathcal{P}_4) \delta^{(\mathrm{reg})}(\vec{r}), \tag{6.31}$$

with $g_F = 4\pi\hbar^2 a_F / m$ ($F = 0, 2, 4$). $\mathcal{P}_F$ is the projector onto the total spin F channel. It can also be written as $H_s = c_0 + c_1 \vec{f}_1 \cdot \vec{f}_2 + c_2 \mathcal{S}_0$, where $\mathcal{S}_0$ is the projector onto the singlet subspace [171]. The respective parameters are listed below

$$
\begin{aligned}
c_0 &= \frac{4\pi\hbar^2}{m} \frac{4a_2 + 3a_4}{7}, \\
c_1 &= \frac{4\pi\hbar^2}{m} \frac{a_4 - a_2}{7}, \\
c_2 &= \frac{4\pi\hbar^2}{m} \frac{5(7a_0 - 10a_2 + 3a_4)}{7}.
\end{aligned}
\tag{6.32}
$$
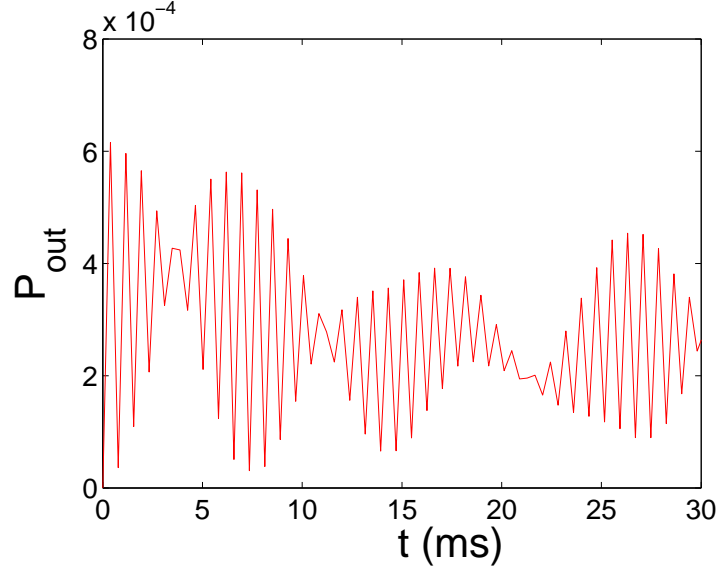
Figure 6.11: The spin relaxation due to the dipolar interaction is shown for the first oscillation period. The trap parameters are the same as before. The external B-field is chosen to be at near resonance with the two-state doublet in the ground motional state.

Another useful representation is to express the singlet operator as [172]

$$\mathcal{S}_0 = \frac{1}{3} \left[(\vec{f_1} \cdot \vec{f_2})^2 - 1 \right]. \tag{6.33}$$

For $f = 2$ ^{87}Rb atom, the most recent scattering lengths are $a_0 = (87.93 \pm 0.2) a_B$, $a_2 = (91.28 \pm 0.2) a_B$ and $a_4 = (98.98 \pm 0.2) a_B$ [64], which are used in our numerical calculation. The Landé g-factor is $\mathbf{g}_2 = -\mathbf{g}_1 = 1/2$, so c_d is the same as in the $f = 1$ case.

6.7.1 $|-1, -1\rangle$ and $|0, -2\rangle$

First we consider the spin mixing dynamics between states $|-1, -1\rangle$ and $|0, -2\rangle$, where the procedure parallels that of $f = 1$ considered earlier. In the Hilbert space spanned by the spin states $|-1, -1\rangle$ and $|0, -2\rangle$, the scattering potential is given by

$$\begin{pmatrix} c_0 + c_1 & 2\sqrt{3}c_1 \\ 2\sqrt{3}c_1 & c_0 \end{pmatrix} \delta^{(\text{reg})}(\vec{r}), \tag{6.34}$$

and the dipolar interaction is

$$\frac{c_d}{r^3} P_2(\cos\theta) \begin{pmatrix} -2 & 2\sqrt{3} \\ 2\sqrt{3} & 0 \end{pmatrix}. \tag{6.35}$$

95

Similar to the $f = 1$ case, we use a Gaussian ansatz to calculate the effective Rabi frequency. The numerical results are shown in Figs. 6.12 and 6.13, respectively. We can see that the dipolar effect is enhanced to the same order for both $\lambda \ll 1$ and $\lambda \gg 1$, with the latter of $\lambda = 10$ having an even stronger dipolar effect than the former of $\lambda = 1/10$. The spin dipolar interaction induces a frequency shift of about 13 Hz for $\lambda = 3$ and $\lambda = 1/4$ at a magnetic field $B = 0.4$ Gauss. However, the relative shift becomes small compared to that in $f = 1$. The B-field dependence of f_{eff} shows different behavior from that of the $f = 1$ case: the dipolar interaction lowers (raises) the frequency for $\lambda > 1$ ($\lambda < 1$).

Figure 6.12: The aspect ratio dependence of f_{eff} computed within the $\phi^{(v)}$ approximation. The solid line includes the dipolar interaction, while the dashed line does not. Here we fix the geometric average of the trap frequency $(\omega_\rho^2 \omega_z)^{1/3} = (2\pi)41.1$ (kHz).

6.7.2 $|0, 0\rangle$, $|1, -1\rangle$ and $|2, -2\rangle$

Different from the two-level system, we consider spin mixing in the three-state manifold of $|0, 0\rangle$, $|1, -1\rangle$, and $|2, -2\rangle$. In the basis order of $|0, 0\rangle$, $|1, -1\rangle$ and $|2, -2\rangle$, the matrix
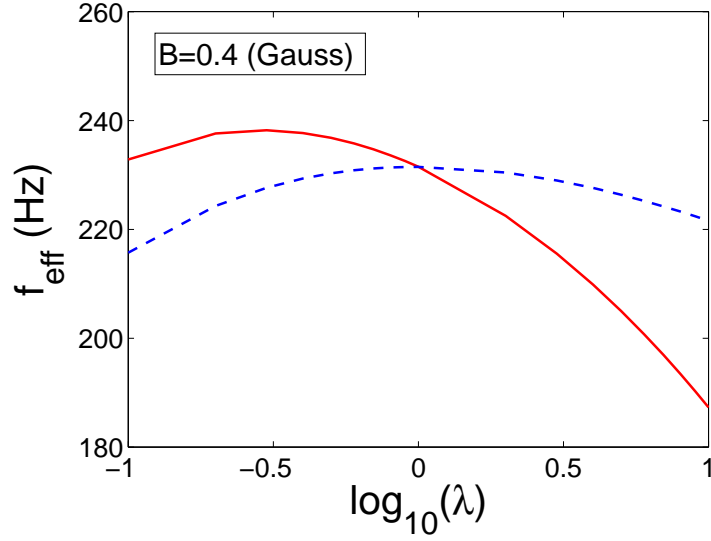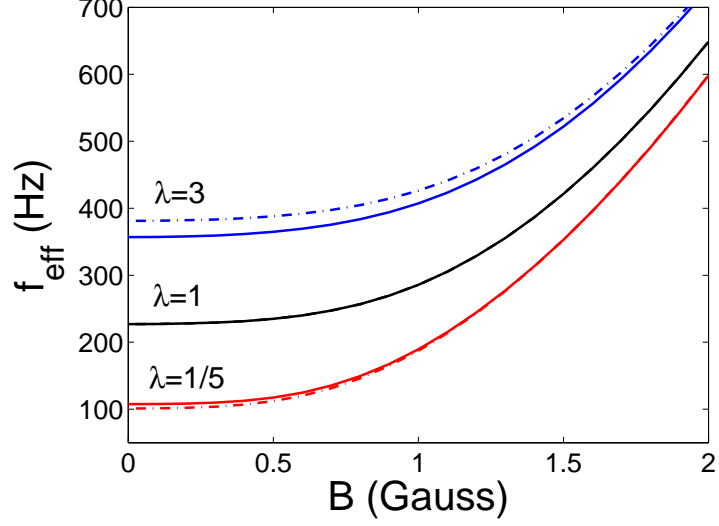
Figure 6.13: The B-field dependence of f_{eff} computed within the $\phi^{(v)}$ approximation. The solid lines include the dipolar interaction, while the dashed lines do not. The solid and dashed lines for $\lambda = 1$ are indistinguishable from the figure. Here we fix $\omega_\rho = (2\pi)41.1$ (kHz).

elements of the scattering potential H_s are given by

$$
\begin{aligned}
H_{s,11} &= \frac{1}{35}(7g_0 + 10g_2 + 18g_4)\delta^{(\text{reg})}(\vec{r}), \\
H_{s,22} &= \frac{1}{35}(14g_0 + 5g_2 + 16g_4)\delta^{(\text{reg})}(\vec{r}), \\
H_{s,33} &= \frac{1}{35}(14g_0 + 20g_2 + g_4)\delta^{(\text{reg})}(\vec{r}), \\
H_{s,12} &= H_{s,21} = \frac{\sqrt{2}}{35}(-7g_0 - 5g_2 + 12g_4)\delta^{(\text{reg})}(\vec{r}), \\
H_{s,13} &= H_{s,31} = \frac{\sqrt{2}}{35}(7g_0 - 10g_2 + 3g_4)\delta^{(\text{reg})}(\vec{r}), \\
H_{s,23} &= H_{s,32} = \frac{1}{35}(-14g_0 + 10g_2 + 4g_4)\delta^{(\text{reg})}(\vec{r}).
\end{aligned}
\tag{6.36}
$$

The matrix form of the spin dipolar term is

$$
\frac{c_d}{r^3}P_2(\cos\theta)\begin{pmatrix} 0 & 3\sqrt{2} & 0 \\ 3\sqrt{2} & 2 & 2 \\ 0 & 2 & 8 \end{pmatrix}.
\tag{6.37}
$$

To grasp the essential physics of the spin mixing dynamics in this three-level system, we first use the simplest harmonic ground state as the motional state for each spin state, and neglect the dipolar interaction in a spherical trap. Following the discussion of Ref. [64], the

interaction Hamiltonian in the same basis order is

$$H_s = \frac{\hbar}{2}\begin{pmatrix} 0 & \Omega_1 & 0 \\ \Omega_1 & 2\delta_1 & \Omega_2 \\ 0 & \Omega_2 & 2\delta_2 \end{pmatrix}, \tag{6.38}$$

assuming the direct coupling between $|0,0\rangle$ and $|2,-2\rangle$ can be ignored due to much larger detuning. δ_i and Ω_i are the detuning and coupling strength for each process respectively. To obtain the Rabi frequency, we need the eigenvalues of H_s, which can be determined straightforwardly from the equation

$$\lambda^3 - (\delta_1 + \delta_2)\lambda^2 + \left(\delta_1\delta_2 - \frac{\Omega_1^2}{4} - \frac{\Omega_2^2}{4}\right)\lambda + \frac{\Omega_1^2}{4}\delta_2 = 0. \tag{6.39}$$

The solutions are given by

$$\begin{aligned} \lambda^0 &= \frac{1}{3}\left(\delta_1 + \delta_2 + \tilde{\Omega}\cos\frac{\zeta}{3}\right), \\ \lambda^+ &= \frac{1}{3}\left(\delta_1 + \delta_2 + \tilde{\Omega}\cos\frac{2\pi - \zeta}{3}\right), \\ \lambda^- &= \frac{1}{3}\left(\delta_1 + \delta_2 + \tilde{\Omega}\cos\frac{2\pi + \zeta}{3}\right), \end{aligned} \tag{6.40}$$

where

$$\begin{aligned} \tilde{\Omega} &= \sqrt{3(\Omega_1^2 + \Omega_2^2) + 4(\delta_1^2 - \delta_1\delta_2 + \delta_2^2)}, \\ \zeta &= 2\pi - \arccos\left[\frac{1}{\tilde{\Omega}^3}[9(\Omega_1^2 + \Omega_2^2) - 4(2\delta_1 - \delta_2)(2\delta_2 - \delta_1)] - 27\Omega_1^2\delta_2\right]. \tag{6.41} \end{aligned}$$

Obviously, if the magnetic field is large enough ($\delta_2 \gg \delta_1$ due to the stronger Zeeman effect of $|2,-2\rangle$), the transitions from $|0,0\rangle$ and $|1,-1\rangle$ to $|2,-2\rangle$ will be greatly suppressed. In this case, the system dynamics behave like that of a two-level system, with the angular frequency

$$\lim_{\delta_2 \gg \delta_1}(\lambda^0 - \lambda^+) = \sqrt{\Omega_1^2 + \delta_1^2}. \tag{6.42}$$

Numerically, we estimate the B-field above which the system reduces to a two-level one is about 0.6 Gauss [62].

Including the dipolar interaction, we can address this problem more accurately by using the Gaussian ansatz for each spin state. We consider a more general cylindrical harmonic

trap. The corresponding eigenvalues are still denoted as $\tilde{\lambda}_i, i = 0, \pm$. The spin mixing frequency between spin states $|0,0\rangle$ and $|1,-1\rangle$ is then $f_{\text{eff}} = (\tilde{\lambda}_0 - \tilde{\lambda}_+)/(2\pi)$. The numerical results are shown in Fig. 6.14. We can see that the B-field dependence of f_{eff} obviously deviates from that of two-level system considered earlier in Fig. 6.7. We find the dipolar interaction becomes detectable in a pancake shape trap with $\lambda > 1$. For $\lambda = 3$, the dipolar interaction constitutes a maximal frequency difference around 25 Hz.
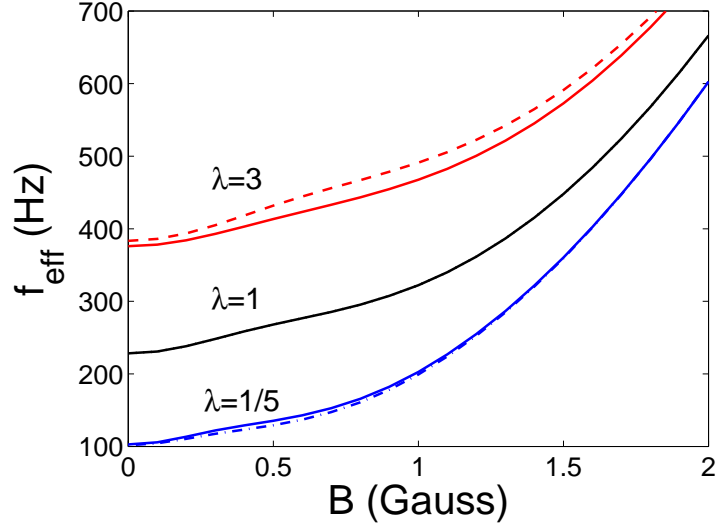
Figure 6.14: The spin mixing frequency between spin states $|0,0\rangle$ and $|1,-1\rangle$ in a cylindrical harmonic trap. We fix $\omega_\rho = (2\pi)41.1$ (kHz). The solid lines include the dipolar interaction, and the dashed lines do not.

We briefly summarize the effect of dipolar interaction in the $f = 1$ and $f = 2$ case. The dipolar interaction is normally stronger by a factor of two in magnitude along the direction of the dipoles (favored by the $\lambda < 1$ geometry) in comparison to the perpendicular direction (favored when $\lambda > 1$). Our results on the spin mixing frequency, however, reveal a completely opposite trend. We find relatively larger (smaller) dipolar effects for $\lambda > 1$ (< 1). This can be easily understood as follows. For the $f = 1$ case, the dipolar term H_{dd} is positive (negative) for $\lambda < 1$ (> 1), thus destructively (constructively) adding to the (negative) c_2 term in Eq. (6.9). For the $f = 2$ case, the same reasoning applies despite the opposite dipolar interaction in spin state $|-1,-1\rangle$. The dipolar effect becomes constructively enhanced for $\lambda > 1$ because the c_1 (corresponding to c_2 in $f = 1$) is positive in $f = 2$.

6.8   Conclusion

In conclusion, we have studied spin mixing between two ^{87}Rb atoms trapped in a single optical lattice site. The mixing dynamics of different spin states come from the s-wave interaction between the two atoms. Thus, the spin mixing frequency depends on the motional wave function of each spin state. We have shown the dependence of spin mixing frequency on various approximations of the motional states. We find that in a spherical harmonic trap, the motional state approximated as the trap ground state causes an error of about 7% of the most accurate theoretical estimate of the spin mixing frequency. The scattering length difference, which is used to identify the magnetic ground state of the system, can be extracted from the spin mixing frequency measurements. The experiments have confirmed that $f = 1$ ^{87}Rb atom is ferromagnetic. The $f = 2$ ^{87}Rb atom favors antiferromagnetic phase. However, the error bar touches the boundary between the antiferromagnetic and cyclic phase, which calls for more precise measurements to unambiguously determine the magnetic ground state of the $f = 2$ ^{87}Rb atomic system. For a more complete description, we have also included the spin dipolar interaction. While the effects of the dipolar interaction is typically small, and can be ignored completely for spherical harmonic traps, our calculations show that they become observable inside cylindrical harmonic traps, especially for oblate shaped traps in the limit of $\lambda > 3$. This is due to the fact that the spin exchange interaction c_2 is extremely small for ^{87}Rb atom, thus making the spin dipole induced dynamics relatively strong in comparison. Our theoretical studies suggest a new way to observe the dipolar effect in atomic systems. We hope this study will stimulate experimental efforts aimed at observing interesting dipolar effects in spin mixing.

APPENDIX A

EXPANDING THE WAVE FUNCTION OF CM AND RELATIVE MOTIONS TO SINGLE PARTICLE BASIS STATES IN 1D AND 3D HARMONIC TRAPS

First we consider the two-boson solution inside a 1D harmonic trap, we note that

$$
N \sum_{pq} \frac{1 + (-1)^{p+q}}{2} \frac{(-1)^{(p-q)/2} \Gamma(\frac{p+q+1}{2})}{(2\nu_e - p - q)\sqrt{p!q!}} \phi_p(x_1)\phi_q(x_2)
$$

$$
= \sum_{pq} \frac{1 + (-1)^{p+q}}{2} \frac{(-1)^{(p-q)/2} \Gamma(\frac{p+q+1}{2})}{(2\nu_e - p - q)\sqrt{p!q!}} \frac{e^{-x_1^2/2}}{\sqrt{2^p p!\sqrt{\pi}}} H_p(x_1) \frac{e^{-x_2^2/2}}{\sqrt{2^q q!\sqrt{\pi}}} H_q(x_2)
$$

$$
= \frac{N}{\sqrt{\pi}} \sum_{Kq} \frac{(-1)^K (-1)^q \Gamma(K + \frac{1}{2})}{(2\nu_e - 2K) 2^K (2K - q)! q!} e^{-x_1^2/2} H_{2K-q}(x_1) e^{-x_2^2/2} H_q(x_2)
$$

$$
= e^{-x_1^2/2} e^{-x_2^2/2} \frac{N}{\sqrt{\pi}} \sum_K \frac{(-1)^K \Gamma(K + \frac{1}{2})}{(2\nu_e - 2K) 2^K (2K)!} \sum_q \frac{(-1)^q (2K)!}{(2K - q)! q!} H_{2K-q}(x_1) H_q(x_2)
$$

$$
= e^{-X^2/2} e^{-x^2/2} \frac{N}{\sqrt{\pi}} \sum_K \frac{(-1)^K \Gamma(K + \frac{1}{2})}{(2\nu_e - 2K) 2^K (2K)!} 2^K H_{2K}\left(\frac{x_1 - x_2}{\sqrt{2}}\right)
$$

$$
= e^{-X^2/2} e^{-x^2/2} \frac{N}{\sqrt{\pi}} \sum_K \frac{(-1)^K \Gamma(K + \frac{1}{2})}{(2\nu_e - 2K)} \frac{\sqrt{\pi}}{2^{2K} \Gamma(K + \frac{1}{2}) K!} (-1)^K 2^{2K} K! L_K^{(-1/2)}(x^2)
$$

$$
= -e^{-X^2/2} e^{-x^2/2} \frac{N}{2} \sum_K \frac{1}{K - \nu_e} L_K^{(-1/2)}(x^2)
$$

$$
= -e^{-X^2/2} e^{-x^2/2} \frac{N}{2} \sum_K \int_0^{+\infty} \frac{dy}{(1+y)^2} \left(\frac{y}{1+y}\right)^{K-\nu_e-1} L_K^{(-1/2)}(x^2)
$$

$$
= -e^{-X^2/2} e^{-x^2/2} \frac{N}{2} \int_0^{+\infty} \frac{dy}{(1+y)^2} \left(\frac{y}{1+y}\right)^{-\nu_e-1} \sum_K L_K^{(-1/2)}(x^2) \left(\frac{y}{1+y}\right)^K
$$

$$
= -e^{-X^2/2} e^{-x^2/2} \frac{N}{2} \int_0^{+\infty} \frac{dy}{(1+y)^2} \left(\frac{y}{1+y}\right)^{-\nu_e-1} e^{-x^2 y} (1+y)^{1/2}
$$

$$
= -e^{-X^2/2} e^{-x^2/2} \frac{N}{2} \int_0^{+\infty} e^{-x^2 y} y^{-\nu_e-1} (1+y)^{\nu_e-1/2} dy
$$

$$
= -e^{-X^2/2} e^{-x^2/2} \frac{N}{2} \Gamma(-\nu_e) U\left(-\nu_e, \frac{1}{2}; x^2\right)
$$

$$
= -\frac{N}{2} \pi^{1/4} \phi_0(X) \frac{\sqrt{\pi}}{A_e} \psi_{\nu_e}(x). \tag{A.1}
$$

Thus if we choose $N = -2\pi^{-3/4}A_e$, we recover the decomposition

$$\phi_0(X)\psi_{\nu_e}(x) = -2\pi^{-3/4}\left(\frac{\Gamma(-\nu_e + \frac{1}{2})}{\Gamma(-\nu_e)}\frac{1}{\mathcal{F}(-\nu_e + \frac{1}{2}) - \mathcal{F}(-\nu_e)}\right)^{\frac{1}{2}}$$
$$\sum_{pq}\frac{1 + (-1)^{p+q}}{2}\frac{(-1)^{(p-q)/2}\Gamma(\frac{p+q+1}{2})}{(2\nu_e - p - q)\sqrt{p!q!}}\phi_p(x_1)\phi_q(x_2). \qquad (A.2)$$

Similarly, we have the decomposition for two fermions,

$$\phi_0(X)\psi_{\nu_o}(x) = -2\pi^{-3/4}\left(\frac{\Gamma(-\nu_o - 1/2)}{\Gamma(-\nu_o)}\frac{1}{\mathcal{F}(-\nu_o) - \mathcal{F}(-\nu_o - 1/2)}\right)^{\frac{1}{2}}$$
$$\sum_{pq}\frac{1 - (-1)^{p+q}}{2}\frac{(-1)^{(p-q-1)/2}\Gamma(\frac{p+q+2}{2})}{(2\nu_o + 1 - p - q)\sqrt{p!q!}}\phi_p(x_1)\phi_q(x_2). \qquad (A.3)$$

Next we consider a 3D cylindrical harmonic trap with $\lambda = \omega_z/\omega_\perp$. The decomposition can be realized using the same technique with the result given by

$$\phi_{\mathbf{0}}(\vec{R})\psi_\nu(\vec{r}) = N\sum_{\mathbf{mn}}\frac{1}{2\nu - \sum_{j=x,y}(m_j + n_j) - \lambda(m_z + n_z)}$$
$$\left[\prod_{j=x,y,z}\frac{1 + (-1)^{m_j+n_j}}{2}\frac{(-1)^{\frac{m_j-n_j}{2}}}{\sqrt{m_j!n_j!}}\Gamma\left(\frac{m_j + n_j + 1}{2}\right)\right]\phi_{\mathbf{m}}(\vec{r}_1)\phi_{\mathbf{n}}(\vec{r}_2), \quad (A.4)$$

where the total energy is $E = 2\nu + 2 + \lambda$, including both the CM and relative motion. The normalization constant N is given by

$$N = \frac{2}{\pi^{5/4}}\frac{1}{\sqrt{\sum_{p=0}^{\infty}\zeta(2, \lambda p - \nu)\Gamma(p + 1/2)/p!}}, \qquad (A.5)$$

here $\zeta(s, x) = \sum_{k=0}^{\infty}1/(k + x)^s$. The length and energy scale are $\sqrt{\hbar/(m\omega_\perp)}$ and $\hbar\omega_\perp$ respectively.

APPENDIX B

EXPRESSING A 3D SCHMIDT DECOMPOSITION OF TWO ATOMS INTO A 1D DECOMPOSITION

In the single particle basis, the motional wave function is given by

$$
\begin{aligned}
|\Psi\rangle \;=\; & N \sum_{\mathbf{m},\mathbf{n}} \frac{1}{2x - \sum_{j=x,y}(m_j + n_j) - \lambda(m_z + n_z)} \\
& \prod_{j=x,y,z} \frac{1 + (-1)^{m_j+n_j}}{2} \frac{(-1)^{\frac{m_j-n_j}{2}}}{\sqrt{m_j! n_j!}} \Gamma\left(\frac{m_j + n_j + 1}{2}\right) |\mathbf{m}\rangle_1 |\mathbf{n}\rangle_2, \quad\quad \text{(B.1)}
\end{aligned}
$$

where N is the normalization constant as given before. Finding the Schmidt decomposition for such 3D system generally requires large amount of memory. For example, at a cutoff level of 30 in all three directions, we need to deal with a 27000×27000 matrix, which is really a demanding computational task. So we try an alternative method as shown below. We rewrite the wave function as

$$
\begin{aligned}
|\Psi\rangle \;=\; & -N \sum_{\mathbf{m},\mathbf{n}} \int_0^\infty \frac{dy}{(1+y)^2} \left(\frac{y}{1+y}\right)^{-2x-1} \left(\frac{y}{1+y}\right)^{\sum_{j=x,y}(m_j+n_j)+\lambda(m_z+n_z)} \\
& \prod_{j=x,y,z} \frac{1 + (-1)^{m_j+n_j}}{2} \frac{(-1)^{\frac{m_j-n_j}{2}}}{\sqrt{m_j! n_j!}} \Gamma\left(\frac{m_j + n_j + 1}{2}\right) |\mathbf{m}\rangle_1 |\mathbf{n}\rangle_2 \\
\;=\; & -N \int_0^\infty \frac{dy}{(1+y)^2} \left(\frac{y}{1+y}\right)^{-2x-1} \sum_{\mathbf{m},\mathbf{n}} \left(\frac{y}{1+y}\right)^{\sum_{j=x,y}(m_j+n_j)+\lambda(m_z+n_z)} \\
& \prod_{j=x,y,z} \frac{1 + (-1)^{m_j+n_j}}{2} \frac{(-1)^{\frac{m_j-n_j}{2}}}{\sqrt{m_j! n_j!}} \Gamma\left(\frac{m_j + n_j + 1}{2}\right) |\mathbf{m}\rangle_1 |\mathbf{n}\rangle_2, \quad\quad \text{(B.2)}
\end{aligned}
$$

which facilitates the Schmidt decomposition for $j = x, y$, respectively according to

$$
\begin{aligned}
& \sum_{m_j,n_j} \left(\frac{y}{1+y}\right)^{m_j+n_j} \frac{1 + (-1)^{m_j+n_j}}{2} \frac{(-1)^{\frac{m_j-n_j}{2}}}{\sqrt{m_j! n_j!}} \Gamma\left(\frac{m_j + n_j + 1}{2}\right) |m_j\rangle_1 |n_j\rangle_2 \\
\;=\; & \sum_{s_j} \mu_{s_j} |\tilde{\phi}_{s_j}\rangle_1 |\tilde{\phi}_{s_j}\rangle_2, \quad\quad \text{(B.3)}
\end{aligned}
$$

and similarly for $j = z$,

$$\sum_{m_j, n_j} \left(\frac{y}{1+y}\right)^{\lambda(m_j+n_j)} \frac{1+(-1)^{m_j+n_j}}{2} \frac{(-1)^{\frac{m_j-n_j}{2}}}{\sqrt{m_j! n_j!}} \Gamma\left(\frac{m_j+n_j+1}{2}\right) |m_j\rangle_1 |n_j\rangle_2$$

$$= \sum_{s_j} \mu'_{s_j} |\tilde{\phi}'_{s_j}\rangle_1 |\tilde{\phi}'_{s_j}\rangle_2. \tag{B.4}$$

We assume that both μ_{s_j} and μ'_{s_j} real. $|\tilde{\phi}_{s_j}\rangle$ and $|\tilde{\phi}'_{s_j}\rangle$ then correspond to the natural orbitals of the Schmidt decomposition. Thus,

$$|\Psi\rangle = -N \int_0^\infty \frac{dy}{(1+y)^2} \left(\frac{y}{1+y}\right)^{-2x-1} \sum_{\mathbf{s}} \mu_{\mathbf{s}} |\phi_{\mathbf{s}}\rangle_1 |\phi_{\mathbf{s}}\rangle_2$$

$$= \sum_{\mathbf{s}} \kappa_{\mathbf{s}} |\phi_{\mathbf{s}}\rangle_1 |\phi_{\mathbf{s}}\rangle_2, \tag{B.5}$$

here $\mu_{\mathbf{s}} = \mu_{s_x} \mu_{s_y} \mu'_{s_z}$ and $|\phi_{\mathbf{s}}\rangle_j = |\tilde{\phi}_{s_x}, \tilde{\phi}_{s_y}, \tilde{\phi}'_{s_z}\rangle_j$. The Schmidt coefficients are given by

$$\kappa_{\mathbf{s}} = -N \int_0^\infty \frac{dy}{(1+y)^2} \left(\frac{y}{1+y}\right)^{-2x-1} \mu_{\mathbf{s}}. \tag{B.6}$$

The original 3D diagonalization is now reduced to three 1D diagonalizations, which are much easier to deal with. The price we pay is an extra integration over variable y. This can be done with high precision using the Simpson's 3/8 Rule.

REFERENCES

[1] A. Einstein, B. Podolsky, and N. Rosen, Phys. Rev. **47**, 777 (1935).

[2] J. S. Bell, Physics **1**, 195 (1964).

[3] A. Ekert and R. Jozsa, Philos. Trans. R. Soc. London, Ser. A **356**, 1769 (1998).

[4] S. L. Braunstein, C. M. Caves, R. Jozsa, N. Linden, S. Popescu, and R. Schack, Phys. Rev. Lett. **83**, 1054 (1999).

[5] B. Schumacher, Phys. Rev. A **51**, 2738 (1995).

[6] C. H. Bennett, Phys. Today **24** (1995).

[7] A. K. Ekert, Phys. Rev. Lett. **67**, 661 (1991).

[8] C. H. Bennett, G. Brassard, C. Crépeau, R. Jozsa, A. Peres, and W. K. Wootters, Phys. Rev. Lett. **70**, 1895 (1993).

[9] D. Bouwmeester, Jian-Wei Pan, K. Mattle, M. Eibl, H. Weinfurter, and A. Zeilinger, Nature **390**, 575 (1997).

[10] D. Boschi, S. Branca, F. De Martini, L. Hardy, and S. Popescu, Phys. Rev. Lett. **80**, 1121 (1998).

[11] A. Furusawa, J. L. Sørensen, S. L. Braunstein, C. A. Fuchs, H. J. Kimble, and E. S. Polzik, Science **282**, 706 (1998).

[12] M. Murao, M. B. Plenio, and V. Vedral, Phys. Rev. A **61**, 032311 (2000).

[13] P. W. Shor, in *Proc. 35th Annual Symposium on the Foundations of Computer Science*, edited by S. Goldwasser (IEEE Computer Society Press, Los Alamitos, California, 1994), p. 124.

[14] L. Henderson and V. Vedral, J. Phys. A: Math. Gen. **34**, 6899 (2001).

[15] V. Vedral and M. B. Plenio, Phys. Rev. A **57**, 1619 (1998).

[16] D. Bruß, J. Math. Phys. **43**, 4237 (2002).

[17] R. F. Werner, Phys. Rev. A **40**, 4277 (1989).

[18] M. A. Nielsen and I. S. Chuang, *Quantum Computation and Quantum Information*, (Cambridge University Press, 2000).

[19] R. Paškauskas and L. You, Phys. Rev. A **64**, 042310 (2001).

[20] L. Gurvits, in *Proc. 35th ACM Symposium on Theory of Computing*, (ACM Press, New York, 2003), p. 10.

[21] C. H. Bennett, D. P. DiVincenzo, J. A. Smolin, and W. K. Wootters, Phys. Rev. A **54**, 3824 (1996).

[22] G. Vidal and R. F. Werner, Phys. Rev. A **65**, 032314 (2002).

[23] A. Peres, Phys. Rev. Lett. **77**, 1413 (1996).

[24] M. Horodecki, P. Horodecki, and R. Horodecki, Phys. Lett. A **232**, 333 (1997).

[25] A. Aspect, J. Dalibard, and G. Roger, Phys. Rev. Lett. **49**, 1804 (1982).

[26] Z. Y. Ou and L. Mandel, Phys. Rev. Lett. **61**, 50 (1988).

[27] Y. H. Shih and C. O. Alley, Phys. Rev. Lett. **61**, 2921 (1988).

[28] P. G. Kwiat, K. Mattle, H. Weinfurter, A. Zeilinger, A. V. Sergienko, and Y. Shih, Phys. Rev. Lett. **75**, 4337 (1995).

[29] D. Bouwmeester, Jian-Wei Pan, M. Daniell, H. Weinfurter, and A. Zeilinger, Phys. Rev. Lett. **82**, 1345 (1999).

[30] M. Eibl, S. Gaertner, M. Bourennane, C. Kurtsiefer, M. Żukowski, and H. Weinfurter, Phys. Rev. Lett. **90**, 200403 (2003).

[31] M. W. Mitchell, J. S. Lundeen, and A. M. Steinberg, Nature **429**, 161 (2004).

[32] J. I. Cirac and P. Zoller, Phys. Rev. A **50**, R2799 (1994).

[33] S. J. D. Phoenix and S. M. Barnett, J. Mod. Opt. **40**, 979 (1993).

[34] S. J. van Enk, J. I. Cirac, and P. Zoller, Phys. Rev. Lett. **79**, 5178 (1997).

[35] C. Cabrillo, J. I. Cirac, P. Garcia-Fernandez, and P. Zoller, Phys. Rev. A **59**, 1025 (1999).

[36] Q. A. Turchette, C. S. Wood, B. E. King, C. J. Myatt, D. Leibfried, W. M. Itano, C. Monroe, and D. J. Wineland, Phys. Rev. Lett. **81**, 3631 (1998).

[37] C. F. Roos, M. Riebe, H. Häffner, W. Hänsel, J. Benhelm, G. P. T. Lancaster, C. Becher, F. Schmidt-Kaler, and R. Blatt, Science **304**, 1478 (2004).

[38] C. A. Sackett, D. Kielpinski, B. E. King, C. Langer, V. Meyer, C. J. Myatt, M. Rowe, Q. A. Turchette, W. M. Itano, D. J. Wineland, and C. I. Monroe, Nature **404**, 256 (2000).

[39] D. Leibfried, E. Knill, S. Seidelin, J. Britton, R. B. Blakestad, J. Chiaverini, D. B. Hume, W. M. Itano, J. D. Jost, C. Langer, R. Ozeri, R. Reichle, and D. J. Wineland, Nature **438**, 639 (2005).

[40] K. Mølmer and A. Sørensen, Phys. Rev. Lett. **82**, 1835 (1999).

[41] T. Busch, B. G. Englert, K. Rzazewski, and M. Wilkens, Found. Phys. **28**, 549 (1998).

[42] Z. Idziaszek and T. Calarco, Phys. Rev. A **71**, 050701(R) (2005).

[43] K. I. Petsas, A. B. Coates, and G. Grynberg, Phys. Rev. A **50**, 5173 (1994).

[44] M. Raizen, C. Salomon, and Q. Niu, Phys. Today **50**, 30 (1997).

[45] G. Raithel, G. Birkl, A. Kastberg, W. D. Phillips, and S. L. Rolston, Phys. Rev. Lett. **78**, 630 (1997).

[46] T. Müller-Seydlitz, M. Hartl, B. Brezger, H. Hänsel, C. Keller, A. Schnetz, R. J. C. Spreeuw, T. Pfau, and J. Mlynek. Phys. Rev. Lett. **78**, 1038 (1997).

[47] L. Guidoni, C. Triché, P. Verkerk, and G. Grynberg, Phys. Rev. Lett. **79**, 3363 (1997).

[48] S. Friebel, C. D'Andrea, J. Walz, M. Weitz, and T. W. Hänsch, Phys. Rev. A **57**, R20 (1998).

[49] L. Guidoni and P. Verkerk, Phys. Rev. A **57**, R1501 (1998).

[50] I. H. Deutsch and P. S. Jessen, Phys. Rev. A **57**, 1972 (1998).

[51] S. E. Hamann, D. L. Haycock, G. Klose, P. H. Pax, I. H. Deutsch, and P. S. Jessen, Phys. Rev. Lett. **80**, 4149 (1998).

[52] M. Greiner, O. Mandel, T. Esslinger, T. W. Hansch, and I. Bloch, Nature **415**, 39 (2002).

[53] S. Tsuchiya, S. Kurihara, and T. Kimura, Phys. Rev. A **70**, 043628 2004.

[54] T. Stöferle, H. Moritz, C. Schori, M. Köhl, and T. Esslinger, Phys. Rev. Lett. **92**, 130403 (2004).

[55] K. Sengupta and N. Dupuis, Europhys. Lett. **70**, 586 (2005).

[56] M. Köhl, H. Moritz, T. Stöferle, K. Günter, and T. Esslinger, Phys. Rev. Lett. **94**, 080403 (2005).

[57] T. Stöferle, H. Moritz, K. Güter, M. Köhl, and T. Esslinger, Phys. Rev. Lett. **96**, 030401 (2006).

[58] R. B. Diener and Tin-Lun Ho, Phys. Rev. Lett. **96**, 010402 (2006).

[59] J. Wang, C. K. Law, and M. C. Chu, Phys. Rev. A **72**, 022346 (2005).

[60] M.-S. Chang, Q. Qin, W. Zhang, L. You, and M. S. Chapman, Nature Phys. **1**, 111 (2005).

[61] J. Kronjäger, C. Becker, M. Brinkmann, R. Walser, P. Navez, K. Bongs, and K. Sengstock, Phys. Rev. A **72**, 063619 (2006).

[62] A. Widera, F. Gerbier, S. Fölling, T. Gericke, O. Mandel, and I. Bloch, Phys. Rev. Lett. **95**, 190405 (2005).

[63] F. Gerbier, A. Widera, S. Fölling, O. Mandel, and I. Bloch, Phys. Rev. A **73**, 041602(R) (2006).

[64] A. Widera, F. Gerbier, S. Fölling, T. Gericke, O. Mandel, and I. Bloch, cond-mat/0604038.

[65] L. Santos, G. V. Shlyapnikov, P. Zoller, and M. Lewenstein, Phys. Rev. Lett. **85**, 1791 (2000).

[66] S. Giovanazzi, A. Görlitz, and T. Pfau, Phys. Rev. Lett. **89**, 130401 (2002).

[67] B. Damski, L. Santos, E. Tiemann, M. Lewenstein, S. Kotochigova, P. Julienne, and P. Zoller, Phys. Rev. Lett. **90**, 110401 (2003).

[68] S. Yi and L. You, Phys. Rev. A **67**, 045601 (2003).

[69] S. Yi and L. You, Phys. Rev. Lett. **92**, 193201 (2004).

[70] S. Yi, L. You, and H. Pu, Phys. Rev. Lett. **93**, 040403 (2004).

[71] C. Eberlein, S. Giovanazzi, and D. H. J. O'Dell, Phys. Rev. A **71**, 033618 (2005).

[72] K. Nho and D. P. Landau, Phys. Rev. A **72**, 023615 (2005).

[73] M. A. Baranov, K. Osterloh, and M. Lewenstein, Phys. Rev. Lett. **94**, 070404 (2005).

[74] J. Stuhler, A. Griesmaier, T. Koch, M. Fattori, T. Pfau, S. Giovanazzi, P. Pedri, and L. Santos, Phys. Rev. Lett. **95**, 150406 (2005).

[75] S. Yi and H. Pu, Phys. Rev. A **73**, 023602 (2006).

[76] Y. Kawaguchi, H. Saito, and M. Ueda, Phys. Rev. Lett. **96**, 080405 (2006).

[77] A. Griesmaier, J. Werner, S. Hensler, J. Stuhler, and T. Pfau, Phys. Rev. Lett. **94**, 160401 (2005).

[78] S. Haroche and J. M. Raimond, *Cavity Quantum Electrodynamics*, edited by P. R. Berman, (Academic Press, Inc., USA, 1994).

[79] E. T. Jaynes and F. W. Cummings, Proc. IEEE **51**, 89 (1963).

[80] C. Cohen-Tannoudji, J. Dupont-Roc, and G. Grynberg, *Atom-Photon Interactions*, (John Wiley & Sons, Inc., USA, 1992).

[81] D. F. Walls and G. J. Milburn, *Quantum Optics*, (Springer-Verlag, 1994).

[82] C. K. Law and J. Kimble, J. Mod. Opt. **44**, 2067 (1997).

[83] J. Eberly and C. K. Law, Acta Physica Polonica A **93**, 55 (1998).

[84] J. Kim, O. Benson, H. Kan, and Y. Yamamoto, Nature (London) **397**, 500 (1999).

[85] C. Brunel, B. Lounis, P. Tamarat, and M. Orrit, Phys. Rev. Lett. **83**, 2722 (1999).

[86] C. Santori, M. Pelton, G. Solomon, Y. Dale, and Y. Yamamoto, Phys. Rev. Lett. **86**, 1502 (2001).

[87] A. Kuhn, M. Hennrich, T. Bondo, and G. Rempe, Appl. Phys. B **69**, 373 (1999).

[88] Hyunchul Nha, Young-Tak Chough, and Kyungwon An, Phys. Rev. A **63**, 010301 (2001).

[89] M. B. Plenio and P. Knight, Rev. Mod. Phys. **70**, 101 (1998).

[90] S. J. van Enk, J. I. Cirac, and P. Zoller, Phys. Rev. Lett. **78**, 4293 (1997).

[91] S. J. van Enk, J. I. Cirac, and P. Zoller, Science **279**, 205 (1998).

[92] G. P. Guo and G. C. Guo, Phys. Lett. A **320**, 140 (2003).

[93] X. X. Yi, X. H. Su, and L. You, Phys. Rev. Lett. **90**, 097902 (2003).

[94] H. Häffner, S. Gulde, M. Riebe, G. Lancaster, C. Becher, J. Eschner, F. Schmidt-Kaler, and R. Blatt, Phys. Rev. Lett. **90**, 143602 (2003).

[95] T. Pellizzari, S. A. Gardiner, J. I. Cirac, and P. Zoller, Phys. Rev. Lett. **75**, 3788 (1995).

[96] A. M. Steane and D. M. Lucas, Fortschr. Phys. **48**, 839 (2000).

[97] H. Mabuchi, Q. A. Turchette, M. S. Chapman, and H. J. Kimble, Opt. Lett. **21**, 1393 (1996).

[98] C. J. Hood, M. S. Chapman, T. W. Lynn, and H. J. Kimble, Phys. Rev. Lett. **80**, 4157 (1998).

[99] J. McKeever, J. R. Buck, A. D. Boozer, A. Kuzmich, H.- C. Nägerl, D. M. Stamper-Kurn, and H. J. Kimble, Phys. Rev. Lett. **90**, 133602 (2003).

[100] P. W. H. Pinkse, T. Fischer, P. Maunz, and G. Rempe, Nature **404**, 365 (2000).

[101] M. Hennrich, T. Legero, A. Kuhn, and G. Rempe, Phys. Rev. Lett. **85**, 4872 (2000).

[102] A. D. Boozer, A. Boca, R. Miller, T. E. Northup, and H. J. Kimble, quant-ph/0606104.

[103] P. Maunz, T. Puppe, I. Schuster, N. Syassen, P. W. H. Pinkse, and G. Rempe, Phys. Rev. Lett. **94**, 033002 (2005).

[104] X. Maître, E. Hagley, G. Nogues, C. Wunderlich, P. Goy, M. Brune, J. M. Raimond, and S. Haroche, Phys. Rev. Lett. **79**, 769 (1997).

[105] W. Lange and H. J. Kimble, Phys. Rev. A **61**, 063817 (2000).

[106] A. S. Parkins, P. Marte, P. Zoller, and H. J. Kimble, Phys. Rev. Lett. **71**, 3095 (1993).

[107] C. Monroe, D. M. Meekhof, B. E. King, S. R. Jefferts, W. M. Itano, and D. J. Wineland, Phys. Rev. Lett. **75**, 4011 (1995).

[108] F. Diedrich, J. C. Bergquist, W. M. Itano, and D. J. Wineland, Phys. Rev. Lett. **62**, 403 (1989).

[109] L. You, Phys. Rev. A **64**, 012302 (2001).

[110] T. A. B. Kennedy and P. Zhou, Phys. Rev. A **64**, 063805 (2001).

[111] L.-M. Duan, A. Kuzmich, and H. J. Kimble, Phys. Rev. A **67**, 032305 (2003).

[112] P. Zhang, Y. Li, C. P. Sun, and L. You, Phys. Rev. A **70**, 063804 (2004) .

[113] E. Knill, R. Laflamme, and G. J. Milburn, Nature(London) **409**, 46 (2001).

[114] T. B. Pittman, B. C. Jacobs, and J. D. Franson, Phys. Rev. Lett. **88**, 257902 (2002).

[115] T. B. Pittman, B. C. Jacobs, and J. D. Franson, Johns Hopkins APL Technical Digest **25**, 84 (2004).

[116] A. Rauschenbeutel, P. Bertet, S. Osnaghi, G. Nogues, M. Brune, J. M. Raimond, and S. Haroche, Phys. Rev. A **64**, 050301(R) (2001).

[117] D. E. Browne and M. B. Plenio, Phys. Rev. A **67**, 012325 (2003).

[118] C. Marr, A. Beige, and G. Rempe, Phys. Rev. A **68**, 033817 (2003).

[119] K. Bergmann, H. Theuer, and B. W. Shore, Rev. Mod. Phys. **70**, 1003 (1998).

[120] B. Sun, M. S. Chapman, and L. You, Phys. Rev. A **69**, 042316 (2004).

[121] L.-M. Duan, A. Kuzmich, and H. J. Kimble, Phys. Rev. A **67**, 032305 (2003).

[122] A. Kuzmich, W. P. Bowen, A. D. Boozer, A. Boca, C. W. Chou, L.-M. Duan, and H. J. Kimble, Nature **423**, 731 (2003).

[123] C. Simon and Jean-Philippe Poizat, Phys. Rev. Lett. **94**, 030502 (2005).

[124] P. Grangier, G. Reymond, and N. Schlosser, Fortschr. Phys. **48**, 859 (2000).

[125] S. Kuhr, W. Alt, D. Schrader, M. Muller, V. Gomer, and D. Meschede, Science **293**, 278(2001).

[126] C. W. Gardiner and P. Zoller, *Quantum Noise*, (Springer-Verlag, 2000).

[127] H. Carmichael, *An Open Systems Approach to Quantum Optics*, (Springer-Verlag, 1993).

[128] C. K. Law and J. H. Eberly, Phys. Rev. Lett. **92**, 127903 (2004).

[129] D. L. Zhou, B. Sun, C. P. Sun, and L. You, Phys. Rev. A **72**, 040302 (2005).

[130] K. Huang and C. N. Yang, Phys. Rev. **105**, 767 (1957).

[131] C. J. Pethick and H. Smith, *Bose-Einstein Condensation in Dilute Gases*, Cambridge University Press, 2002.

[132] M. Olshanii, Phys. Rev. Lett. **81**, 938 (1998).

[133] D. Blume and C. H. Greene, Phys. Rev. A **65**, 043613 (2002).

[134] E. L. Bolda, E. Tiesinga, and P. S. Julienne, Phys. Rev. A **66**, 013403 (2002).

[135] K. Kanjilal and D. Blume, Phys. Rev. A **70**, 042709 (2004).

[136] B. E. Granger and D. Blume, Phys. Rev. Lett. **92**, 133202 (2004).

[137] M. D. Girardeau and M. Olshanii, Phys. Rev. A **70**, 023608 (2004).

[138] K. Wódkiewicz, Phys. Rev. A **43**, 68 (1991).

[139] G. Arfken, *Mathematical Methods for Physicists*, 3rd Ed., (Academic Press, Inc., 1987).

[140] E. Merzbacher, *Quantum Mechanics*, 3rd Ed., (John Wiley & Sons, Inc., 1998).

[141] Tzu-Chieh Wei and P. M. Goldbart, Phys. Rev. A **68**, 042307 (2003).

[142] S. J. van Enk and O. Hirota, Phys. Rev. A **71**, 062322 (2005).

[143] T. Yu and J. H. Eberly, Phys. Rev. B **68**, 165322 (2003).

[144] T. Yu and J. H. Eberly, Phys. Rev. Lett. **93**, 140404 (2004).

[145] L. Tonks, Phys. Rev. **50**, 955 (1936).

[146] M. D. Girardeau, J. Math. Phys. **1**, 516 (1960).

[147] B. Paredes, A. Widera, V. Murg, O. Mandel, S. Fölling, I. Cirac, G. V. Shlyapnikov, T. W. Hänsch and I. Bloch, Nature **429**, 277 (2004).

[148] M. D. Girardeau and M. Olshanii, cond-mat/0309396.

[149] M. D. Girardeau, H. Nguyen, and M. Olshanii, Opt. Commun. **243**, 3 (2004).

[150] M. G. Moore, T. Bergeman, and M. Olshanii, J. de Phys. IV **116**, 69 (2004).

[151] A. Lupu-Sax, *Quantum Scattering Theory and Applications*, Ph.D. Thesis, (Harvard University, 1998).

[152] D. J. Heinzen, R. Wynar, P. D. Drummond, and K. V. Kheruntsyan, Phys. Rev. Lett. **84**, 5029 (2000).

[153] M. G. Moore, Phys. Rev. Lett. **96**, 100401 (2006).

[154] L. M. Jensen, H. M. Nilsen, and Gentaro Watanabe, cond-mat/0604149.

[155] M. Kohl, K. Gunter, T. Stoferle, H. Moritz, and T. Esslinger, J. Phy. B **39**, S47 (2006).

[156] R. B. Diener and Tin-Lun Ho, cond-mat/0405174.

[157] Tin-Lun Ho, Phys. Rev. Lett. **81**, 742 (1998).

[158] T. Ohmi and K. Machida, J. Phys. Soc. Jpn. **67**, 1822 (1998).

[159] C. K. Law, H. Pu, and N. P. Bigelow, Phys. Rev. Lett. **81**, 5257 (1998).

[160] D. S. Hall, M. R. Matthews, C. E. Wieman, and E. A. Cornell, Phys. Rev. Lett. **81**, 1543 (1998).

[161] D. Jaksch, C. Bruder, J. I. Cirac, C. W. Gardiner, and P. Zoller, Phys. Rev. Lett. **81**, 3108 (1998).

[162] B. Sun, W. X. Zhang, S. Yi, M. S. Chapman, and L. You, Phys. Rev. Lett. **97**, 123201 (2006).

[163] S. Yi and L. You, Phys. Rev. A **61**, 041604(R) (2000).

[164] S. Yi and L. You, Phys. Rev. A **63**, 053607 (2001).

[165] D. C. E. Bortolotti, S. Ronen, J. L. Bohn, and D. Blume, cond-mat/0604432.

[166] J. P. Burke, Jr. and J. L. Bohn, Phys. Rev. A **59**, 1303 (1999).

[167] N. N. Klausen, J. L. Bohn, and C. H. Greene, Phys. Rev. A **64**, 053602 (2001).

[168] E. G. M. van Kempen, S. J. J. M. F. Kokkelmans, D. J. Heinzen, and B. J. Verhaar, Phys. Rev. Lett. **88**, 093201 (2002).

[169] A. Derevianko, Phys. Rev. A **67**, 033607 (2003); Phys. Rev. A **72**, 039901(E) (2005).

[170] Z. Pavlović, R. V. Krems, R. Côté, and H. R. Sadeghpour, Phys. Rev. A **71**, 061402 (2005).

[171] C. V. Ciobanu, S. K. Yip, and Tin-Lun Ho, Phys. Rev. A **61**, 033607 (2000).

[172] Guang-Ming Zhang and Xiaoguang Wang, J. Phys. A: Math. Gen. **39**, 8515 (2006).

VITA

Bo Sun was born in Lianyungang, Jiangsu Province, P. R. China on December 12, 1975. He entered Nanjing University after high school in 1994 and received his B. S. degree in Physics in 1998 and M. S. degree in condensed matter physics in 2001 from Nanjing University. He came to the U. S. A. for more development in August 2001, studying at the Georgia Institute of Technology. Since Fall 2001, he has been a Teaching Assistant and later a Research Assistant in the School of Physics. His work at the Georgia Institute of Technology has concentrated on the theoretical studies of atom-atom, atom-photon, and photon-photon entanglement. His immediate postgraduate plan involves post-doctoral work. His scientific publications during this Ph. D. study include:

(1) Bo Sun, M. S. Chapman, and Li You, "Atom-photon entanglement generation and distribution", Phys. Rev. A **69**, 042316 (2004).

(2) Duan-Lu Zhou, Bo Sun, Chang-Pu Sun, and Li You, "Generating entangled photon pairs from a cavity-QED system", Phys. Rev. A **72**, 040302 (2005).

(3) Bo Sun, Duan-Lu Zhou, and Li You, "Entanglement between two interacting atoms in a one-dimensional harmonic trap", Phys. Rev. A **73**, 012336 (2006).

(4) Bo Sun, Wen-Xian Zhang, Su Yi, M. S. Chapman, and Li You, "Dipolar effect in coherent spin mixing of two atoms in a single optical lattice", Phys. Rev. Lett. **97**, 123201 (2006).

(5) Bo Sun and Li You, "Entanglement between two fermionic atoms inside a cylindrical harmonic trap", (submitted to Phys. Rev. A).